Article

SOURCE DATA | TRANSPARENT PROCESS

THE EMBO JOURNAL

Binary organization of epidermal basal domains highlights robustness to environmental exposure

Sangeeta Ghuwalewala[1,†], Seon A Lee[1,†], Kevin Jiang[1], Joydeep Baidya[1], Gopal Chovatiya[1], Pritinder Kaur[2], David Shalloway[1] & Tudorita Tumbar[1,*]

Abstract

Adulte interfollicular epidermis (IFE) renewal is likely orchestrated by physiological demands of its complex tissue architecture comprising spatial and cellular heterogeneity. Mouse tail and back skin display two kinds of basal IFE spatial domains that regenerate at different rates. Here, we elucidate the molecular and cellular states of basal IFE domains by marker expression and single-cell transcriptomics in mouse and human skin. We uncover two paths of basal cell differentiation that in part reflect the IFE spatial domain organization. We unravel previously unrecognized similarities between mouse tail IFE basal domains defined as scales and interscales versus human rete ridges and inter-ridges, respectively. Furthermore, our basal IFE transcriptomics and gene targeting in mice provide evidence supporting a physiological role of IFE domains in adaptation to differential UV exposure. We identify Sox6 as a novel UV-induced and interscale/inter-ridge preferred basal IFE-domain transcription factor, important for IFE proliferation and survival. The spatial, cellular, and molecular organization of IFE basal domains underscores skin adaptation to environmental exposure and its unusual robustness in adult homeostasis.

Keywords epidermal domains; human skin; scRNA-seq; Sox6; UV
Subject Categories Development; Skin; Stem Cells & Regenerative Medicine
DOI 10.15252/embj.2021110488 | Received 19 December 2021 | Revised 7 July 2022 | Accepted 8 July 2022 | Published online 10 August 2022
The EMBO Journal (2022) 41: e110488

Introduction

Adult skin interfollicular epidermis (IFE) makes the essential body barrier to the outside world and must respond to a variety of environmental insults and physiological demands (Blanpain & Fuchs, 2009; Gola & Fuchs, 2021). Homeostatic IFE renewal is likely resulting from local microenvironmental challenges, locally imposed on an intricate tissue architecture that comprises multiple levels of heterogeneity. The vicinity of the hair follicle, body region variations, skin maturation and aging, and stress conditions such as mechanical stretching or wounding pose additional challenges to IFE renewal (Roy *et al*, 2016, 2020; Aragona *et al*, 2017, 2020; Park *et al*, 2017; Ichijo *et al*, 2021). Development of skin cancers, such as melanoma, is also associated with IFE regional heterogeneity and UV-exposure (Kohler *et al*, 2017; Moon *et al*, 2017). We and others have previously documented that adult mouse IFE presents two spatially distinct domains that renew at different rates during homeostasis. These two domains are found in both mouse tail skin, known as scales and interscales, and in back skin; they can be identified as H2B-GFP or BrdU non-label retaining cells (non-LRCs) domains and LRCs domains (Riquelme *et al*, 2008; Gomez *et al*, 2013; Roy *et al*, 2016; Sada *et al*, 2016; Sanchez-Danes *et al*, 2016; Aragona *et al*, 2017). Human skin also presents two kinds of spatial domains, known as rete ridges and inter-ridge (Lawlor & Kaur, 2015), which based on their location in the epidermis have differential exposure to the outside environment. The functional significance of the two spatial IFE domains and their correspondence from mouse to human skin are currently unknown. Recent single-cell transcriptomics of mouse skin revealed basal layer (BL) cell heterogeneity with multiple cell states (Joost *et al*, 2018; Aragona *et al*, 2020; Dekoninck *et al*, 2020; Haensel *et al*, 2020; Lin *et al*, 2020), but how these states are spatially and functionally organized in the IFE is unclear. Recent data from human newborn foreskin suggest that different basal IFE cell states might be spatially organized (Wang *et al*, 2020). A persistent lack of markers to distinguish spatial and functional basal cellular subsets impedes our current understanding of IFE organization.

Here, we use markers of basal IFE cellular subsets in mouse and human skin to examine the molecular, cellular, and functional organization of two IFE spatial basal domains. We show that the two IFE domains have different gene expression patterns and predominantly different paths of basal layer (BL) cell differentiation (Synopsis). Despite these differences, they both contain comparable mixtures of cell states previously defined as stem, proliferating, and differentiating basal cell types. We find that mouse back skin IFE domain organization stands out as somewhat unique, but we unearth previously unrecognized similarities of basal IFE organization between mouse tail scales and interscales with human rete ridges and inter-ridges, respectively (Synopsis). Different molecular

1 Department of Molecular Biology and Genetics, Cornell University, Ithaca, NY, USA
2 Curtin Medical School/Curtin Health Innovation Research Institute, Curtin University, Perth, WA, Australia
*Corresponding author. Tel: +16073191597 E-mail: tt252@cornell.edu
†These authors contributed equally to this work

pathways—notably UV-response genes—are differentially upregulated in the two IFE domains, corresponding to their differential exposure to the outside environment. Our gene targeting functional studies in mice support the hypothesis that this heterogeneity is physiologically important, enabling the skin's adaptive response to UV exposure (Synopsis). This spatial and molecular organization of the IFE may help explain the remarkable robustness of long-term skin homeostasis in the face of environmental challenges.

Results

Mouse tail scale/non-LRC vs. interscale/LRC basal IFE domains express preferred genes at different levels

We previously labeled skin cells based on proliferation history and isolated IFE label retaining cells (LRCs) and non-LRCs from mouse back skin using our tet-repressible K5tTA x pTRE-H2BGFP transgenic mice (Tumbar *et al*, 2004; Sada *et al*, 2016). The classical stem cell (SC)-transit amplifying (TA) cell model (Kaur & Potten, 2011) predicted that LRCs would be exclusively SCs. However, we found that both LRCs and non-LRCs contained long-lived regenerative (stem) cells, which could be marked with distinct genetic drivers (Dlx1-CreER and Slc1a3-CreER, respectively). Moreover, LRCs and non-LRCs and their corresponding marked lineages segregated preferentially in two spatial domains in mouse back and tail skin (Fig 1A; Sada *et al*, 2016). In tail skin, LRC domains correspond to interscales, whereas non-LRC domains correspond to scales (Figs 1A and EV1A and B; Sada *et al*, 2016) (also see a top view example in Fig EV1A and B). These findings were also reported by two other groups (Gomez *et al*, 2013; Sada *et al*, 2016; Sanchez-Danes *et al*, 2016; Dekoninck *et al*, 2020). The interscale includes a subregion that unites all the hair follicles, which we called the "line" (Fig 1A; Sada *et al*, 2016). Using two inducible systems (K14-rTA and K5-tTA), we confirm here that 2-week chase via K5-tTA renders easily detectable LRCs in tail skin, as expected (Sada *et al*, 2016), and they were preferentially in $K10^{+}$ regions or interscales (Fig EV1C and D). Lack of IFE LRCs after 1-week chase (Rompolas *et al*, 2016; Piedrafita *et al*, 2020) suggests short chase periods may not be sufficient to render differences in proliferation rates in the different domains. In our chases, LRCs were also present in other body regions, such as back, ear, and paw (Fig EV2). We also used tamoxifen (TM) induction experiments and confirmed preferential Slc1a3-CreER or Dlx1-CreER marking of non-LRCs or LRCs spatial clusters in tail (Fig 1B and C). The drivers are also active in back, ear, and paw skin (Fig EV2A–D), except Dlx1-CreER is highly inefficient in back skin, where we use K14-CreER as a surrogate LRC control. Next, we tested marking via Aspm-CreER, another basal non-LRC gene from the back skin microarray (Sada *et al*, 2016; Kang *et al*, 2020), but this was not enriched in scale (non-LRC) domain (Figs 1B and C, and EV1A). Interestingly, the Dlx1-CreER marking was enriched along the interscale/scale boundary, and all three drivers marked the interscale "line" substructure (Fig 1A–C; Sada *et al*, 2016). This data suggest that although the H2B-GFP non-LRCs cluster preferentially in scales while the LRCs cluster preferentially in interscales, the LRC/non-LRC gene expression spatial patterns are more complex.

To examine spatial patterns of protein expression in the IFE basal domains, we used immunofluorescence (IF) staining and microscopy on different body regions of mice at different ages. We tested commercial antibodies to > 10 gene candidates we previously identified by microarrays of back skin IFE LRCs/non-LRCs (Sada *et al*, 2016), and obtained working conditions for Sox6 and Vamp1 (enriched in LRCs) and Slc1a3, Cxcl12, and Aspm (enriched in non-LRCs). We also used antibodies to some previously known SC-enriched genes—K15 (Webb *et al*, 2004; Cotsarelis, 2006), Col17a1 (Watanabe *et al*, 2017; Li *et al*, 2019), and K14 (Mascre *et al*, 2012). Most LRC/non-LRC-enriched factors, but especially, the Slc1a3 protein, were expressed in distinct basal cell clusters in adult tail (Figs 1D and EV1D). Back, ear, and paw BL also showed heterogeneous expression for some of these genes (Fig EV2D–F). However, overall correlation to LRC/non-LRCs was generally weaker in non-tail tissues (Fig EV2E–G). This might reflect more fluidity of the LRCs/non-LRC cell states and gene expressions in non-tail tissues. Newborn skin was relatively homogeneous to these expressions when compared with adult skin (Fig EV3A–C). Tail image quantification measured the differential expression of our LRC/non-LRC-enriched genes in the scale, interscale, and line basal IFE regions (Fig 1E). Except for Aspm and Cxcl12, the non-LRC-enriched genes (e.g., Slc1a3) were preferentially expressed in scale, whereas the LRC-enriched genes (Sox6 and Vamp1) were preferentially expressed in interscale (Fig 1F). Unexpectedly, previously known SC-expressed genes also showed preferred expression: K15 was enriched in scale, and K14 and Col17a1 were enriched in interscale (Fig 1E and F).

In summary, we identified preferred basal layer (BL) factors that distinguish the scale (*K15/Slc1a3*), a non-LRC-enriched tail domain, from interscale (*Vamp1/Sox6/Col17a1/K14*), a LRC-enriched tail domain (Fig 1G). Several of these genes also show heterogeneous expression in BL of other mouse body regions, but the correlation with LRC/non-LRCs is reduced in non-tail skin regions.

Human inter-ridges vs. rete ridges resemble the mouse interscale vs. scale domains

Human IFE is characterized by an undulating pattern of rete ridges (RR), which are spatial domains embedded deep into the dermis, and inter-ridges (IR), which are more raised and exposed IFE spatial domains (Lawlor & Kaur, 2015). Here, we used human skin samples to probe for expression of our newly identified preferred-genes from mouse IFE LRC domain (interscale in tail) and non-LRC domain (scale in tail). Interestingly, we found preferential expression of Slc1a3/K15 in the rete ridges and of Vamp1, Sox6, and Col17a1 in the inter-ridges (Figs 2A–H and EV4A–D). This correlation is maintained to some extent in human breast, forehead, abdomen, scalp, arm, cheek, ear, and newborn foreskin (ages 21, 30, 45, 52, 76-year-old; Fig EV4B and Appendix Table S1). These data reveal previously unrecognized similarities between mouse tail and human IFE organization in basal layer. Specifically, mouse tail interscales/LRC domains correspond to inter-ridges in human skin, and scales/non-LRC domains correspond to rete ridges (compare Figs 1G and 2M). Other basal markers such as Cxcl12 and Aspm were found in small basal cell clusters in both IR and RR (Fig 2D and E), reminiscent of their presence in both scales and interscales in mouse tail (Fig 1D–G). We briefly inquired into the

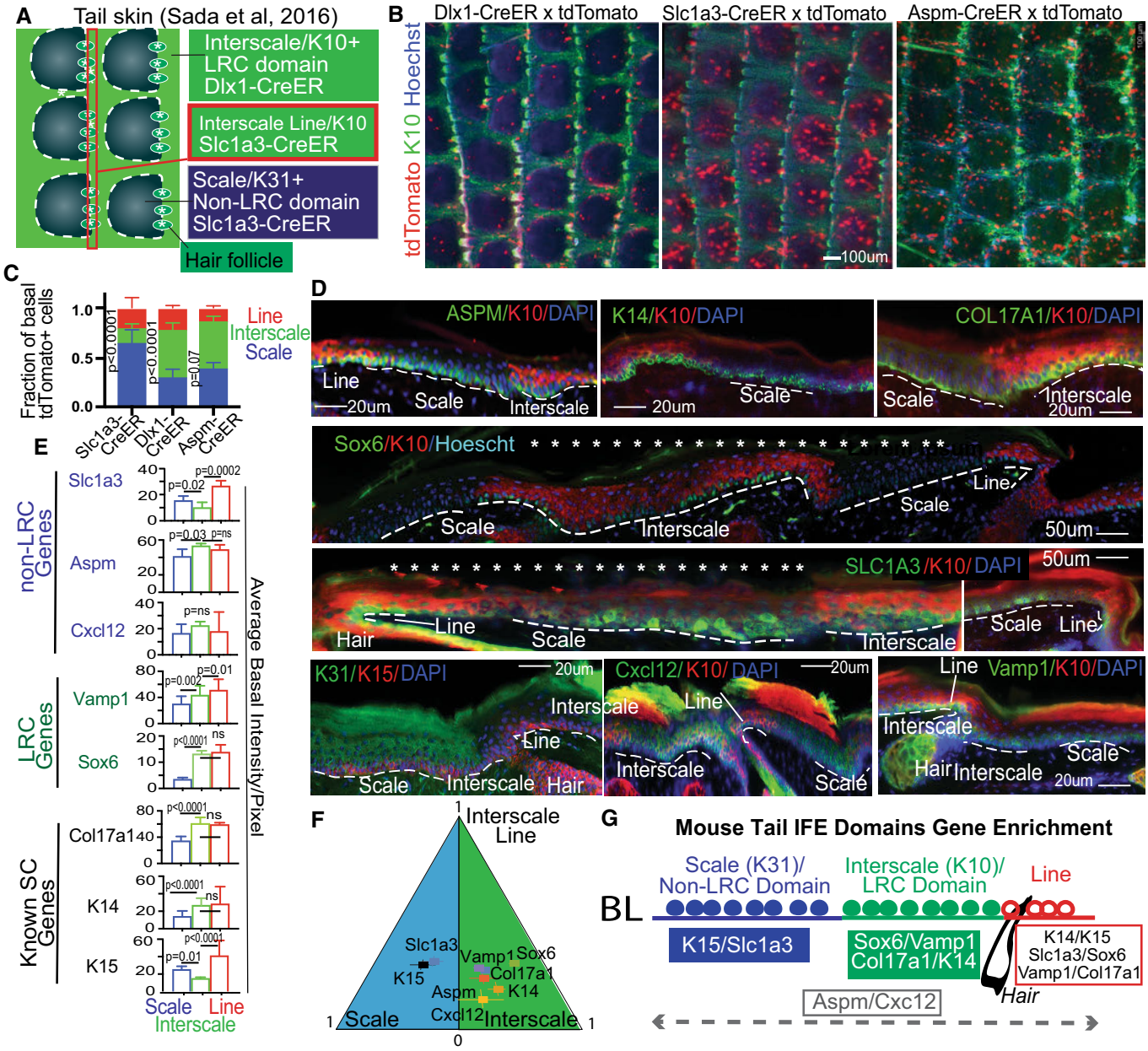

Figure 1. Basal layer cells express different LRC/non-LRC preferred-genes in scales vs. interscales of mouse tail skin.

A Model of tail skin organization in IFE domains.

B, C (B) Whole mount low magnification images show marking in interscale ($K10^+$) vs. scale regions, quantified in (C). Error bars are SDs. The data shown are average of four different time points (2 week, 3 month, 6 month and 1 year) each consisting of two mice and five images per mice. P-value is calculated for difference between scale vs. interscale using Student's *t*-test (mixed Anova).

D Tail skin sections immunofluorescence stained for interscale (K10) or scale (K31) supra-basal markers, and basal markers. Scale bar = 20 μm or 50 μm as indicated on the panels. Asterisks indicate that photoshop was used to erase the autoflourescent cornified layer. Dashed lines indicate ROI in basement membrane.

E Quantification of images like those in (D) with n = 3–4 mice and 6–7 images per mouse showing preferred-gene enrichment. Error bars are SDs. *P*-values calculated by Student's *t*-test (mixed effect model).

F Relative gene expression/area levels from (D) and (E), normalized to sum to one, and displayed in a barycentric plot obtained from a total of 3–4 biological replicates and 6–7 images per replicate. Error bars are SEMs. The proportions in Fig 1F were computed using log ratios (Aitchison, 1982).

G Cartoon summarizing spatial distribution of markers in the tail IFE domains.

proliferative status of RR and IR, but $Ki67^+$ proliferative cells showed no obvious difference (Fig EV4A), as reported (Ruetze *et al*, 2010). Notably, marker expression heterogeneity in the newborn human foreskin was less pronounced than in aged skin (Fig EV4C and D), reminiscent of the mouse age-dependent differences in heterogeneity (Fig EV3).

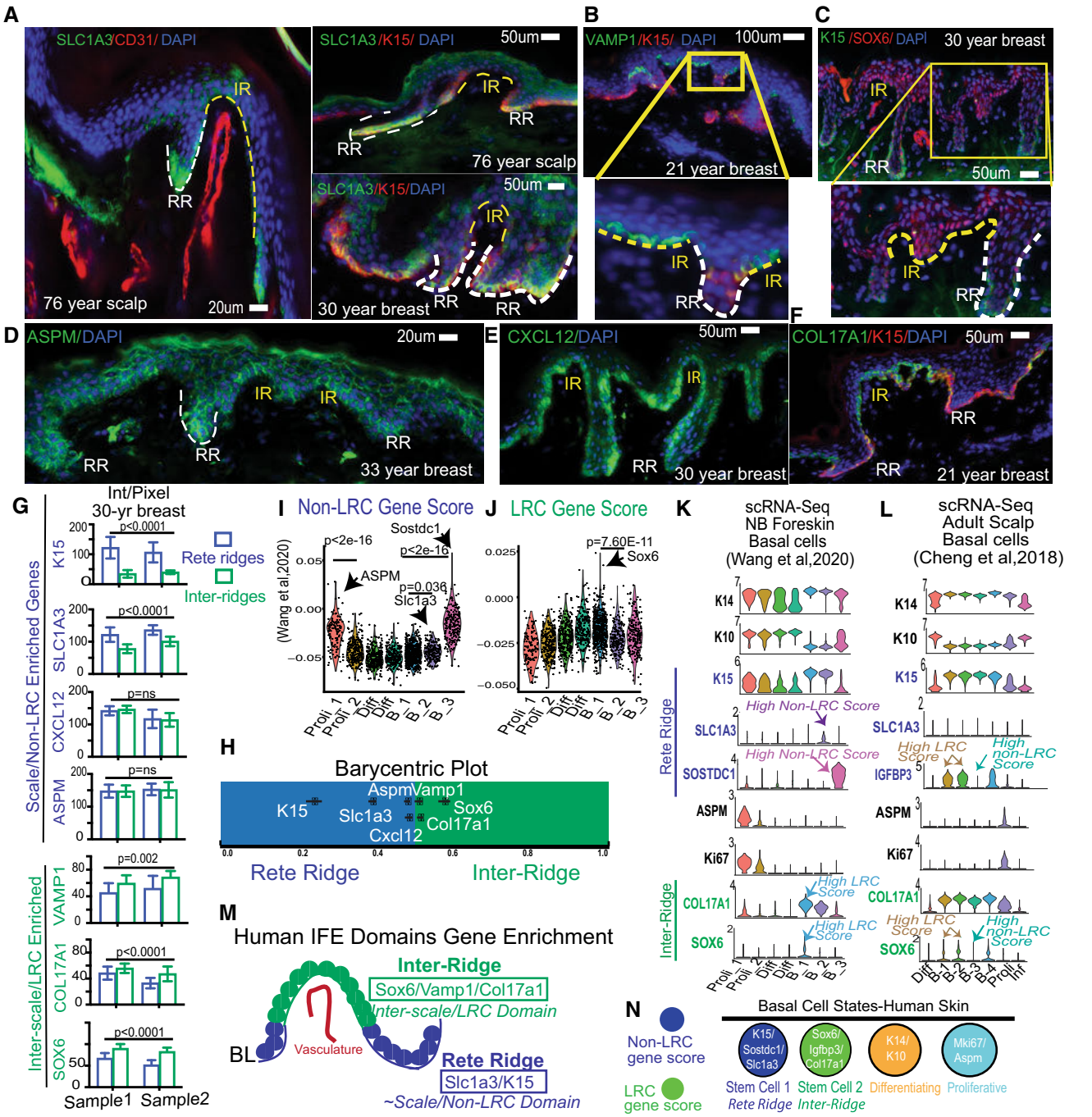

Figure 2. Human IFE shows basal domains and cell clusters enriched in mouse LRC/non-LRC preferred-genes.

A–F Human skin immunofluorescence images of mouse basal non-LRC/LRC preferred-factor staining in rete ridges (RR) versus inter-ridges (IR). Representative images from 30 samples of different body regions and ages (see Appendix Table S1). Scale bars are indicated on the panels.

G LRC/non-LRC preferred gene expression in RR and IR samples from two 30-year-old breast samples, quantified using background subtraction (Materials and Methods). *P*-values from paired Student's *t*-test. Error bars are SDs. 8–10 images were quantified each from two females.

H Relative RR vs. IR gene expression/area normalized to sum to one, shown as barycentric plot. A gene expressed only in inter-ridges would be plotted at 1. Error bars are SEMs.

I, J Gene score analysis in cell clusters from (Wang *et al*, 2020). *P*-values from pairwise Wilcoxon rank-sum tests with Benjamini-Hochberg correction.

K, L scRNA-seq identified clusters show specific gene expression of relevant markers.

M Cartoon summarizing differential RR vs. IR marker distribution.

N Model of human IFE basal cell states with LRC/ non-LRC gene expression distributions.

To further investigate our mouse IFE LRC/non-LRC preferred-genes in human skin, we used Seurat analysis (Satija *et al*, 2015; Butler *et al*, 2018) with Uniform Manifold Approximation and Projection (UMAP) (preprint: McInnes *et al*, 2018; Korsunsky *et al*, 2019) to probe two human single-cell (sc)RNA-seq databases recently generated from newborn foreskin (Wang *et al*, 2020) and adult scalp (Cheng *et al*, 2018). We identified seven clusters in human basal layer IFE (Fig EV4E and G), and examined marker expression of known SC, proliferation, differentiation, and our mouse LRC/non-LRC genes (Figs 2I–L and EV4E–J). All clusters expressed K14, indicative of their basal layer identity, but some had low levels of K10, suggesting they are initiating differentiation, as was also reported for mouse basal IFE (Rompolas *et al*, 2016; Park *et al*, 2017; Lin *et al*, 2020; preprint: Cockburn *et al*, 2021; Fig EV4F and H). Several clusters expressed Ki67, indicative of actively proliferating cells, and interestingly, those clusters also expressed our non-LRC marker Aspm. The remaining basal clusters that qualify as undifferentiated and non-proliferative (e.g., putative G0 SC states) expressed preferentially either non-LRC/scale makers (Slc1a3, Sostdc1, and K15) or LRC/interscale markers (Sox6, Igfbp3, and Col17a1) (Fig 2K and L). Furthermore, these clusters were enriched in either LRC or non-LRC computed gene scores (see Materials and Methods and Dataset EV1) (Figs 2I and J, and EV4I and J). We conclude that human IFE contains multiple basal cell states: differentiating, proliferative, and several putative SC states (Fig 2N). The SC states are enriched in either non-LRC or LRC gene, and the expression of preferred-genes place them in either rete ridges or inter-ridges (Fig 2N). This analysis adds to work and interpretation from (Wang *et al*, 2020). Importantly, the non-LRC vs. LRC gene enrichment in human rete ridges vs. inter-ridges resembles mouse tail scales vs. interscales, respectively (compare Figs 2M and 1G and see Synopsis). This suggests an unexpected and novel link between the organization of the IFE basal layer in tail skin and human skin.

LRCs/non-LRCs sorted from mouse back and tail skin harbor a mixture of basic basal cell states

To characterize the cell states present in our IFE LRC/non-LRC domains, we next used mouse tail and back skin isolated cellular subsets and performed scRNA-seq analysis (Figs 3A–J and EV5A–N; Appendix Fig S1A–E). We FACS purified basal ($Sca1^+/\alpha6\text{-integrin}^+$) IFE cells as H2BGFP LRCs, mid-LRCs, and non-LRCs from K5-tTA × pTRE-H2BGFP mice (Tumbar *et al*, 2004; Fig 3A) and used 10X Genomics scRNA-seq technology (see Materials and Methods). After quality control and filtering, we obtained a total of 13,484 cells from back skin of two mice, or ~ 4,500 cells each for LRC, mid-LRC and non-LRC sorted population (Fig EV5A–E). LRC vs. non-LRC gene scores computed from previous microarrays (Materials and Methods; Sada *et al*, 2016) confirmed the expected marker gene enrichment in our LRC vs. non-LRC scRNA-seq databases (Fig 3B). Some LRC/non-LRC gene expression differences previously found by microarrays (Sada *et al*, 2016) were detectable by scRNA-seq (e.g., Igfbp3, Chit1, and Sostdc1), but many others were not (Fig EV5F and G). Quantitative reverse transcriptase (QRT)–PCR confirmed the microarray results for some of the individually tested genes (Fig EV5H), underscoring detection limitations of scRNA-seq data.

Despite these limitations, cluster analysis of scRNA-seq data helped define basic basal cell states present in all sorted LRC, mid-LRC, non-LRC IFE populations (Fig 3C). Seurat and *Harmony* integration (Korsunsky *et al*, 2019) with quality control parameters and UMAP (preprint: McInnes *et al*, 2018) reduction method showed the 10 back skin basal cell clusters were well-correlated in two mouse samples (Fig EV5C–E). The results were similar in cluster analysis of 14,884 (4,402 LRCs, 6,236 mid-LRCs and 4,245 Non-LRCs) basal IFE cell fractions sorted from two tail skin replicates (Fig 3D; Appendix Fig S1A and B). To assign cell-cluster identity, we used previously published cluster-markers (Figs 3E and EV5I for back and Appendix Fig S1C for tail and Dataset EV1), cell cycle analysis (Fig EV5M), and gene scores (Fig EV5L; Appendix Fig S1D) extracted from other previously defined IFE cellular subsets (Joost *et al*, 2016; Dekoninck *et al*, 2020; Haensel *et al*, 2020). This classified both the back and the tail skin IFE clusters as: Three putative G0 SC states well-correlated in tail and back skin (Appendix Fig S1E); actively proliferating (Proli) cells; and basal-differentiating cells (Diff) (Fig 3C–E). Based on these data, we can infer that the two spatial (LRC/non-LRC) IFE basal domains of mouse back and tail skin harbor mixtures of basic basal cell states that can be defined by scRNA-seq (Fig 3F).

Next, we examined how the LRC/non-LRC gene expression signatures defined as gene scores (Materials and Methods) from the back skin microarrays (Sada *et al*, 2016) may be represented in the scRNA-seq basal cell clusters. The back skin scRNA-seq clusters showed mild, if any, differential enrichment in LRC/non-LRC-specific marker expression and computed gene scores (Fig EV5J and K, and N). This was reminiscent of IF staining results from back skin that showed poor correlation of preferred-gene expression with LRCs/non-LRC (Fig EV2G). In contrast, the tail skin SC clusters showed strong differences in LRC/non-LRC gene scores

Figure 3. Single-cell RNA-seq of basal IFE LRCs/non-LRCs sorted from mouse back and tail skin.

A FACS sorting of basal LRCs, mid-LRCs and non-LRCs.

B scRNA-seq data of sorted cells from (A) analyzed for LRC/non-LRC gene scores computed from microarray data (Sada *et al*, 2016).

C, D UMAP cell clusters identified based on published markers and cell cycle regression analysis (see 3E). Marker definition analysis is described in Fig EV5I–M (back) and Appendix Fig S1C–E (tail).

E Basal cluster definition markers.

F Model of basal IFE domain cell states.

G LRCs and non-LRCs computed gene scores are differentially enriched in tail SC clusters. *P*-values from pairwise Wilcoxon rank-sum tests with Benjamini-Hochberg correction.

H, I Violin and feature plots of markers in tail skin without proliferative (Proli) clusters. Note LRC/interscale markers Sox6&Igfbp3 enriched in SC-2&3 and non-LRC/scale markers K15/Sostdc1 enriched in SC-1. Slc1a3 is in SC-1 (scale); SC-2 expression is likely due to Slc1a3 expression in interscale line.

J Model of LRC/non-LRC gene scores and marker expression in scRNA-seq clusters found in tail vs. back skin.

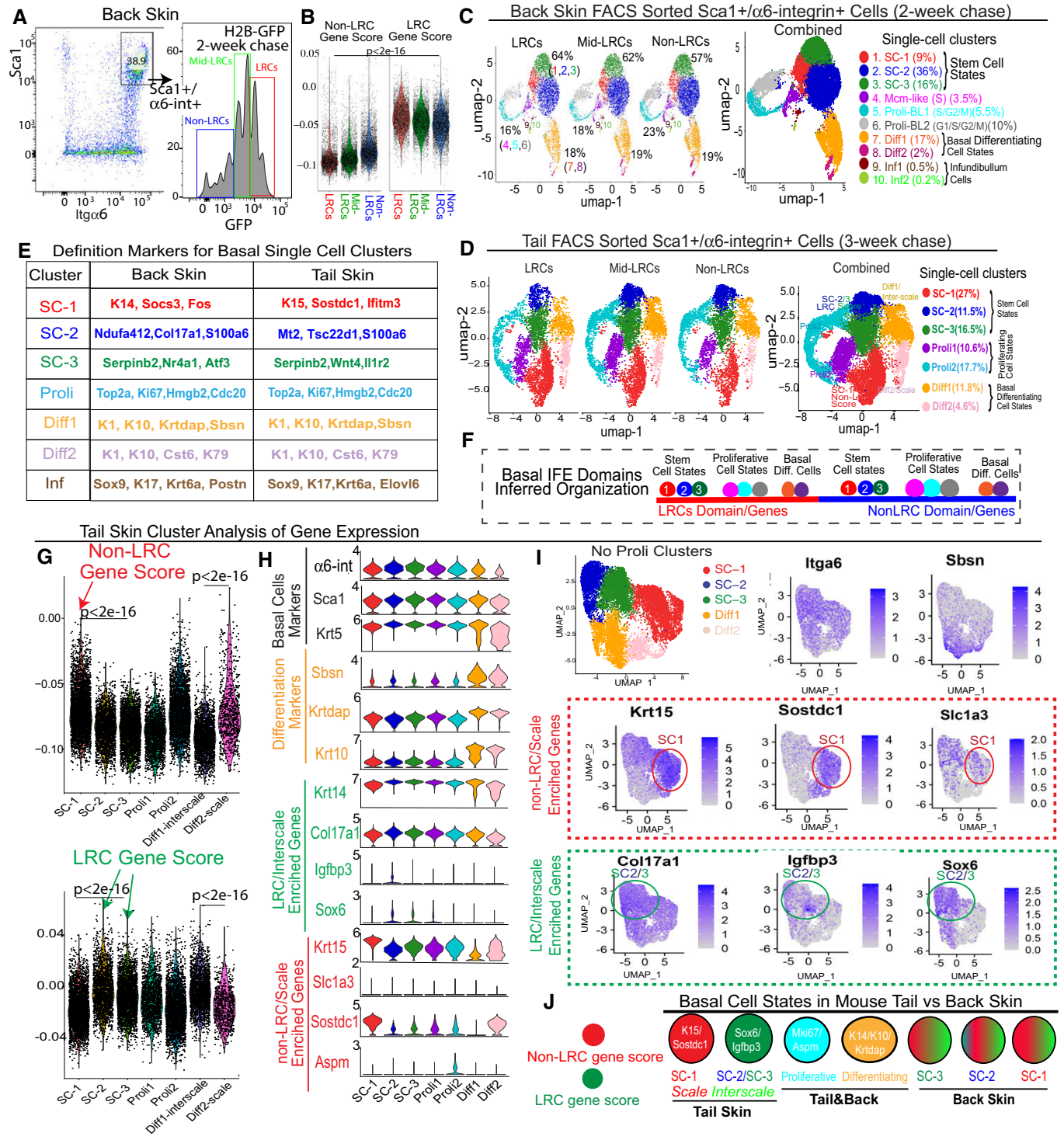

Cluster	Back Skin	Tail Skin
SC-1	K14, Socs3, Fos	K15, Sostdc1, Ifitm3
SC-2	Ndufa412,Col17a1,S100a6	Mt2, Tsc22d1,S100a6
SC-3	Serpinb2,Nr4a1, Atf3	Serpinb2,Wnt4,Il1r2
Proli	Top2a, Ki67,Hmgb2,Cdc20	Top2a, Ki67,Hmgb2,Cdc20
Diff1	K1, K10, Krtdap,Sbsn	K1, K10, Krtdap,Sbsn
Diff2	K1, K10, Cst6, K79	K1, K10, Cst6, K79
Inf	Sox9, K17, Krt6a, Postn	Sox9, K17,Krt6a, Elovl6

Figure 3.

(Fig 3G and H). Specifically, the SC-1 tail cluster was enriched in non-LRC gene scores and K15&Sostdc1 expressions (Fig 3G and H), which makes it a scale-preferred cluster. Conversely, SC-2 and SC-3 tail clusters were enriched in LRC gene scores and Igfbp3&Sox6 (Fig 3G and H), making them interscale-preferred. This was also apparent to some extent in feature plots of specific LRC/non-LRC preferred-genes (Fig 3I). Aspm marked proliferative clusters of both tail and back skin (Figs 3H and EV5J), as previously seen in human skin (Fig 2K and L). In summary, we propose that several basic basal cell states that include stem, proliferative, and differentiating cells exist in both LRC and non-LRC spatial domains of mouse back and tail skin. In the mouse

back skin, the LRC/non-LRC gene signatures do not differentiate well the three predicted stem cell states (Fig 3F). However, in tail skin, distinct scRNA-seq defined stem cell states express preferentially either the LRC or the non-LRC gene expression signatures (Fig 3J), a situation also seen in human undifferentiated basal cell clusters (Fig 2N). This further underscores the previously unrecognized similarities between mouse tail and human skin.

Two basal cell differentiation paths reflect the IFE spatial domain organization

To understand how the IFE basal cell states might relate to each other in transcriptomic lineage trajectory maps, we used Monocle 2 and Pseudotime analysis (Trapnell *et al*, 2014) from which the proliferative cell clusters were removed to eliminate bias due to cell cycle status. We analyzed all our mouse back and tail databases (Fig 4), along with two databases previously published from human (Cheng *et al*, 2018; Wang *et al*, 2020) (Appendix Fig S1F–H) and three from mouse skin (Joost *et al*, 2016; Dekoninck *et al*, 2020; Haensel *et al*, 2020) (Appendix Fig S1I–K). Our mouse sorted basal cells rendered a uniquely rich mouse dataset combining both high sequencing depth and large numbers of basal sorted cells. These combined qualities of our dataset uncovered a previously unidentified bifurcated lineage tree for the basal IFE, with three differentiation branches (Fig 4A and D), not as apparent in other smaller databases from mouse skin (Appendix Fig S1I–K). This 3-branched lineage tree was also present in a human skin dataset from the adult scalp (Fig 4G). The basal differentiating ($K14^+/K10^+$) cells were found on one branch, and the three predicted SC clusters were split on the other two branches (Fig 4A and D, and G).

Pseudotime analysis assigned the two SC branches as ground states, and they both converged onto the more committed, basal differentiating cells (Diff) (Fig 4B and E, and H). This suggests the existence of two distinct paths of IFE basal cell differentiation in mouse back and tail skin and in human scalp in the samples analyzed. In mouse back skin where LRC/non-LRC gene scores and expressions were not strongly differentiated in the three SC states (Figs 3J and EV2G), all three SC states intermingled together along each of the two differentiation paths (Fig 4A). In contrast, in mouse tail and human scalp skin where LRC/non-LRC gene scores and markers were strongly differentiated among the SC clusters (Figs 2N and 3J), the SC states were strongly segregated along the two basal differentiation paths (Fig 4D and G). Specifically, in tail, SC-1 (K15/Sostdc1-enriched; non-LRC score/e.g., of the scale) was on one path, while SC-2 and SC-3 (Igfbp3/Sox6-enriched; LRC score/ e.g., of the interscale) were on the other path (Fig 4D). This distribution was similar in human skin, where a basal cluster highly enriched in LRCs score/Sox6 expression (e.g., of the inter-ridge) was found on one path, while a different basal cluster enriched in non-LRC score (e.g., of the rete ridge) was found on the other (Fig 4G). The two differentiation paths seem to reflect at least in part the spatial organization of the IFE in mouse tail scales vs. interscales and in human rete ridges vs. inter-ridges (Fig 4F and I). Two basal paths of differentiation were detectable in mouse back skin as well, but a possible fluidity of SC states might exist along the two paths in this distinct tissue type (Fig 4C; see also Discussion and Synopsis).

Molecular pathway differences suggest IFE basal domain-specific adaptation to UV exposure

To further examine the cellular and molecular make up of our IFE basal populations enriched in the two spatial domains, we stained the back and tail skin of Slc1a3-CreER x, Aspm-CreER x, Dlx1-CreER x tdTomato mice at 1-month post-TM with basal markers (Slc1a3, K15, Aspm, Vamp1, and Cxcl12; Fig 5A and B; Appendix Fig S2A–D). K14-CreER x tdTomato mice served as a control population previously defined as a broad epidermal stem cell (Mascre *et al*, 2012). This population shows even distribution of all our five tested basal markers (Fig 5B). The Dlx1-CreER, Slc1a3-CreER, and Aspm-CreER progenies were enriched in their respective "parent" lineage-marker, and each showed a unique pattern of different marker distributions (Fig 5B). Notably, by 1-month post-TM, only a fraction of progenies expressed the parent-marker, suggesting that some descending cells convert into other basal cell states. This was true in both scales and interscales (Appendix Fig S2B). Therefore, we conclude that progenies of our IFE populations evolve over time, but overall remain different from each other, attesting to their distinct and heterogeneous molecular nature in the two spatial domains.

To systematically characterize the molecular differences among these IFE populations and obtain clues on their potential physiological purpose, we used bulk RNA-seq analysis for each of the individually sorted IFE lineages. For this, we FACS purified > 10,000 $tdTomato^+/Sca1^+/\alpha6\text{-}int^+$ (basal) cells from both back and tail skin at 2-week post-TM induction from each of four CreER mouse lines and normalized them to $Sca1^+/\alpha6\text{-}int^+$ sorted from the same mouse. Because the Dlx1-CreER is extremely inefficient in mouse back skin, we relied on K14-CreER as a control population in this body region. Hierarchical clustering and principal component analysis revealed hundreds of genes with differential expression in our IFE populations in both back and tail skin (Fig 5C–F; Appendix Table S2). GSEA analysis of Hallmark Pathways (Subramanian *et al*, 2005) revealed differential upregulation of many pathways including metabolism, inflammation, and hypoxia (Appendix Table S3) in both back and tail (Fig 5E and F). Two pathways that differed among our sorted IFE cells especially caught our attention, as they were related to UV-response genes (Fig 5E and F). Similarly, in scRNA-seq analysis, SC2/3 clusters enriched in Sox6 (an interscale/inter-ridge marker) also showed upregulation of UV-response genes as defined by Hallmark Analysis in both mouse tail and human scalp (Appendix Fig S2E–G). A second UV-signature list extracted from previously published work (Dataset EV1; Li *et al*, 2021; Shen *et al*, 2019) was also found enriched in the Sox6 expressing scRNA-seq clusters (e.g., SC3 in tail and B-1/2/4 in human scalp) (Appendix Fig S2H and I).

That UV-pathways might be differentially regulated in the distinct IFE population and domains was especially intriguing, given that in human skin, the basal layer in the domains (rete ridges and inter-ridges) clearly faces unequal UV exposure. Specifically, rete ridges, enriched in Slc1a3 and other non-LRC genes (Fig 2), are deeply embedded in the human skin and hence more UV-protected. Conversely, inter-ridges, enriched in LRC markers Sox6 and Vamp1 (Fig 2), are highly exposed to UV. In mouse tail, scales may be less UV-exposed than interscales, as they are more than double in thickness due to IFE undulations and very thick cornified envelope that retains nuclei in scales (Appendix Fig S3A–C). The degree of UV

COLOR

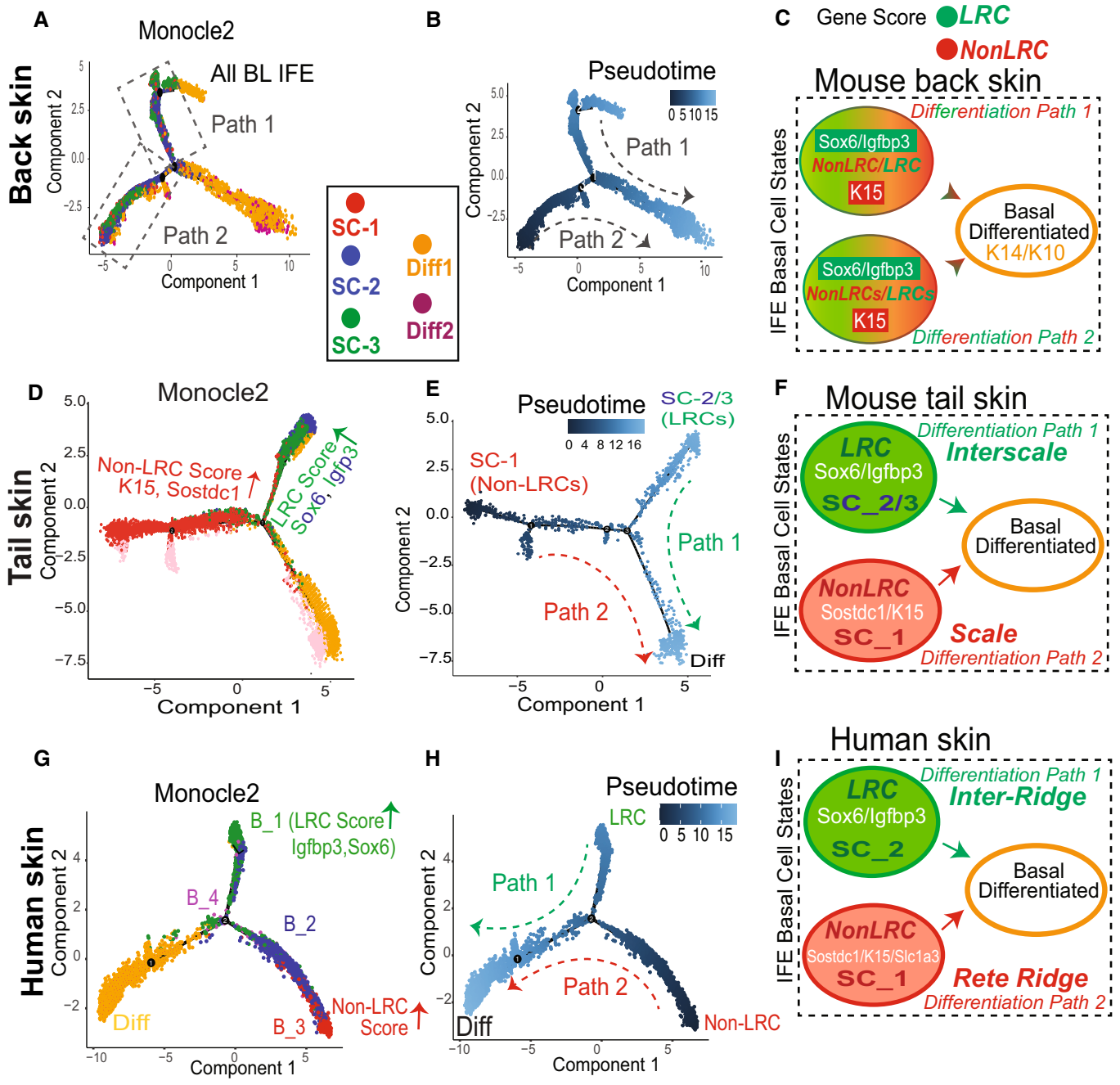

Figure 4. Transcriptomic lineage trajectory models reveal two basal IFE differentiation paths.

A–I (A, D, and G) *Monocle 2* lineage trajectory model and associated Pseudotime predictions (B, E, and H) for skin samples indicated with proliferative and infundibulum clusters excluded. (G) is human scalp from (Cheng *et al*, 2018). Pseudotime places the "Diff" basal cluster branch as most differentiated, as expected based on marker expression. (C, F, and I) Cartoons depicting two differentiation paths that based on LRC/non-LRC marker expression can be defined as tail scale vs. interscales (F) and human rete ridges inter-ridges (I); note mixed expressions along the two paths for back skin (C).

exposure of an IFE basal domain might explain the differential regulation of UV-response pathways detected in these domains.

To directly test whether UV exposure might affect the expression of some of our IFE domain preferred-genes, we irradiated the mouse back skin with UVB (Moon *et al*, 2017; Roy *et al*, 2020), which superficially affects the epidermis without penetrating to the dermal cells. We then performed IF staining for Aspm, Slc1a3, and Sox6 at several time points (Fig 5G; Appendix Fig S3D). Sox6 IF signal was clearly increased in basal cells by 6-h post-UVB exposure, and no signal was detected in Sox6 KO epidermis, confirming Sox6 antibody specificity (Fig 5G–H). Moreover, our quantification demonstrates that there is an increase in % $Sox6^{high}$ cells in response to

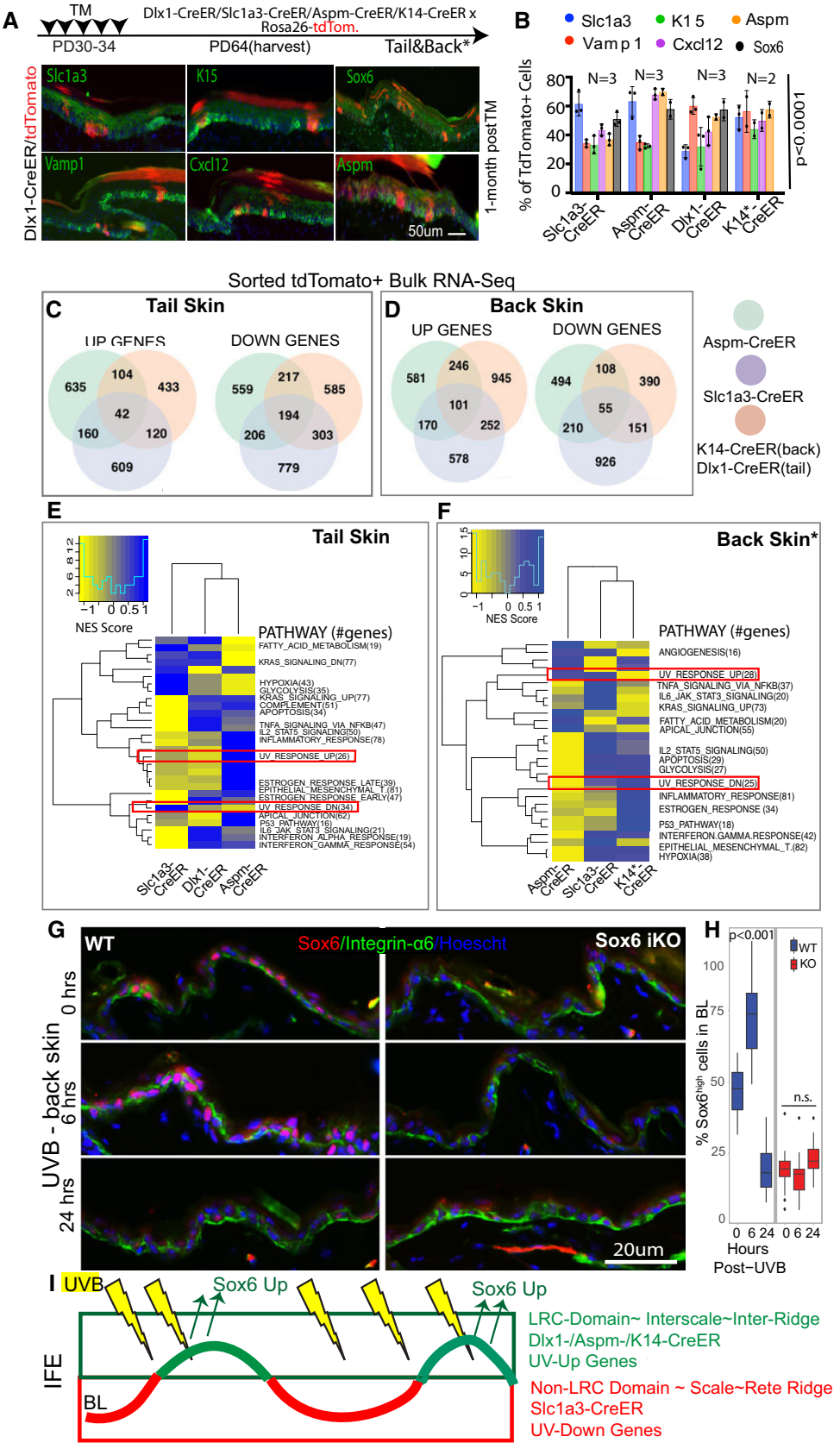

Figure 5.

Figure 5. Molecular differences in IFE populations suggest domain-specific adaptation to environmental UV exposure.

A Schematic showing the tamoxifen injection paradigm for tdTomato-labeling of all IFE lineages in tail and back. Co-expression of markers with the lineage-traced cells at 1-month post-tamoxifen. Dlx1-CrER is shown as example in tail; see also Appendix Fig S2A and C (*Back skin). Scale bar = 50 μm.

B Quantification of images like those in (A) and Appendix Fig S2A, showing % tdTomato$^+$ cells expressing indicated markers. Sox6 (black bar) was not analyzed in K14-Cre/EYFP lineage. See also Appendix Fig S2B for scale vs. interscale split. Error bars are SDs. *P*-values calculated by Student's *t*-test (mixed effects model) from $n = 2$–3 mice and 5–6 images per replicate.

C–F (C, D) Venn diagram showing bulk RNA-seq data in the three sorted IFE basal lineages and (E, F) heatmap for their differentially regulated Hallmark_Pathways.

G Immunofluorescence images of Sox6 staining in noUVB (0 h) or UVB-exposed (6 h- or 24-h post) mouse back skin.

H Boxplot shows % Sox6 expressing basal cells quantified from images like those in (G). Central band is the mean value, the top of box indicates 25th percentile while the bottom indicates 75th percentile. Whiskers indicate minimum and maximum values in the data, with dots indicating potential outliers. Linear mixed model statistical test was used with data from 18 images from 3 biological replicates.

I Model of IFE LRC/non-LRC domains and marked lineages with distinct degree of UV exposure in normal conditions.

UVB irradiation of the mouse back skin, resulting from Sox6^{low} cells acquiring more Sox6 expression (Fig 5G and H; Appendix Fig S3E and F). Further mining of the databases revealed several other UV-regulated gene candidates expressed at higher levels in the LRC-enriched SC clusters located in the more exposed IFE domains (Appendix Fig S4A–C). These results suggest that increased UV exposure of inter-ridges and interscales might contribute to Sox6 and possibly other LRC-domain genes upregulation in these regions (Fig 5I) and see Discussion. The upregulation of LRC-domain genes such as Sox6 in UV-exposed regions and in response to acute UV irradiation poses the question of what role might these genes play in skin homeostasis and in response to environmental challenges, such as UV exposure.

Sox6 promotes IFE proliferation and survival during homeostasis and in UV exposure

To first examine the role of Sox6 in the IFE during homeostasis, we deleted Sox6 from the skin epithelium and examined basal layer cell proliferation, differentiation, and survival in mouse tail. We used inducible Sox6 knockout (iKO) mice obtained by crossing the K14-CreER^{T2} (Indra, 1999) and Sox6$^{fl/fl}$ mice (Dumitriu *et al*, 2006), and injected TM at PD32 followed by a short BrdU pulse-chase experiment (Fig 6A). We then sacrificed both wild-type (WT) and iKO littermates at 2-h, 12-h, and 7-day chase and quantified BrdU$^+$ cells. Initially, the number of BrdU-labeled basal cells was comparable in WT vs. Sox6 iKO, but by 7-day chase, they significantly decreased in the iKO (Fig 6B and C; Appendix Fig S5A). The DNA damage (Appendix Fig S5B and C) and the epidermis thickness marked by K10 (Appendix Fig S5D) were not significantly different between two groups. To check whether the BrdU$^+$ cell loss in the iKO IFE during chase is caused by changes in proliferation, cell death, or both, we performed Ki67 and Caspase3 staining and quantified the results. We observed decreased proliferation (Fig 6D and E) and a transient increase in cell death in the iKO IFE compared with CT skin (Fig 6F and G). Importantly, these data indicate that Sox6 promotes cell proliferation and survival in the IFE basal layer. To our surprise, despite Sox6 upregulation in interscale compared with scale, the gene loss affected basal cells in both scale and interscale (Appendix Fig S5E–M). Apparently, even at lower expression levels as those found in the scales, Sox6 actively promotes normal IFE proliferation and survival during skin homeostasis. Differences in proliferation as indicated by Ki67 staining, survival, and DNA damage were subtle, if any, and not detectable in these assays between scale and interscale by IF staining (Appendix Fig S5N–Q). Interestingly, whereas initially Sox6 loss results in increased cell death and decreased proliferation, by 30-day post-TM injection, cell death resolves and proliferation appear upregulated in the epidermis (Appendix Fig S5R–U). This is likely due to robust skin compensatory mechanisms to overcome tissue abnormalities in long-term.

Since Sox6 was upregulated in the IFE upon acute UVB irradiation (Fig 5G and H), we then asked whether Sox6 plays an additional or additive role in UV response. Thus, we UVB irradiated back skin of WT and Sox6 iKO mice and analyzed them at different time points post-exposure (Fig 6H). Staining with Ki67$^+$ demonstrated that proliferative cells were fewer in the IFE of iKO mice at 0 and 6-h post-UVB, although interestingly and unlike in homeostasis, they recovered by 24 h (Fig 6I and J). In contrast, cell apoptosis was consistently increased in the Sox6 iKO IFE upon UVB treatment (Fig 6K and L). Furthermore, the frequency of DNA-damaged cells was decreased in the iKO IFE by 6-h post-UV (Fig 6M and N). These results together suggest that in acute UVB stress upon Sox6 loss, IFE basal cells may resort more to apoptosis rather than DNA damage repair, compounding the effect this gene loss has on cell survival during homeostasis. Overall, our data demonstrate that the LRC-factor Sox6, enriched in more UV-exposed IFE regions (e.g., inter-ridges in human and interscales in mouse tail), plays a vital role in basal cell proliferation and survival during homeostasis and in acute UV exposure (Fig 6O).

Discussion

Here, we characterize the molecular, cellular, and functional organization of two types of IFE basal spatial domains in both mouse and human skin. The two spatial IFE domains were previously shown in mouse tissue kinetics studies to renew at (~ 2x) different rates in mouse back and tail skin (Mascre *et al*, 2012; Gomez *et al*, 2013; Roy *et al*, 2016; Sada *et al*, 2016; Sanchez-Danes *et al*, 2016), hence harboring preferentially either LRCs or non-LRCs in pulse-chase experiments. This relatively small proliferation differences cannot be detected by short chases (Rompolas *et al*, 2016; Piedrafita *et al*, 2020) or by less quantitative tissue kinetics studies, such as Ki67 staining. Based on lineage tracing data with different CreER drivers, we previously proposed that the two spatial domains each contain a spatially distinct stem cell population (Sada *et al*, 2016). Here, we demonstrate by *in situ* analysis that the two basal IFE domains express LRC/non-LRC preferred genes and some other known SC markers at different protein levels. The two domains

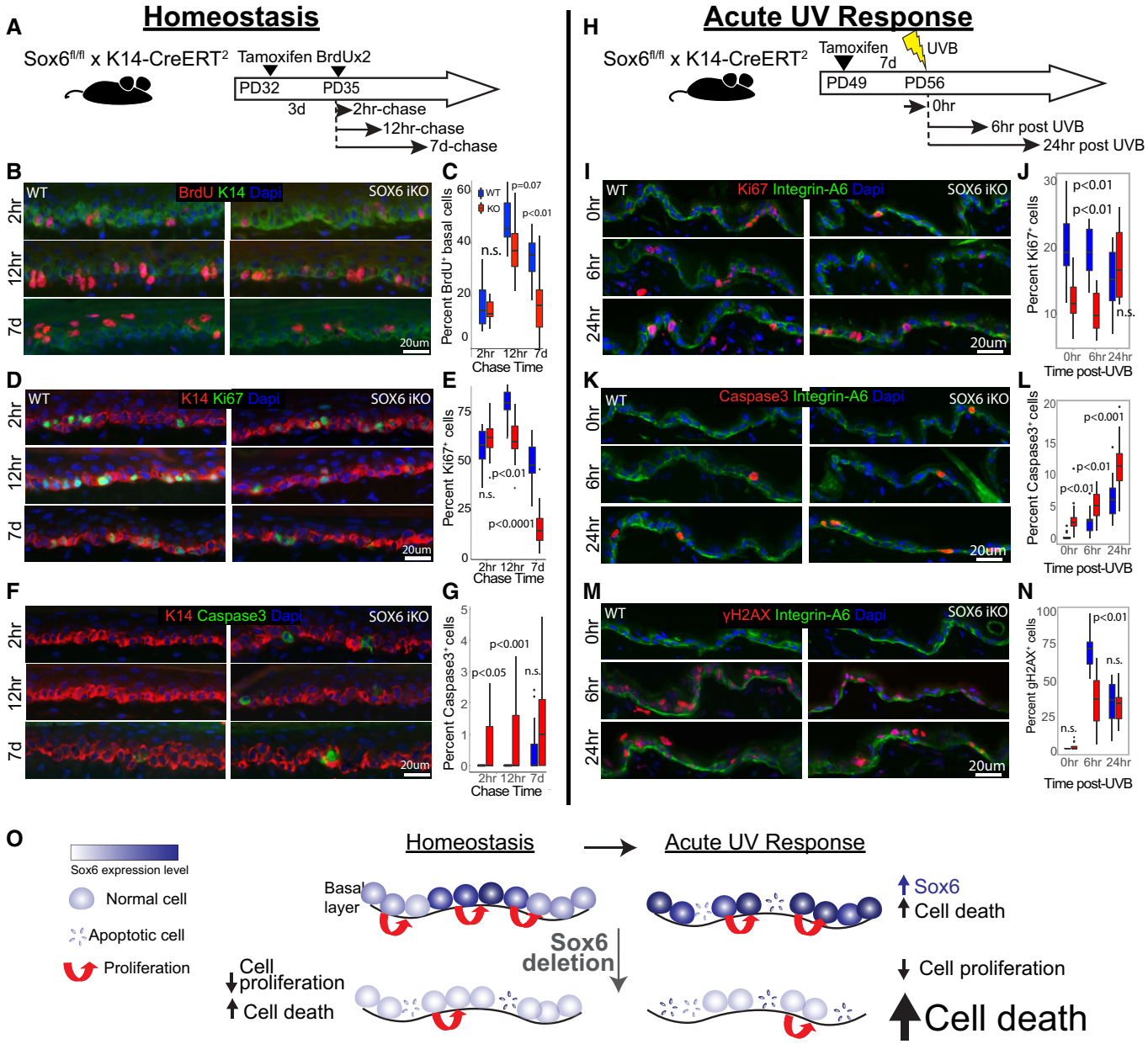

Figure 6. Sox6 role in basal cell proliferation and survival during homeostasis and acute UV response.

A Schematic of Sox6 epithelial knockout (iKO) and BrdU pulse-chase experiment.

B–G (B, D, and F) Images of tail skin immune-stained for markers indicated and (C, E, and G) corresponding box plots.

H Sox6 role in acute UV-response was assessed in back skin to avoid compounding effects from the nucleus-retaining cornified envelope in tail scales.

I–N (I, K, and M) Images of skin immune-stained for markers indicated and (J, L, and N) corresponding box plots.

O Model depicting the role of Sox6 in IFE homeostasis and acute UV response.

Data information: In box plots, central band is the mean value, and the top indicates 25th percentile while the bottom indicates 75th percentile. Whiskers indicate minimum and maximum values in the data, with dots indicating potential outliers. Linear mixed model statistical test was used with data from 18 images from three biological replicates.

contain mixtures of molecularly discrete basal cell states on their path to differentiation, as defined by single-cell transcriptomics. Importantly, we propose that the spatial and molecular organization of these two domains reflects in part the IFE adaptation to environmental exposure.

The spatial organization of IFE in domains is reflected in two basal cell differentiating paths, as described by our single-cell transcriptomic analysis of mouse and human skin. The two differentiation paths harbor distinct stem cell states and, unexpectedly, show strong similarities in human skin and mouse tail but not mouse back skin.

Specifically, the tail IFE domains, defined as scales and interscales, show similarities of preferred-gene expression and lineage differentiation trajectories with the human rete ridges and inter-ridges, respectively (Synopsis). Furthermore, our IF and single-cell transcriptomic data suggest that mouse scales and their newly found human counterpart—rete ridges—harbor stem cell states enriched in our non-LRC gene signatures. Conversely, the mouse interscales and their new human counterpart—the inter-ridges—harbor SCs enriched in our LRC gene signatures (Synopsis). The mouse back skin, which has so far been considered a prototype of human skin, shows the most distinct behavior among all these skin types. Although the mouse back skin presents two distinct differentiation paths, the SC states are intermingled along the paths and present a mixed identity based on LRC/non-LRC gene signatures (Synopsis). An important difference between tail and back is that in tail, the LRC/non-LRC domains remain as permanent fixed structures (e.g., interscale/scales) throughout the animals' life. In contrast, in back skin, an LRC domain may be a temporary structure with a fluid identity. This identity may be influenced by local and changing micro-environmental conditions, or by the waves of synchronized hair cycle progression specific to mouse back skin (Plikus *et al*, 2011; Roy *et al*, 2016), which influence the overall rates of epidermal proliferation. In contrast to back skin, and similar with tail scales/interscales, human skin rete ridges/inter-ridges also may remain as fixed spatial structures throughout animal's life and thus display strong segregation of stem cell identities along the two basal layer differentiation paths.

An important finding of our study is that cells from the two IFE domains express a set of genes and molecular pathways that distinguish them at the functional level. Many pathways are differentially regulated, and future studies will be needed to decipher the full spectrum of these differences. However, given the spatial organization of IFE domains, one clear functional link that emerges from our study is with UV-response. This may be explained at least in part by the differential exposure of the two IFE domains to the outside world (e.g., rete ridges and scales are less exposed than inter-ridges and interscales). A link of UV response with spatial organization was also proposed for smaller epidermal domains, which are strictly linked to the vicinity of the hair follicle (Roy *et al*, 2020). We propose that the differential pattern of basal gene expressions in the more environment-exposed regions (e.g., the LRC gene signature) may be in part (although not in total, see below paragraph), a consequence of skin's increased UV stress in these IFE regions (Synopsis). These genes likely underline the adaptation that provides each epidermal domain with equal chances of survival despite differential exposure. This model is supported by our data on the LRC-factor Sox6, a novel interscale/inter-ridge enriched gene. Interestingly, Sox6 is also upregulated in skin with atopic dermatitis, a disease in which epidermal barrier defects cause excessive environmental susceptibility (Liew *et al*, 2020). Our gene targeting data in mice demonstrate that Sox6 promotes basal cell proliferation and survival during homeostasis. In long-term, the epidermis compensates for its loss by upregulating proliferation. We also find that Sox6 is readily upregulated by basal cells upon UV exposure to combat cellular stress and prevent excessive apoptosis (Synopsis). Although future work is required to substantiate downstream mechanisms, Sox6 emerges here as a novel LRC-domain gene prototype, which helped us decipher at least one potential physiological meaning of epidermal spatial organization. In future, it will be interesting to examine how exactly is Sox6 performing its role in epidermis survival and proliferation in homeostasis and UV response.

One exciting possibility is that UV-protection may be a broader characteristic of LRC-related genes, as several UV-induced master regulators (Shen *et al*, 2019; Li *et al*, 2021) appeared in our analysis preferentially upregulated in the LRC/interscale/inter-ridge-enriched population. These observations warrant a more systematic future testing of LRC signature genes implication in UV and other environmental-stress responses. While exposure to UV and other environmental challenges may contribute to spatial and molecular IFE domain organization, this is likely not the absolute origin of it. The laboratory mouse is not naturally exposed much to UV, and the scale/interscale regions form early on after birth, by ~ PD9 (Gomez *et al*, 2013; Sada *et al*, 2016), before extensive exposure were possible. Furthermore, the distinct spatial IFE domains already exist to some extent in newborn human foreskin ([Wang *et al*, 2020] and this work, suggesting the domains may be established during skin development. We plan to investigate the question of epidermal spatial patterning in the future.

In closing, we propose that the spatial organization of the IFE basal layer in distinct regenerative domains encompasses complex cellular and molecular organization. This organization may reflect the skin adaptation to local environmental challenges, imposed on a non-uniform 3D tissue structure. The spatial, cellular, and molecular complexity of the basal layer may contribute to the remarkable robustness of epidermis, this extraordinarily resilient and essential tissue that faces constant challenges during adult homeostasis.

Materials and Methods

Mice

All mouse work was carried out according to Cornell University Institutional Animal Care and Use Committee guidelines (protocol number no. 2007–0125). To employ the H2B–GFP tet-off system, double-transgenic K5–tTA (FVB) (Diamond *et al*, 2000)/pTRE–H2B–GFP (CD1) (Tumbar *et al*, 2004) mice were used. Mice were fed with doxy chow (1 g doxy/1 kg, Bio-serv) for the indicated chase periods, starting at 1–3 months of age. Chase times are indicated for all the different experiments.

For lineage tracing, K14-CreER (CD1) (Vasioukhin *et al*, 1999), Dlx1-CreER (C57BL6) (Taniguchi *et al*, 2011) (The Jackson Laboratory, no. 014551) Slc1a3-CreER (C57BL6) (Nathans, 2010) (The Jackson Laboratory, no. 012586) mice or Aspm-CreER (Madisen *et al*, 2010; Marinaro *et al*, 2011), were crossed with Rosa–tdTomato reporter mice (Madisen *et al*, 2010; The Jackson Laboratory). CreER/Rosa–tdTomato mice without TM injections were used to examine the leakiness of Cre. Dlx1-CreER, Slc1a3-CreER or Aspm-CreER quadruple-transgenic mice (CreER/Rosa–tdTomato/K5–tTA/pTRE–H2B–GFP) were obtained after several steps of intercrossing the above lines. Cre-ER/K5tTa (using Tet860-1060 primers), Rosa-EYFP (used for K14-CreER) and tdTomato mice were genotyped as recommended by the Jackson manufactures primer and protocol.

For short-term BrdU pulse-chase and UVB-irradiation experiment, K14-CreER^{T2} mice (Indra, 1999) were crossed with Sox6$^{fl/fl}$ mice (Dumitriu *et al*, 2006) to generate inducible epithelial-specific Sox6 knockout (iKO) mice.

Tamoxifen injection

K14-CreER-H2BGFP quadruple-transgenic mice were injected intraperitoneally with a single dose of TM (Sigma) (75 μg g^{-1} body weight for FACS, 200 μg g^{-1} in K14-CreER-EYFP). For lineage tracing and FACS experiments (using Dlx1-CreER and Slc1a3-CreER lines), mice were injected with TM (100 μg g^{-1} body weight) for five consecutive days at 4–7 weeks of age. Intermediate dose (100 μg g^{-1} body weight for two consecutive days) was used for Aspm CreER and Slc1a3-CreER lines in the lineage staining experiments. Mice were euthanized at the indicated times after the last injection.

To induce epithelial-specific Sox6 deletion for short-term BrdU pulse-chase and UVB experiments, K14-$CreER^{T2}$ × $Sox6^{fl/fl}$ mice were injected with a single dose of 100 μg g^{-1} body weight tamoxifen at PD32 or PD49, respectively.

Human samples

Human skin samples were de-identified except age and sex was recorded. They were obtained as frozen OCT tissue samples, under Cornell Office of Research Integrity and Assurance IRB for Human Participants, Protocol# 0908000777.

Whole-mount immunostaining in the tail epidermis

Tail skin pieces (5 mm × 5 mm) were incubated in EDTA (20 mM)/PBS on a shaker at 37°C for 2 h to separate the epidermis from the dermis as an intact sheet. Epidermal sheets were fixed in 4% paraformaldehyde (PFA) overnight at 4°C. The skin pieces were washed, incubated in blocking buffer (1% BSA, 2.5% donkey serum, 2.5% goat serum, 0.8% Triton in PBS) for 3 h at room temperature, and incubated with primary antibodies/blocking buffer overnight at room temperature. Samples were washed 4× in PBS with 0.2% Tween for 1 h at room temperature, and were incubated overnight with secondary antibodies at 4°C. After washing, samples were counterstained with Hoechst for 1 h and mounted. For the H2B-GFP samples, back and tail skin were chased for 2, 3 or 6-week, respectively. No-GFP staining was done to enhance the signal.

Primary antibody dilutions: mouse anti-K10 (1:100, BioLegend 904301), rat anti-β4-integrin (1:200, BD bioscience 553745), guinea pig anti-K31 (1:100, PROGEN Biotechnik GP-hHa1), rabbit anti-K14 (1:100, BioLegend 905301). All secondary antibodies (TxR, FITC, Cy5 or Alexa-594, Jackson ImmunoResearch) were used at a 1:500 dilution. The MOM kit (Vector Laboratories) was used for blocking when staining with mouse primary antibodies.

Preparations were analyzed by confocal microscopy (Zeiss LSM710 or Zeiss LSM880) with Zen 2012 software. All confocal data are shown as projected *Z*-stack images viewed from the basal surface.

Prefixation of tdTomato expressing tissues before embedding and immunostaining of mouse and human skin sections

For lineage-traced mice (both tdTomato or EYFP), back and tail skin (with intact dermis) were prefixed in 4% PFA overnight and passed through sucrose gradient (15 and 30%) before embedding. Non-CreER or only H2BGFP chased mice back and tail skin was directly embedded in optimal cutting temperature (OCT) compound (Tissue Tek, Sakura). The frozen sections (10 μm) were fixed with 4% PFA for 10 min at room temperature. After blocking in normal serum, sections were incubated with primary antibodies overnight at 4°C. The following day, the sections were washed and incubated for 1 h with secondary antibodies at room temperature. After washing, the sections were counterstained with Hoechst and mounted. For staining with anti-BrdU antibody, the sections were treated with 2 M HCl for 55 min at 37°C after blocking and stained as described above.

Primary antibody dilutions were as follows: rabbit anti-K14 (1:1,000, BioLegend 905301), mouse anti-K10 (1:100, BioLegend 904301), guinea pig anti-K31 (1:100, PROGEN Biotechnik GP-hHa1), chicken anti-K15 (1:150, BD Biosciences 833904), rabbit anti-Ki67 (1:100, Abcam ab15580), rabbit anti-Slc1a3 (1:300, abcam 416), Aspm (1:1,000, Proteintech 26223-1-AP), Vamp1 (1:500, Proteintech 13115-1-AP), Col17a1 (1:20,000, Invitrogen MA5-31984) and Cxcl12 (1:500, Cell Signaling Technology 97958S). Rabbit anti-Sox6 (1:4,000, Abcam ab30455), anti-Caspase3 (1:4,000, R&D Systems AF835), anti-gamma H2AX (1:4,000, Abcam ab2893), rat anti-α6 integrin (1:4,000, BD Biosciences 555734), anti-BrdU (1:400, Abcam ab6326), chicken anti-K14 (1:40,000, BioLegend 906004), mouse anti-K10 (1:4,000, Abcam ab9026). All secondary antibodies (TxR, FITC, Cy5 or Alexa-594, Jackson ImmunoResearch) were used at 1:500 dilution. For mouse primary antibodies, the MOM kit (Vector Laboratories) was used for blocking.

Preparations were examined using a fluorescent microscope (Nikon) and digitally imaged using a CCD (charge-coupled device) 12-bit digital camera (Retiga EXi; QImaging) and IP-Lab software (MVI).

Short-term BrdU pulse-chase

For short-term bromodeoxyuridine (BrdU) pulse-chase labeling, 35 days old K14-Cre^{ERT2}/ $Sox6^{fl/fl}$ mice and their control litter mates (n = 3 per group) were injected with 50 μg/g body weight BrdU intraperitoneally twice at 12-h intervals. 2 h-chased mice were harvested 2 h after the first BrdU injection, while 12 h- and 7 days-chased mice were harvested at the indicated times after the last injection.

UVB-irradiation

UVB irradiation was performed on 56-day-old K14-$CreER^{T2}$/$Sox6^{fl/fl}$ mice and their control litter mates (n = 3 per group) following the procedure described in a previously published protocol (Moon *et al*, 2017). Isoflurane was used to anesthetize mice during dorsal skin shaving at PD55 and UVB-irradiation procedure at PD56, and 180 mJ/cm^2 UVB was irradiated on dorsal skin during the irradiation. No UVB (0 h UVB) and UVB-exposed skin samples (6 h or 24 h post-UVB) were collected at indicated times after the procedure.

Quantification of microscope images

Relative fluorescence intensity per unit area/pixel or fraction of tdtomato$^+$ cells of the basal layer were quantified by using ImageJ software. The scale/interscale regions are defined based on the retention of nuclei in the cornified layer in the scale region and/or K10 (interscale) or K31(scale) expression. The data were normalized

by subtracting background intensity (the region of lowest intensity in the basal layer) per image. For H2B-GFP overlap analyses, we first examined basal cells that were marker positive vs. negative, qualitatively define cells with low GFP intensity, that was then quantified and set as threshold to further classify cells in GFP^{low} vs. GFP^{high}. Next, we counted both marker positive and negative cells per image and calculated % BL expressing marker irrespective of H2BGFP. For whole mount clonal data, the number of $tdTomato^{+}$ clones of the tail epidermis was counted on maximal projections *Z*-stack confocal images. Clones are defined as clusters of cells that contain at least one basal or suprabasal cell. Quantifications were independently performed on ≥ 2 mice/per time point/per genotype, and ≥ 50 clones/structure were counted per mouse.

FACS sorting

Mouse back/tail skin was incubated in 0.25% trypsin/versene overnight at 4°C and for 30 min at 37°C. Single-cell suspensions were prepared by scraping off the fat and subcutaneous tissue from the dermal side of the skin followed by enzymatic digestions and subsequent filtering with strainers (70 mm, followed by 40 mm). Cells were stained with the following antibodies for 30 min on ice: FITC rat anti-Sca1 (1:300, 557405) or PE-Cy7 rat anti-Sca1 (1:400, 558162) and Brilliant Violet 421 rat anti-α6-integrin (1:200, 313624) from BD Biosciences. Dead cells were excluded by AmCyan Live/Dead dye (1:500, Invitrogen L34966) staining. FACS (FACS Aria, BD Biosciences) analyses were performed in the Cornell Flow Cytometry facility. FACS data were analyzed with the FlowJo software.

RNA isolation and RT–PCR

Total RNAs were isolated from sorted skin cells prepared by TriZol method and used for reverse transcription by Super script III (Invitrogen). The primers used were as follows: Gapdh, 5′-ACTGCCACCCAGAAGACTGT-3′ and 5′-GATGCAGGGATGATGTTCT-3′; Dlx1, 5′-ATGCCAGAAAGTCTCAACAGC-3′ and 5′-AACAGTGCATGGAGTAGTGCC-3′; Igfbp3, 5′-TCTAAGCGGGAGACAGAATACG-3′ and 5′-CTCTGGGACTCAGCACATTGA-3′; Sox6, 5′-GGTCATGTTTCCCACCCACAA-3′ and 5′-TTCAGAGGGGTCCAAATTCCT-3′; Slc1a3,5′-ACCAAAAGCAACGGAGAAGAG-3′ and 5′-GGCATTCCGAAACAGGTAACTC-3′; Aspm, 5′-TGGCTATGAGTGAATGCTCTTCC-3′ and 5′-TCGCGTAAAAACAGTGGCAAG 3′; Vamp1,5′-CAGTGCTGCCAAGCTAAAAA-3’and 5′-CCAGTAGCCGTCTCCATACC-3′; Cxcl12, 5′-GCGCTCTGCATCAGTGAC-3’and 5′-TTTCAGATGCTTGACGTTGG-3′ K14, 5′-AAGGTCATGGATGTGCACGAT-3′ and 5′-CAGCATGTAGCAGCTTTAGTTCTTG-3′; K10, 5′-GGAGGGTAAAATCAAGGAGTGGTA-3′ and 5′-TCAATCTGCAGCAGCACGTT-3′; K15, 5′-GGAGGTGGAAGCCGAAGTAT-3′ and 5′-GAGAGGAGACCACCATCGCC-3′ qRT–PCR for each gene is normalized to GAPDH. The relative level for each gene is set to 1 in the control population.

Single-cell capturing, library generation and processing of scRNA-seq data

FACS collected $\alpha6\text{-integrin}^{+}/Sca1^{+}$ cells from back skin epidermis were further purified by GFP intensity into LRCs, Mid-LRCs and Non-LRCs from two male mice at PD47 (telogen). Single-cell suspension of each cell type (~ 4,000 live cells) were processed to generate single-cell 3′ cDNA libraries using individually barcoded 10X Chromium Single-Cell 3′ gel bead and library Kit v3, according to the manufacturer's recommendations (10x Genomics). RNA from the barcoded cells was reverse transcribed, followed by amplification, shearing 50 adaptor and sample index attachment. The final libraries were quantified using Agilent Bioanalyzer high-sensitivity DNA chip and sequenced using an Illumina NextSeq-500. The raw data files were demultiplexed to generate the sample-specific FASTQ files, which were aligned to the mouse reference genome (mm10-3.0.0) using the 10X Genomics Cellranger pipeline (v3.1.0) with default parameters. Approximately 270 M reads were generated for the LRCs, Mid-LRCs and Non-LRCs libraries from the back skin, with a mean number of 68,000, 56,000 and 42,000 reads per cell. After filtering, 3,674, 4,308 and 5,500 cells were analyzed for back skin, detecting a median of 3,000 genes per cell. For tail skin, we analyzed 4,402, 6,236 and 4,245 cells combined from two replicates for the LRCs, Mid-LRCs and Non-LRCs respectively. Total reads per cell and the number of genes detected were comparable to back skin.

Single-cell RNA-seq data analysis

The output from the Cellranger from the 10X platform consists of a matrix of raw read counts that was further analyzed in R using the Seurat package version 3.1 (Satija *et al*, 2015). High-quality cells that contain at least 200–5,000 genes with a mitochondrial gene percentage under 10% were filtered. Expression value scaling and normalization, PCA and UMAP dimensionality reductions and clustering were performed using the Seurat (Butler *et al*, 2018) R package (version 3.0.1). LRCs, Mid-LRCs and Non-LRCs were integrated using harmony (version 1.0) (Korsunsky *et al*, 2019) after scaling expression values for each sample independently using Seurat, resulting a total of 13,487 cells by combining two replicates for further analyses, which could be further splitted back into LRCs, Mid-LRCs and Non-LRCs for sample-specific information. To identify cell clusters, principle component analysis (PCA) was first performed and the top 10 PCs with a 0.55 resolution were used to obtain 10 clusters. Differentially expressed genes for all the clusters were acquired using FindAllMarkers function with log2 fold change > 0.25 using the Wilcoxon Ranked Sum test. Multiple resolutions (0.3, 0.5, 0.7, 0.9) were assessed to reveal clusters with biological significance and perform marker gene discovery. Markers were then selected by setting the threshold to all genes with an adjusted P-value lower than 0.05. After filtering, cells belonging to the infundibulum ($Sox9^{high}$, $Krt17^{high}$, and $Krt79^{high}$), differentiated cells ($Krt10^{high}$, $Krt1^{high}$, and $Sbsn^{high}$), putative SC cell types (SC1, SC2, and SC3; $Krt14^{high}$ $Krt15^{high}$, and $Col17a1^{high}$), proliferating cells (enriched in either S-phase MCMs and/or G2-M cell-cycle related genes were remarkably segregated; Mki67, Top2a, and Cdc20) were manually assigned based on their expression of various related genes (Dekoninck *et al*, 2020; Haensel *et al*, 2020).

Pseudotime lineage trajectory

Trajectory analysis was performed using Monocle (Trapnell *et al*, 2014). First, the Seurat object (v3) was converted to a monocle cds (cell data set) and then loaded into Monocle2. We used the top 2,000 differentially expressed genes that were calculated using

the standard Seurat workflow to assign pseudotime values to individual cells. The cells that contain lower than 200 transcripts were removed from further analyses. The trajectories were constructed with DDRTree.

LRC/non-LRC gene score computation and cell cycle analysis

Cell-cycle phases of different clusters were predicted using Seurat's Cell-Cycle scoring method Each cell was scored based on the expression of certain G2M and S phase markers. Any cell that did not express either G2M or S phase markers was predicted to be in G0/G1. The AddModuleScore function in the Seurat R package was used to calculate signature scores and determine whether there was any significant difference between the subpopulations. This function was widely used for scoring various gene sets from previous literature for both mice (Dekoninck *et al*, 2020; Haensel *et al*, 2020) and human (Wang *et al*, 2020). Specific genes in each gene set are listed in Dataset EV1. The two-sided Wilcoxon rank-sum test (Ji *et al*, 2020) was used to evaluate whether there are significant differences in the computed signature scores between two groups of cells.

Bulk RNA-sequencing

RNA-seq were performed in triplicates (BL Slc1a3/Dlx1/Aspm-tdTomato positive BL and total BL α6-integrin$^+$/Sca1$^+$ cells) isolated from three female mice at PD49 (telogen). Total RNA was isolated from sorted cell populations using Trizol (Thermo Fisher) according to the commercial protocol with the following additions: after the first phase separation, additional chloroform extraction step of the aqueous layer in Phase-lock Gel heavy tubes (Quanta Biosciences); addition of 1ul Glyco-blue (Thermo Fisher) immediately prior to isopropanol precipitation; two washes of the RNA pellet with 75% ethanol. The RNA sample quality was confirmed using a Qubit3 (RNA HS kit; Thermo Fisher) to determine concentration and with a Fragment Analyzer (Advanced Analytical) to determine RNA integrity. The PolyA$^+$ RNA was enriched with the NEBNext Poly(A) mRNA Magnetic Isolation Module (New England Biolabs).

Illumina library preparation and sequencing

Since our samples resulted in low-input RNA (< 20 nt total RNA), truSeq-barcoded RNA-seq libraries were generated with the Ultra II RNA Library Prep Kit (non-directional) (New England Biolabs). Each library was quantified with a Qubit 2.0 (dsDNA HS kit; Thermo Fisher), and the size distribution was determined with a Fragment Analyzer (Advanced Analytical) prior to pooling. Libraries were sequenced on an Illumina instrument (Hiseq4000). 2x150 bp HiSeq reads were generated with a depth of 20 M.

Mapping the reads

Preprocessing: reads were trimmed for low quality and adaptor sequences with TrimGalore v0.6.0 (ref 1), a wrapper for cutadapt (ref 2) and fastQC (ref 3). Parameters: -j 1 -e 0.1 --nextseq-trim = 20 -O 1 -a AGATCGGAAGAGC --length 50 --fastqc;unwanted reads were removed with STAR v 2.7.0e (ref 4). Parameters: --outReadsUnmapped Fastx *mapping*: reads were mapped to the reference genome/transcriptome (mouse/mm10) using STAR v2.7.0e (ref 4). GeneCounts *gene expression analysis*: SARTools and DESeq2 v1.26.0 were used to generate normalized counts and statistical analysis of differential gene expression (ref 5,6). Parameters: fitType parametric, cooks Cutoff TRUE, independent Filtering TRUE, alpha 0.05, pAdjustMethod BH, typeTrans VST, locfunc median.

Software references

1 TrimGalore: Felix Krueger.
http://www.bioinformatics.babraham.ac.uk/projects/trim_galore/
2 cutadapt: Marcel Martin.
https://cutadapt.readthedocs.io/en/stable/http://journal.embnet.org/index.php/embnetjournal/article/view/200
3 fastQC: Simon Andrews.
http://www.bioinformatics.babraham.ac.uk/projects/fastqc/
4 STAR: Alexander Dobin.
https://doi.org/10.1093/bioinformatics/bts635
5 SARTools: Hugo Varet.
https://doi.org/10.1371/journal.pone.0157022
6 DEseq2: Michael Love.
http://www.bioconductor.org/packages/release/bioc/html/DESeq2.htmlhttps://genomebiology.biomedcentral.com/articles/10.1186/s13059-014-0550-8

Quality control analysis

Principal component analysis was performed on the raw counts for the different tdTomato$^+$ sorted populations normalized in both back and tail skin with their respective BL (α6-integrin$^+$/Sca1$^+$) sorted control and the scores were represented in a three-dimensional scatter plot. Hierarchical clustering was performed on all the samples to reflect sample grouping between tail and back epidermal populations After normalization, the genes having counts with a signal value < 100 or reported "absent" were excluded. The remaining genes that are ≥ 2-fold up- or downregulated in BL relative to BL tdTomato$^+$ lineages were selected. Signature genes were defined as those that were ≥ 2-fold upregulated in one lineage over its own BL. To compare the populations gene-wise, lists of '≥ 2-fold change in Aspm/Slc1a3/Dlx1/K14-CreER; tdTomato normalized over total BL (~ 400 genes) were used. For pathway comparison, lists of 'log FC ≥ 1 or < 1 genes without any cut-off on raw count signal (~ 4,000 genes) was used (Appendix Table S2). The numbers of overlapping genes are shown in the Venn diagram (Fig 6C). Gene Set Enrichment analyses using Hallmark pathways ([using GSEA 4.0 with classic parameters]; Subramanian *et al*, 2005) were performed on differentially expressed genes (Appendix Table S3).

Statistics and reproducibility

All experiments with or without quantification were independently performed at least twice with different mice and the representative data are shown. All statistical analyses were performed either using the two-tailed Student's *t*-test (mixed Anova) or linear mixed model as indicated in each figure legend; statistical significance was defined as $P < 0.05$.

The sample size was dictated by experimental considerations and not by a statistical method. The experiments were not

randomized. The investigators were not blinded to allocation and outcome assessment during experiments.

Data availability

The scRNA-seq data for both the replicates reported in this paper have been deposited in the Gene Expression Omnibus (GEO) database under accession code GSE205746 (https://www.ncbi.nlm.nih.gov/geo/query/acc.cgi?acc=GSE205746), which is the super Series linked to GSE205745 (12 scRNA-seq samples; https://www.ncbi.nlm.nih.gov/geo/query/acc.cgi?acc=GSE205745). Bulk RNA sequencing data that support the findings of this study have been deposited in the GEO under accession code GSE205744 (28 bulk RNA-seq samples; https://www.ncbi.nlm.nih.gov/geo/query/acc.cgi?acc=GSE205744). All other data supporting the findings of this study are available from the corresponding author on request.

Expanded View for this article is available online.

Acknowledgments
We thank L. Tesfia and J.E. Mahoney for FACS; C. J. Bayles, R. M. Williams, and J. M. DelaCruz for confocal imaging (BRC Facility) and data processing; J. Grenier, A.E. Tate and F. Ahmed for RNA sequencing (TREX facility); P.A. Schweitzer for 10x genomics scRNA-seq run; B. Cosgrove for help with scRNA-seq analysis; T.E. Hall for Vamp1 antibody staining conditions. The Cornell CARE staff for mouse husbandry. The Cornell Biotechnology Research Center and Imaging Facility as supported by NIH Grant 1S10RR025502-01. The research was supported by grants from the National Institute of Arthritis and Musculoskeletal and Skin Diseases (R01AR070157 and R01AR073806) to TT.

Author contributions
Sangeeta Ghuwalewala: Conceptualization; data curation; software; formal analysis; validation; investigation; visualization; methodology; writing – original draft; project administration; writing – review and editing. **Seon A Lee:** Conceptualization; data curation; software; formal analysis; validation; investigation; visualization; methodology; writing – original draft; project administration; writing – review and editing. **Kevin Jiang:** Data curation; formal analysis; validation; investigation; visualization. **Joydeep Baidya:** Formal analysis; validation; visualization. **Gopal Chovatiya:** Software; methodology; writing – review and editing. **Pritinder Kaur:** Resources; data curation; formal analysis; writing – review and editing. **David Shalloway:** Data curation; software; formal analysis; validation; methodology; writing – review and editing. **Tudorita Tumbar:** Conceptualization; resources; formal analysis; supervision; funding acquisition; investigation; visualization; methodology; writing – original draft; project administration; writing – review and editing.

Disclosure and competing interests statement
The authors declare that they have no conflict of interests.

References

Aitchison J (1982) The statistical analysis of compositional data. *J R Stat Soc B Methodol* 44: 139 – 177

Aragona M, Dekoninck S, Rulands S, Lenglez S, Mascre G, Simons BD, Blanpain C (2017) Defining stem cell dynamics and migration during wound healing in mouse skin epidermis. *Nat Commun* 8: 14684

Aragona M, Sifrim A, Malfait M, Song Y, Van Herck J, Dekoninck S, Gargouri S, Lapouge G, Swedlund B, Dubois C *et al* (2020) Mechanisms of stretch-mediated skin expansion at single-cell resolution. *Nature* 584: 268 – 273

Blanpain C, Fuchs E (2009) Epidermal homeostasis: a balancing act of stem cells in the skin. *Nat Rev Mol Cell Biol* 10: 207 – 217

Butler A, Hoffman P, Smibert P, Papalexi E, Satija R (2018) Integrating single-cell transcriptomic data across different conditions, technologies, and species. *Nat Biotechnol* 36: 411 – 420

Cheng JB, Sedgewick AJ, Finnegan AI, Harirchian P, Lee J, Kwon S, Fassett MS, Golovato J, Gray M, Ghadially R *et al* (2018) Transcriptional programming of normal and inflamed human epidermis at single-cell resolution. *Cell Rep* 25: 871 – 883

Cockburn K, Annusver K, Ganesan S, Mesa KR, Kawaguchi K, Kasper M, Greco V (2021) Gradual differentiation uncoupled from cell cycle exit generates heterogeneity in the epidermal stem cell layer. *bioRxiv* https://doi.org/10.1101/2021.01.07.425777 [PREPRINT].

Cotsarelis G (2006) Epithelial stem cells: a folliculocentric view. *J Invest Dermatol* 126: 1459 – 1468

Dekoninck S, Hannezo E, Sifrim A, Miroshnikova YA, Aragona M, Malfait M, Gargouri S, de Neunheuser C, Dubois C, Voet T *et al* (2020) Defining the design principles of skin epidermis postnatal growth. *Cell* 181: 604 – 620.e22

Diamond I, Owolabi T, Marco M, Lam C, Glick A (2000) Conditional gene expression in the epidermis of transgenic mice using the tetracycline-regulated transactivators tTA and rTA linked to the keratin 5 promoter. *J Invest Dermatol* 115: 788 – 794

Dumitriu B, Dy P, Smits P, Lefebvre V (2006) Generation of mice harboring a Sox6 conditional null allele. *Genesis* 44: 219 – 224

Gola A, Fuchs E (2021) Environmental control of lineage plasticity and stem cell memory. *Curr Opin Cell Biol* 69: 88 – 95

Gomez C, Chua W, Miremadi A, Quist S, Headon DJ, Watt FM (2013) The interfollicular epidermis of adult mouse tail comprises two distinct cell lineages that are differentially regulated by Wnt, Edaradd, and Lrig1. *Stem Cell Reports* 1: 19 – 27

Haensel D, Jin S, Sun P, Cinco R, Dragan M, Nguyen Q, Cang Z, Gong Y, Vu R, MacLean AL *et al* (2020) Defining epidermal basal cell states during skin homeostasis and wound healing using single-cell transcriptomics. *Cell Rep* 30: 3932 – 3947.e6

Ichijo R, Kabata M, Kidoya H, Muramatsu F, Ishibashi R, Abe K, Tsutsui K, Kubo H, Iizuka Y, Kitano S *et al* (2021) Vasculature-driven stem cell population coordinates tissue scaling in dynamic organs. *Sci Adv* 7: eabd2575

Indra AK (1999) Temporally-controlled site-specific mutagenesis in the basal layer of the epidermis: comparison of the recombinase activity of the tamoxifen-inducible Cre-ERT and Cre-ERT2 recombinases. *Nucleic Acids Res* 27: 4327

Ji AL, Rubin AJ, Thrane K, Jiang S, Reynolds DL, Meyers RM, Guo MG, George BM, Mollbrink A, Bergenstrahle J *et al* (2020) Multimodal analysis of composition and spatial architecture in human squamous cell carcinoma. *Cell* 182: e422

Joost S, Zeisel A, Jacob T, Sun X, La Manno G, Lonnerberg P, Linnarsson S, Kasper M (2016) Single-cell transcriptomics reveals that differentiation and spatial signatures shape epidermal and hair follicle heterogeneity. *Cell Syst* 3: 221 – 237.e9

Joost S, Jacob T, Sun X, Annusver K, La Manno G, Sur I, Kasper M (2018) Single-cell transcriptomics of traced epidermal and hair follicle stem cells reveals rapid adaptations during wound healing. *Cell Rep* 25: 585 – 597.e7

Kang S, Long K, Wang S, Sada A, Tumbar T (2020) Histone H3 K4/9/27 trimethylation levels affect wound healing and stem cell dynamics in adult skin. *Stem Cell Reports* 14: 34 – 48

Kaur P, Potten CS (2011) The interfollicular epidermal stem cell saga: sensationalism versus reality check. *Exp Dermatol* 20: 697 – 702

Kohler C, Nittner D, Rambow F, Radaelli E, Stanchi F, Vandamme N, Baggiolini A, Sommer L, Berx G, van den Oord JJ *et al* (2017) Mouse cutaneous melanoma induced by mutant BRaf arises from expansion and dedifferentiation of mature pigmented melanocytes. *Cell Stem Cell* 21: 679 – 693.e6

Korsunsky I, Millard N, Fan J, Slowikowski K, Zhang F, Wei K, Baglaenko Y, Brenner M, Loh PR, Raychaudhuri S (2019) Fast, sensitive and accurate integration of single-cell data with harmony. *Nat Methods* 16: 1289 – 1296

Lawlor KT, Kaur P (2015) Dermal contributions to human interfollicular epidermal architecture and self-renewal. *Int J Mol Sci* 16: 28098 – 28107

Li KN, Jain P, He CH, Eun FC, Kang S, Tumbar T (2019) Skin vasculature and hair follicle cross-talking associated with stem cell activation and tissue homeostasis. *Elife* 8: e45977

Li MY, Flora P, Pu H, Bar C, Silva J, Cohen I, Galbo PM Jr, Liu H, Yu X, Jin J *et al* (2021) UV-induced reduction in Polycomb repression promotes epidermal pigmentation. *Dev Cell* 56: e2548

Liew WC, Sundaram GM, Quah S, Lum GG, Tan JSL, Ramalingam R, Common JEA, Tang MBY, Lane EB, Thng STG *et al* (2020) Belinostat resolves skin barrier defects in atopic dermatitis by targeting the dysregulated miR-335: SOX6 axis. *J Allergy Clin Immunol* 146: 606 – 620.e12

Lin Z, Jin S, Chen J, Li Z, Lin Z, Tang L, Nie Q, Andersen B (2020) Murine interfollicular epidermal differentiation is gradualistic with GRHL3 controlling progression from stem to transition cell states. *Nat Commun* 11: 5434

Madisen L, Zwingman TA, Sunkin SM, Oh SW, Zariwala HA, Gu H, Ng LL, Palmiter RD, Hawrylycz MJ, Jones AR *et al* (2010) A robust and high-throughput Cre reporting and characterization system for the whole mouse brain. *Nat Neurosci* 13: 133 – 140

Marinaro C, Butti E, Bergamaschi A, Papale A, Furlan R, Comi G, Martino G, Muzio L (2011) *In vivo* fate analysis reveals the multipotent and self-renewal features of embryonic AspM expressing cells. *PLoS One* 6: e19419

Mascre G, Dekoninck S, Drogat B, Youssef KK, Brohee S, Sotiropoulou PA, Simons BD, Blanpain C (2012) Distinct contribution of stem and progenitor cells to epidermal maintenance. *Nature* 489: 257 – 262

McInnes L, Healy J, Melville J (2018) UMAP: uniform manifold approximation and projection for dimension reduction (Version 3). *arXiv* https://doi.org/10.48550/ARXIV.1802.03426 [PREPRINT]

Moon H, Donahue LR, Choi E, Scumpia PO, Lowry WE, Grenier JK, Zhu J, White AC (2017) Melanocyte stem cell activation and translocation initiate cutaneous melanoma in response to UV exposure. *Cell Stem Cell* 21: 665 – 678.e6

Nathans J (2010) Generation of an inducible Slc1a3-cre/ERT transgenic allele. *MGI Direct Data Submission [MGI Ref ID J:157151]*

Park S, Gonzalez DG, Guirao B, Boucher JD, Cockburn K, Marsh ED, Mesa KR, Brown S, Rompolas P, Haberman AM *et al* (2017) Tissue-scale coordination of cellular behaviour promotes epidermal wound repair in live mice. *Nat Cell Biol* 19: 155 – 163

Piedrafita G, Kostiou V, Wabik A, Colom B, Fernandez-Antoran D, Herms A, Murai K, Hall BA, Jones PH (2020) A single-progenitor model as the unifying paradigm of epidermal and esophageal epithelial maintenance in mice. *Nat Commun* 11: 1429

Plikus MV, Baker RE, Chen CC, Fare C, de la Cruz D, Andl T, Maini PK, Millar SE, Widelitz R, Chuong CM (2011) Self-organizing and stochastic behaviors during the regeneration of hair stem cells. *Science* 332: 586 – 589

Riquelme PA, Drapeau E, Doetsch F (2008) Brain micro-ecologies: neural stem cell niches in the adult mammalian brain. *Philos Trans R Soc Lond B Biol Sci* 363: 123 – 137

Rompolas P, Mesa KR, Kawaguchi K, Park S, Gonzalez D, Brown S, Boucher J, Klein AM, Greco V (2016) Spatiotemporal coordination of stem cell commitment during epidermal homeostasis. *Science* 352: 1471 – 1474

Roy E, Neufeld Z, Cerone L, Wong HY, Hodgson S, Livet J, Khosrotehrani K (2016) Bimodal behaviour of interfollicular epidermal progenitors regulated by hair follicle position and cycling. *EMBO J* 35: 2658 – 2670

Roy E, Wong HY, Villani R, Rouille T, Salik B, Sim SL, Murigneux V, Stark MS, Fink JL, Soyer HP *et al* (2020) Regional variation in epidermal susceptibility to UV-induced carcinogenesis reflects proliferative activity of epidermal progenitors. *Cell Rep* 31: 107702

Ruetze M, Gallinat S, Wenck H, Deppert W, Knott A (2010) In situ localization of epidermal stem cells using a novel multi epitope ligand cartography approach. *Integr Biol* 2: 241

Sada A, Jacob F, Leung E, Wang S, White BS, Shalloway D, Tumbar T (2016) Defining the cellular lineage hierarchy in the interfollicular epidermis of adult skin. *Nat Cell Biol* 18: 619 – 631

Sanchez-Danes A, Hannezo E, Larsimont JC, Liagre M, Youssef KK, Simons BD, Blanpain C (2016) Defining the clonal dynamics leading to mouse skin tumour initiation. *Nature* 536: 298 – 303

Satija R, Farrell JA, Gennert D, Schier AF, Regev A (2015) Spatial reconstruction of single-cell gene expression data. *Nat Biotechnol* 33: 495 – 502

Shen Y, Chan G, Xie M, Zeng W, Liu L (2019) Identification of master regulator genes of UV response and their implications for skin carcinogenesis. *Carcinogenesis* 40: 687 – 694

Subramanian A, Tamayo P, Mootha VK, Mukherjee S, Ebert BL, Gillette MA, Paulovich A, Pomeroy SL, Golub TR, Lander ES *et al* (2005) Gene set enrichment analysis: a knowledge-based approach for interpreting genome-wide expression profiles. *Proc Natl Acad Sci U S A* 102: 15545 – 15550

Taniguchi H, He M, Wu P, Kim S, Paik R, Sugino K, Kvitsiani D, Fu Y, Lu J, Lin Y *et al* (2011) A resource of Cre driver lines for genetic targeting of GABAergic neurons in cerebral cortex. *Neuron* 71: 995 – 1013

Trapnell C, Cacchiarelli D, Grimsby J, Pokharel P, Li S, Morse M, Lennon NJ, Livak KJ, Mikkelsen TS, Rinn JL (2014) The dynamics and regulators of cell fate decisions are revealed by pseudotemporal ordering of single cells. *Nat Biotechnol* 32: 381 – 386

Tumbar T, Guasch G, Greco V, Blanpain C, Lowry WE, Rendl M, Fuchs E (2004) Defining the epithelial stem cell niche in skin. *Science* 303: 359 – 363

Vasioukhin V, Degenstein L, Wise B, Fuchs E (1999) The magical touch: genome targeting in epidermal stem cells induced by tamoxifen application to mouse skin. *Proc Natl Acad Sci U S A* 96: 8551 – 8556

Wang S, Drummond ML, Guerrero-Juarez CF, Tarapore E, MacLean AL, Stabell AR, Wu SC, Gutierrez G, That BT, Benavente CA *et al* (2020) Single cell transcriptomics of human epidermis identifies basal stem cell transition states. *Nat Commun* 11: 4239

Watanabe M, Natsuga K, Nishie W, Kobayashi Y, Donati G, Suzuki S, Fujimura Y, Tsukiyama T, Ujiie H, Shinkuma S *et al* (2017) Type XVII collagen coordinates proliferation in the interfollicular epidermis. *Elife* 6: e26635

Webb A, Li A, Kaur P (2004) Location and phenotype of human adult keratinocyte stem cells of the skin. *Differentiation* 72: 387 – 395

Binary organization of epidermal basal domains highlights robustness to environmental exposure

Sangeeta Ghuwalewala*, Seon A Lee*, Kevin Jiang, Joydeep Baidya, Gopal Chovatiya, Pritinder Kaur[2], David Shalloway and Tudorita Tumbar[#]

[*]Equal contributions

Department of Molecular Biology and Genetics, Cornell University, Ithaca, NY, USA

[2]Curtin Medical School/Curtin Health Innovation Research Institute, Curtin University, Perth, WA, Australia

[#]Corresponding author, tt252@cornell.edu

APPENDIX MATERIAL

- **Appendix Figures S1-5 (pages 3-10)**

- **Appendix Figure S1-5 Legends (pages 4-11)**

- **Appendix Tables S1-3 (pages 12-61)**

Appendix figure and figure legends

Appendix Figure S1 (Associated with Figure 4)

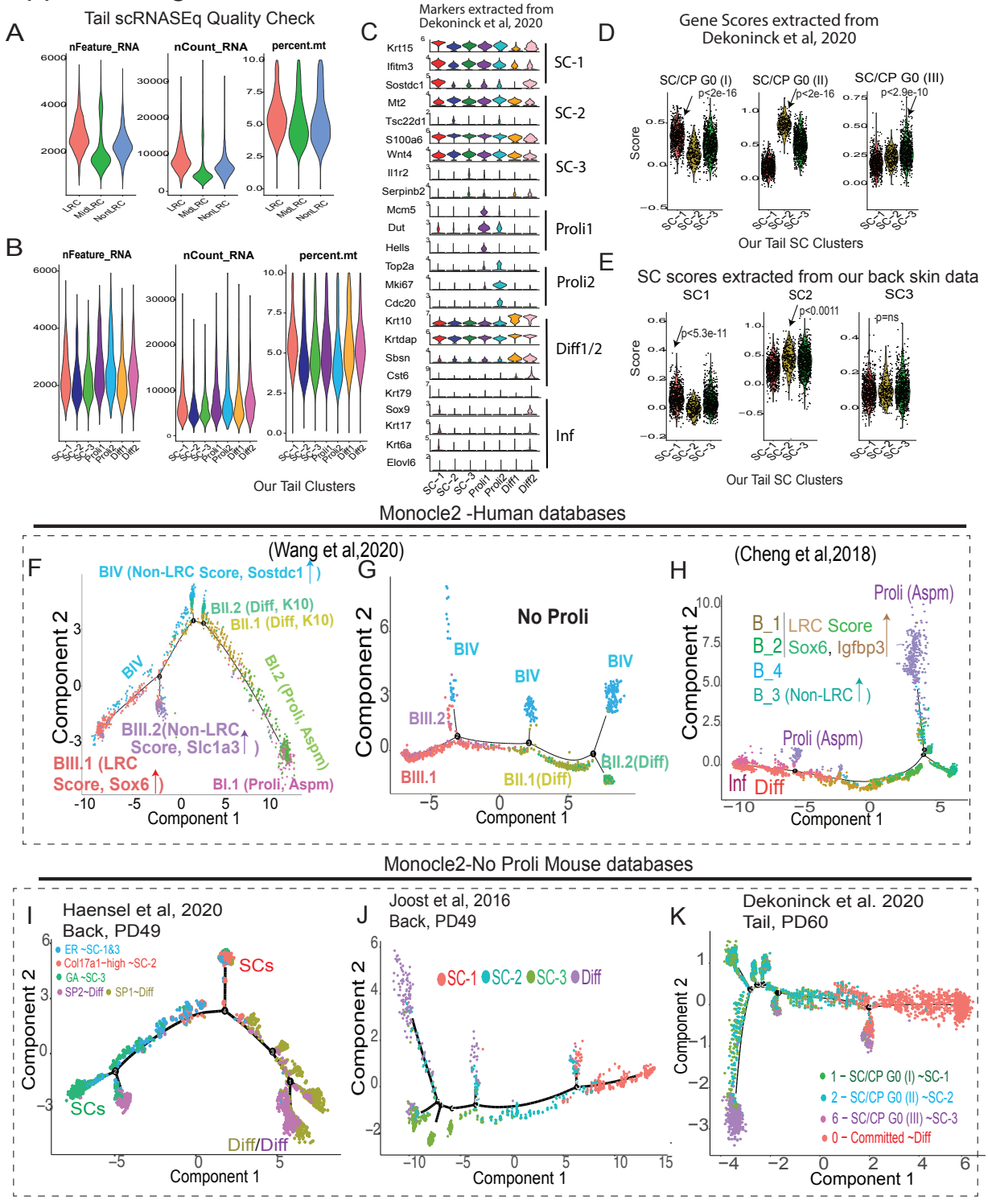

Appendix Figure S1:

Tail and human skin scRNA-seq analysis of sorted basal LRCs, Mid-LRCs, Non-LRCs (Associated with Figure 4)

(A, B) (A) mRNA or gene count and percent mitochondrial genes showing the quality controls for cells used for scRNA-seq analysis are shown as violin plots for the tail sorted samples from 2 replicates and its (B) seven clusters.

(C, D) (C) Violin plots showing expression of genes to assign cell identity to each cell cluster and (D) SC gene scores extracted from (Dekoninck *et al*., 2020). These data indicate correlations amongst the 3 SC populations from our tail databases. P value was calculated using pairwise Wilcoxon rank-sum tests with Benjamini-Hochberg correction.

(E) Correlations of our tail and back skin SC clusters. P value was calculated using pairwise Wilcoxon rank-sum tests with Benjamini-Hochberg correction.

(F-H) Lineage trajectory using Monocle 2 showing all clusters (F) or non-proliferative only clusters (G) from human foreskin (Wang *et al.*, 2020) and all clusters from adult human scalp (Cheng *et al*., 2018) (H).

(I-K) No Proli(ferative) clusters extracted from published databases as indicated (Dekoninck *et al.*, 2020; Haensel *et al*., 2020; Joost *et al*., 2016) used to generate Monocle 2 lineage trajectories.

Appendix Figure S2 (Associated with Figure 5)

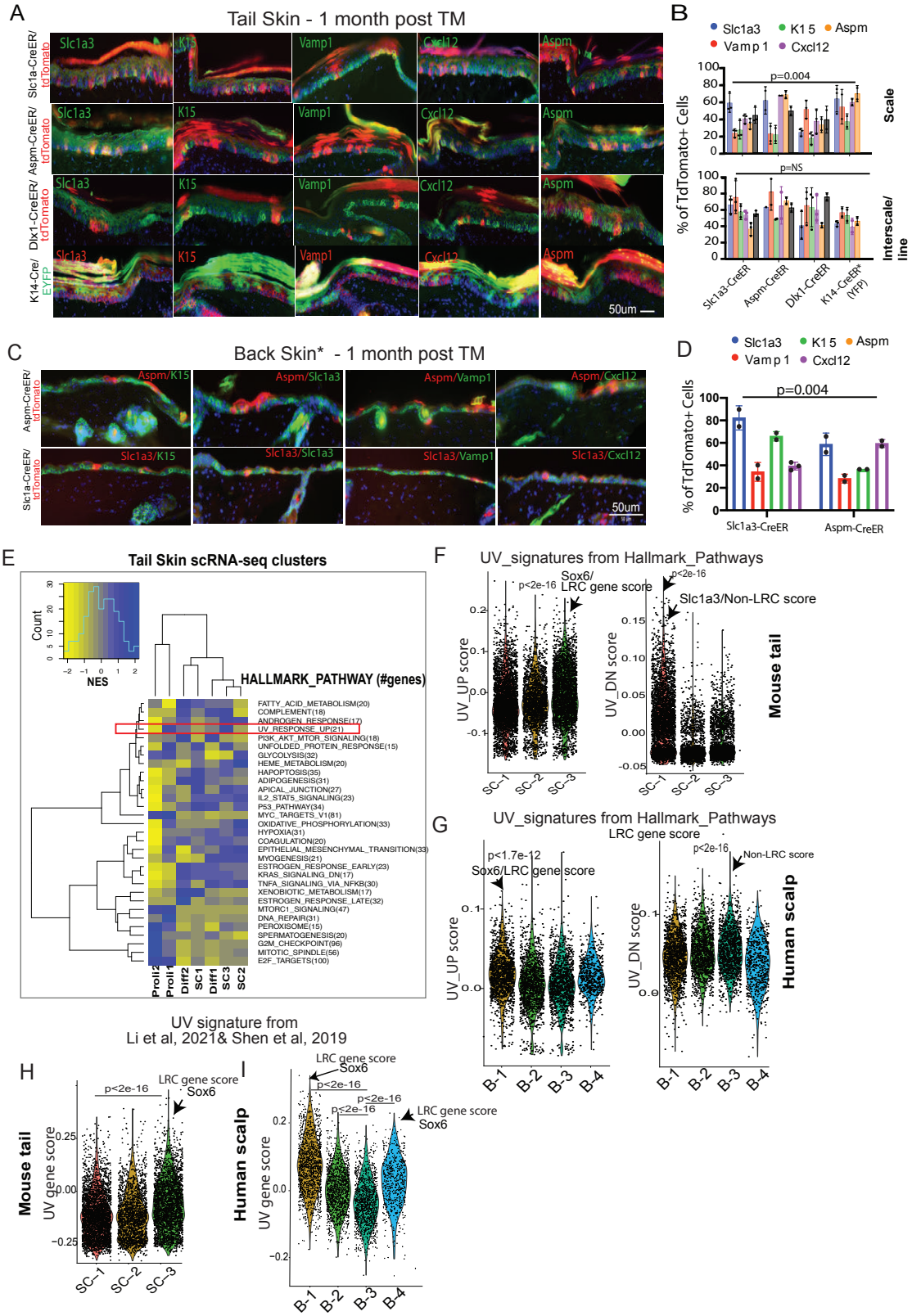

Appendix Figure S2:

Molecular characterization reveals the distinct nature of IFE population and differential expression of UV-response genes (Associated with Figure 5)

(A) Images showing immunofluorescence staining of all the IFE markers within the lineage-traced Slc1a3-CreER, Aspm-CreER, Dlx1-CreER and K14-CreER basal cells in the tail epidermis. Scale bar~200 μm.

(B) Fraction of tdTomato^{+} (EYFP for K14-CreER) cells positive for the respective markers in scale vs interscale for N= 2 or 3 mice per experiment (6-7 images per mouse). Error bars are SDs. P-values calculated by Student's t-test (mixed effects model)

(C) Images of back skin stained for indicated markers show co-localization in lineage-traced Slc1a3-CreER and Aspm-CreER labeled progenies (asterisks indicate back skin equivalence). Scale bar=50 μm

(D) Quantification of data in (C). Error bars are SDs. P-values calculated by Student's t-test (mixed effects model) from 2 mice and 5-6 images per replicate.

(E) Heat map of pathways differentially expressed in scRNA-seq clustered generated from mouse tail skin shows differential regulation of UV-response genes.

(F, G). Hallmark_Pathway of UV-UP or DN regulated genes in mouse tail (F) and (G) human scalp. Note UV-UP gene scores is higher in the SC clusters with high Sox6 and LRC gene expression scores. P value was calculated using pairwise Wilcoxon rank-sum tests with Benjamini-Hochberg correction.

(H) Similar analysis as in (F,G) but with a different UV-gene signature (Dataset EV1) extracted from studies indicated shows enrichment in the Sox6 clusters, which is located in the more exposed epidermal regions.P value was calculated using pairwise Wilcoxon rank-sum tests with Benjamini-Hochberg correction.

Appendix Figure S3 (Associated with Figures 5/6)

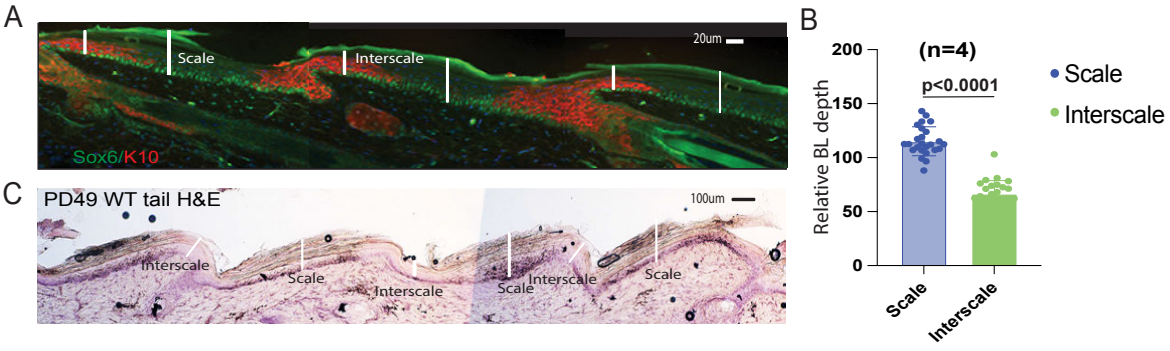

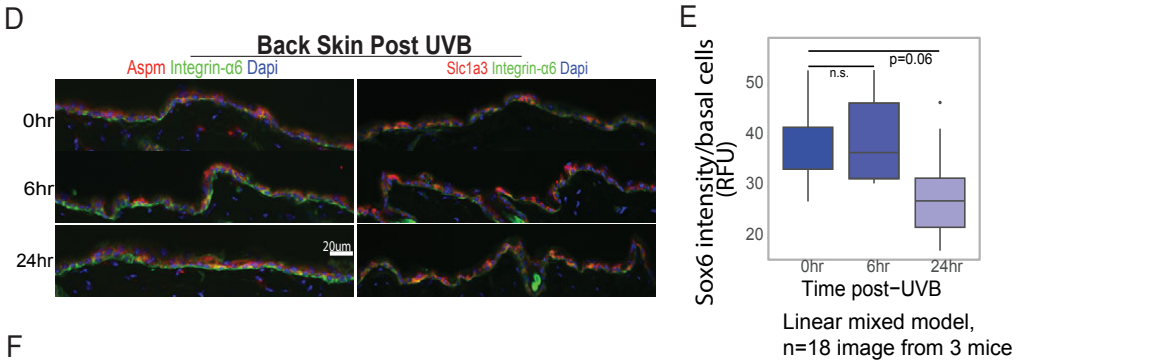

F

SOX6-low cells (in the non-LRC domain) become SOX6-high.

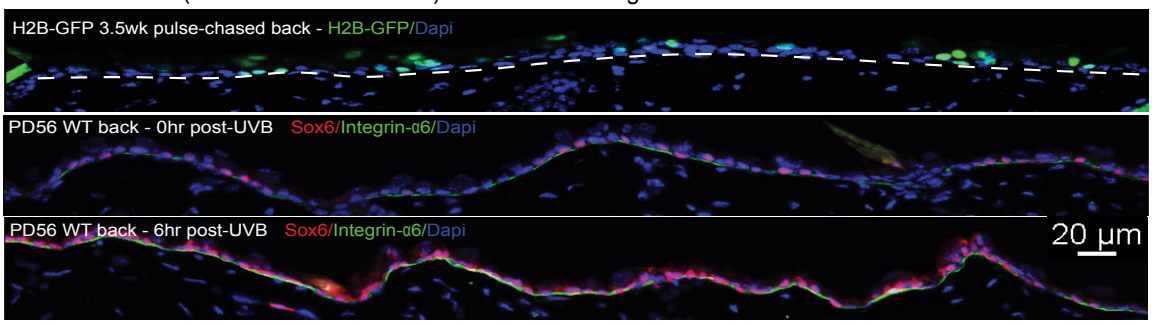

Appendix Figure S3:

Thickness of scale vs interscale and expression of LRC/non-LRC genes in response to UVB (Associated with Figure 5)

(A, B) (A) Images showing the long view of tail skin with Sox6/K10 staining used to measure the basal layer depth of scale vs interscale, quantified in (B). Scale bar =20 μm; lines indicate examples of depth measurements obtained at scale and interscale from N= 4 mice (6-7 images per mouse). Error bars are SDs. P-values calculated by Student's t-test.

(C) H&E images of the same tissue. Scale bar on right top = 100μm.

(D) Expression of Aspm and Slc1a3 in the basal layer of back skin at time points after acute UVB exposure show no apparent changes.

(E) Box plot of average Sox6 intensity changes in $Sox6^{high}$ basal cells in response to UVB. RFU=relative fluorescence unit. Central band is the mean value, the top of box indicates 25th percentile, while the bottom of the box indicates 75th percentile. Whiskers indicate minimum and maximum values in the data, with dots indicating potential outliers. Linear mixed model statistical test was used with data from 18 images from 3 biological replicates.

(F) Representative long-view immunofluorescence images of LRC clusters in back skin, compared to similarly sized $Sox6^{high}$ clusters interspersed with $Sox6^{low}$cells during homeostasis (0hr UVB); note larger $Sox6^{high}$ clusters at 6hrs post-UVB demonstrating that $Sox6^{low}$ cells acquire $Sox6^{high}$ levels. % Sox6 high cells are quantified in Figure 5H. Dashed line indicates basement membrane.

Appendix Figure S4 (Associated with Figures 5/6)

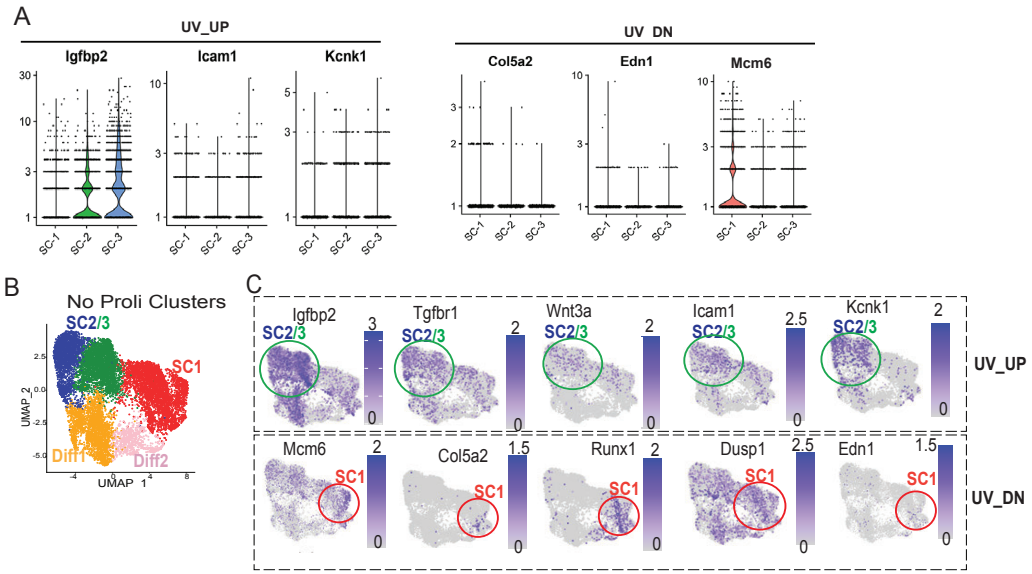

Appendix Figure S4:

Expression of UV signature genes in scRNAseq clusters (Associated with Figure 5/6)

(A-C) Violin (A) and feature plots (B-C) of individual genes listed in the UV regulated signatures that show differential expression in the different SC clusters.

Appendix Figure S5 (Associated with Figure 6)

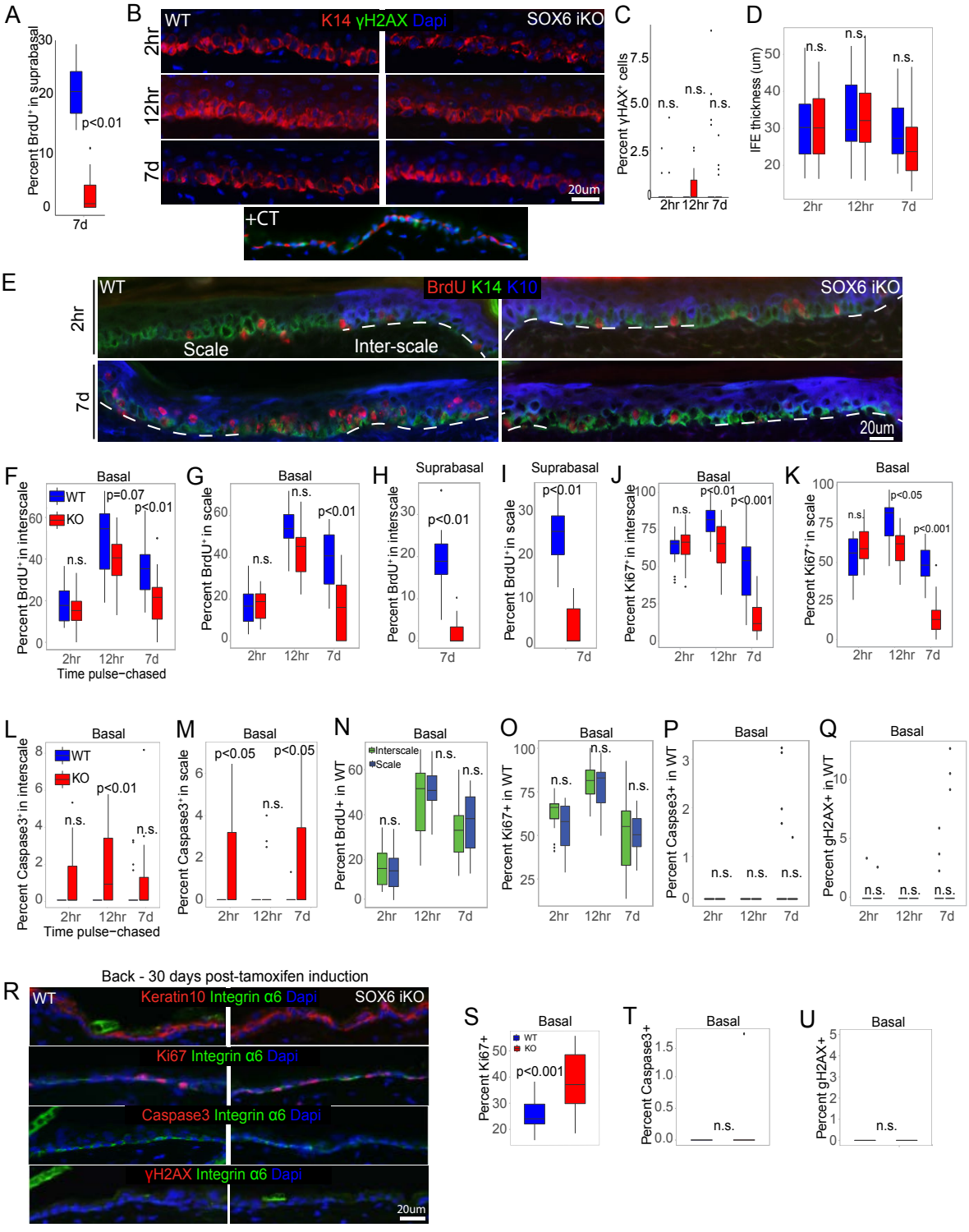

Appendix Figure S5:

Sox6-loss of function phenotype in mouse skin (Associated with Figure 6)

(A) BrdU counts of suprabasal cells from tail skin complementing data in Figure 6 B,C.

(B) Staining for a DNA damage marker gH2AX of skin sections from BrdU pulse-chase mice scheme shown in Figure 6A. Irradiated skin was used as positive control (CT) for the antibody staining.

(C) Boxplot of quantified DNA damage marker gH2AX data from BrdU pulse-chase sample images like those in (B).

(D) Measurements of IFE thickness based on $K10^+$ stains in skin from the BrdU pulse-chase experiment at time points indicated in Figure 6A.

(E) Images showing BrdU-labeled cells in scale or $K10^+$ interscale, from experiment in Figure 6A. Dashed line indicates interscale.

(F-M) Box plots showing percentages of BrdU marked cells in basal (F,G) or suprabasal layer (H,I), as well as of proliferation (J,K) and apoptosis (L,M), split per scale vs interscale from BrdU pulse-chase experiment sample images like those in (E).

(N-Q) Box plots showing percentages of BrdU marked cells (N), cell proliferation (O), apoptosis (P), or DNA damage (Q), comparing scale vs interscale in wild type (WT) skin.

(R) Immunofluorescence images for differentiation (K10), proliferation (Ki67), cell apoptosis (Caspase3), or DNA damage (gH2AX) marker from WT or Sox6 iKO back skin samples harvested 30 days post-tamoxifen induction.

(S-U) Boxplots of cell proliferation (S), apoptosis (T), or DNA damage (U) data quantified from 30-day post-tamoxifen induction skin samples images like those in (R).

Data information: In box plots central band is the mean value, and the top indicates 25th percentile while the bottom indicates 75th percentile. Whiskers indicate minimum and maximum values in the data, with dots indicating potential outliers. Linear mixed model statistical test was used with data from 18 images from 3 biological replicates.

Appendix Tables

Table S1: Characterization of all the human samples used in the study:

Human Samples	Site on Body	Age	Slc1a3	Frequency of patches (Dermal papillae vs rete ridges)	K15	Ki67 staining	Vamp1
A	Female Chin	61	weak	very rare and small patches	partially colocalised	Not colocalised	
B	Male Scalp	70	Didn't work				
C	Male temple	66	Moderate	Few patchy regions (abnormal skin)	Co-stained with Slc1a3	Co-localised in some regions	
D	Male Cheek	59	Strong	Patches around keratin pearls	Not clear	Ki67 underneath	
E	Male ear	88	Strong	Frequent Patches around keratin pearls and tips of rete ridges	Co-stained with Slc1a3	excessive Ki67 (tumor-like)	
F	Female forehead	82	Very strong to strong	Few Patches in the flattened epidermis	With or without Slc1a3	-	
G	Male ear	76	Moderate	small intense patches			
H	Female Scalp	76	Strong	Very rare and small patches	Co-stained with Slc1a3	Very few positives	
I	Female forehead	75	Very strong	Mostly infundibulum and tips of epidermis	opposite to K15		
J	Male Scalp(SCC)	82	Didn't work				
K	Male Ear	79	Didn't work				
L	Male cheek	81	strong small patches	Sometimes in dermal papillae (not clear as the skin is flat)	Strikingly opposite to K15 at some places (2 out of 6 images)	In patches more frequently near K15	Exclusive of K15 (5 out of 9 images) remaning 4 images show co-staining but K15 but not

							completely co-localised, K15 is present in rete ridges where Vamp1 expression is low
M	Male arm	59	Moderate				
N	Female forehead	90	moderate	Keratin pearls and dermal papillae			
O	Male scalp	82	moderate				Vamp1 colocalise with K15 to some extent in the dermal papillae
P	Female Scalp	60	very small to longer patches	extends across the flat rete ridges	K15 is highly intense in rete ridges		Vamp1 colocalise with K15 to some extent in the dermal papillae
Q	Female Forehead	57	small patches	in rete ridges	K15 seems to be present in dermal papilae occasionally		Vamp1 colocalise with K15 to some extent in the dermal papillae
R	Male ear	80	Didn't work				
S	Male temple	65	Lack of epidermis				
T	Male neck	70	strong small patches	Long stretch at some regions	K15 is extended across the rete ridges colocalise with Slc1a3	In patches more frequently under K15 BL	
U	Male arm	85	Weak to moderate	small patches	rete ridges and juctions between dermal papillae and ridges	K15 colocalses with Slc1a3 even through dermal papilae	Vamp1 is occassionaly presnt in rete ridges along with K15
Newborn (6)	Foreskin		Moderate	Homogenous expression throughout he basal layer	Homogeneous	very abundant	Also Homogenous
21 year old (2)	Breast		High around rete ridges	Correlated with Slc1a3 at some patches	Present in rete-ridges and DP junctions	Present in basal and suprabasal layers	in Inter-ridges

30 year (2)	breast		Strong patches at tips of rete ridges	Mostly co-stain with Slc1a3	Present in rete-ridges	Present in basal and suprabasal layers	in Inter-ridges
33 year	breast		Tips of rete ridges	Mostly co-stain with Slc1a3	Present in rete-ridges	Mostly suprabasal	in Inter-ridges
41 year (2)	breast		Didn't work				
45 year (2)	abdominal		moderate at rete ridges	Mostly co-stain with Slc1a3	Present in rete-ridges	Mostly suprabasal	in Inter-ridges
52 year old	abdominal		moderately lost; flattened skin	Correlated with Slc1a3 is low	Present in patches	lost significsnlty	in Inter-ridges to some extent

Table S2: Bulk-RNAseq genes

Tail Skin						Back skin					
Aspm_ T<1	**Aspm_ T>1**	**Dlx1_ T<1**	**Dlx1_ T>1**	**Slc1a3_ T<1**	**Slc1a3_ T>1**	**Aspm_ B<1**	**Aspm_B >1**	**K14_ B<1**	**K14_ B>1**	**Slc1a3_ B<1**	**Slc1a3_ B>1**
GREM1	SYT4	FABP4	RASSF2	GREB1	KPRP	LMCD1	TACR3	FBLN2	PLPPR4	NR1H4	CLDN3
IL31RA	COCH	DIPK1C	IL18	LPAR1	MYO5C	EYA2	IL10RA	PPP1R16B	DAB2	MC3R	RGS1
SORBS2	BEAN1	FBXL7	SULT4A1	CCL2	ACSBG2	CD34	FADS2	KCNE4	USH1G	NKX2-1	WNT2
SYNPO2	CLCA1	TMEM47	PALM2	RASGRF1	RNF223	C2orf88	FAM19A3	GRID2IP	SPINK6	SELE	CNTNAP2
GPRC5D	FGL2	SNX10	VWCE	CA8	GFRA3	LHX2	ALDH3B1	DIPK1C	NKX3-2	PLPPR4	SYCP1
WIF1	SPI1	CCL7	FSD1	SLC27A6	DNAH3	DAB2	PCDH17	PCDH19	APOBEC1	GATA2	CD3D
FBN1	TARM1	KRTAP26-1	MRC1	VIT	KBTBD12	GREB1	TBC1D30	RGS18	SCARNA8	TAS2R60	LNP1
VIT	ERP27	PTGER2	SLC2A2	DIPK1C	AGR3	MYO5C	CYBB	MFRP	PEX5L	CRB2	CCDC60
AMER2	CCDC177	CLDN15	CCDC198	C9	ADGRG3	FSTL1	MRC1	MTCL1	COL6A5	USH1G	BDNF
MIR186	NCKAP1L	SELP	MMEL1	LRRTM4	ACTA1	LRRC4	POU2F2	ASTN1	MROH7	LEAP2	WSCD2
SLC35D3	LRRC10	MMRN2	FGG	PKD1L3	NRAP	PTPRB	TMEM271	TMEM74B	HYAL4	GABRB2	GABRA4
PHEX	HRASLS	ARMCX6	RGS5	KIF1A	S100B	FABP4	OSR2	LRRN1	IL23R	GRIN2B	GCKR
DACT1	PRR29	ZFP37	PTPN7	ARMCX2	MYL7	IL31RA	GPR171	GRIA3	SFTPC	BCAT1	PHEX
CHST13	LOXL1	GFRA1	BIN2	IL1A	CILP	CD36	C5orf52	CNKSR2	NOS1	MGAT4C	SERPINB13
SLC4A5	SNORD73B	FGD5	NOXA1	CACNA2D2	NFASC	FBLN5	GJB1	SDSL	SHISA4	LRCH2	ST8SIA4
HOXD13	TM4SF4	ACKR1	CEL	SLCO2B1	UNC80	FBLN2	APOA1	CHI3L1	RASSF2	GRM2	FGF7
ST6GAL1	SLC17A8	CYTL1	CCDC105	FZD4	CLDN7	DIPK1C	SLC14A2	ITM2A	ST8SIA4	CDH12	RF00019

TTLL9	SCN1A	IL18R1	RF02271	NPTX1	GCNT4	NKX2-1	ESPNL	PCSK9	RF00019	FGR	EDNRB
CFAP54	CA6	WIF1	NPM2	FGFR4	KIAA1211	PPP1R16B	EFHC2	SH2D3C	EDNRB	GALNT15	ANGPT2
CRYBA2	RNY3	HIF3A	CA7	CNGB1	KCNIP2	KCNE4	SLC9B2	LYN	ANGPT2	VAX2	SEBOX
PCDHGA11	CACNG1	RAB33A	LHX9	HS6ST2	HES2	SELE	PRDM1	4-Sep	LRRC24	BDKRB1	KRT25
EMILIN3	HIST2H2AB	FGD3	INSC	ITGA1	PROZ	GATA2	SMARCA1	ENTPD1	TSSK2	LRRC3B	HSD11B1
SHD	KCNS1	LRGUK	APLNR	G0S2	SPATA9	S1PR1	GLRA4	ARHGEF15	LY75	NKX3-2	CYP1A1
CDH6	C1QTNF3	GRIA2	ARL11	SRPK3	SLC44A4	CA8	STK31	LNP1	CLDN7	SCARNA8	ACTL9
ALDH3B1	TNIP3	GALNT16	GLP1R	TMEM47	POMC	COCH	SNORD121B	ACOT4	KRT25	FRZB	RBP7
KLHL41	ARMC3	SPINK6	MS4A1	PYY	TH	WIF1	CCKBR	CDH5	ZNF641	CDH20	FBLN5
CXCR4	LRRC10B	THSD7A	MCHR1	LY75	LIMS2	MGAT4C	CD79A	LINGO1	KCND3	GRIN2A	DCLK3
LDB2	FBXO41	DMC1	PROK1	ADCY4	TMEM229A	LRCH2	PPP2R2B	DLX1	HHIPL2	ZIC3	KCNN3
FIBCD1	IL2	GALNT15	DOK6	HOXC8	OCA2	FGR	BHLHA15	EBF2	MAP7D3	SEZ6L	SLC18A1
FBLIM1	SLC25A34	EMILIN2	RIMS2	CRISPLD1	ZC3H12B	KIF1A	BOLL	NWD2	LCT	CHRNA1	TCHHL1
TRPM6	ARMC2	TMEM217	MPP4	GJC1	SLA2	BDKRB1	SLC16A12	OPCML	IL18RAP	RBP3	PRKG2
ABHD16B	KIAA1755	S1PR1	KCND2	ENPP3	DPEP1	TMEM47	CRYBA2	ADRA2A	SLA	UGT8	MAP7D3
SCARNA6	ARMH2	ARR3	CAP2	EPHB1	SLC9A2	SCARNA8	NTRK3	CFAP100	SLC51A	ESRRB	IL18RAP
MAP3K13	SEMA6B	MIR26A1	KDM4D	GXYLT2	HIST1H2BD	DNAH3	TMEM44	LRAT	CCDC114	PEX5L	BFSP2
EID3	CCDC40	PGLYRP3	SCRT2	FABP12	CAPN3	MTCL1	ATOH1	ZAP70	KLK14	ACTRT3	ST3GAL5
KIAA1614	WDR93	GABRB1	SLC38A1	ST6GAL1	MTCL1	FGL2	FATE1	STXBP5L	GALNT16	RGS21	ARHGAP40
MAP1A	CMA1	SOX30	MYL7	GABRD	FLG	GRIN2A	PAX5	MMP16	FLI1	EPHA6	CA2
NTN3	PROM1	CCM2L	LTB	GNAT1	RCAN2	LRRN1	NFE2	CACNA2D1	NR5A2	KCNT1	MFNG
SLC1A2	SYNPR	SHISA7	B3GALT2	SPRY3	ITGB1BP2	KRTAP26-1	SYNDIG1L	ZNF521	CDH6	GDF2	LYVE1
GNG2	NR2F1	KRT26	SYT13	LCT	HPX	PTGER2	CCER2	ITGA11	TNFSF8	SLC18A3	VCAN
HIF3A	MYT1	AIM2	TMEM150B	SYNPO2	FAM71F2	ACKR1	SLC5A7	EPHA7	ZNF784	COL6A5	USH2A
PRR15	CXXC4	MINAR1	FBXL13	FAT4	C6orf222	CNKSR2	RNU6-580P	WIF1	APOA1	RF02271	TSGA13
KRTAP15-1	MAP3K15	HFM1	SLCO1C1	PPP1R9A	ADM2	HS6ST2	TNFSF4	KIRREL3	LCP2	NHLH2	EREG
SLC7A3	C10orf90	GIMAP1	DMBT1	NXPE2	AMER2	IL18	CD244	HIST1H1B	FAM83E	AMBP	KCNJ6
FOXP3	HGFAC	CADM3	LUM	SLA	DTNA	LYN	SORCS3	FBN2	ATP8A2	CDH19	RAB39A
TEX14	NOVA1	CHST1	HPD	SCNN1G	KCNH6	SLC35D3	WFDC1	GNG11	KRT73	MROH7	CDH22
THEGL	ONECUT2	PODXL	FKBP6	LRRC8C	FNDC11	SELP	SLAMF1	PTPN18	IL17F	HYAL4	TRIM36
UPK3B	HPD	ISLR	TBX15	HOXB13	CELA1	SULT4A1	CD69	RNF125	CCDC40	IL23R	IL5
NES	C1QB	TESPA1	SLC6A11	CCDC114	SPATA17	PALM2	RS1	C1QA	TRPM6	C1orf158	OMG
EIF4EBP3	C11orf87	FAM180A	PAX6	GPC6	TEX54	4-Sep	RN7SKP197	SCUBE1	LHFPL4	ZFPM2	KCND2

PLD6	ARL11	C1orf115	TMEM26	TTC21A	BST1	LRRC24	RRAGB	GALNT13	FAM184B	OR13C8	FIGN
HTRA4	MYO1G	HHIPL1	EBI3	INPP5J	SLC8A2	MMRN2	GYPC	SV2B	CMA1	GABRA1	CDH8
FAM217A	PTGIS	EYA1	VNN3	NRCAM	CREB3L3	SLC10A6	SPNS3	RGS5	TFR2	RORB	CPA6
GPRIN1	ASB2	RFX8	MMP9	MIR186	MMP24	ENTPD1	INA	SYT14	MAK	OLIG3	HHIP
DTNA	ARHGAP20	PTGDR2	GLTPD2	PRDM6	CDH15	ARHGEF15	CACNA1F	FLT4	SCARNA6	SALL1	TNFSF8
ARL13A	TYROBP	TRIM17	AREG	TRAF3IP3	CD86	NRAP	KRTAP7-1	TEK	CAPN3	USP44	ADORA3
C20orf144	RFTN2	RAB17	CXCR5	TNFAIP6	B4GALT6	S100B	MINAR2	PLD5	HS6ST2	AGMAT	C7
IGF2BP2	PTPRR	SLAMF9	VIL1	IL4	GNG11	UNC80	ZAN	RGS7	AIM2	EBF3	MOGAT1
FSTL4	REC8	FUT9	P2RY4	PLEK	DSCAML1	EMCN	EDNRB	SHD	RCAN2	PDGFRL	PPP1R9A
KCNH4	SDSL	IQCA1	ASB11	SCNN1B	PWWP3B	JAM2	STUM	OMP	MAMDC2	SCARNA11	BHLHA15
TIE1	LEAP2	RNASE12	STUM	MLXIPL	SLC19A3	NHLH2	SHISAL1	NEK5	TESMIN	ARHGAP15	FAM83E
RNF182	MCOLN2	LRRTM4	LHX3	CCK	HPD	ADCY4	SMIM32	PODNL1	BTBD18	SFTPC	ACOX2
XCR1	TRIM67	GRM7	ARHGAP30	CCL24	ADORA3	CDH5	KRT84	HSD17B13	INSM2	NOS1	ATP8A2
C13orf42	VSTM2A	EGR4	SLC25A34	GRXCR2	SNX31	CRISPLD1	DGKG	SLC38A5	ARHGEF25	MIR200C	KRT84
AC020613.1	KIAA1324	SERPINI1	ERP27	RYR2	ACTBL2	LINGO1	NR5A2	COLGALT2	GABRR2	SFRP4	SLC45A2
LANCL3	SLC41A2	KCNU1	LRIT1	Z98752.3	ERBB4	FGD5	MMP13	FAM228A	GNG2	ANKS4B	DMTN
ZNF853	GABRA4	TSPYL5	TRIM50	NCF4	CLCN1	KCNB1	MAP7D2	PODXL	SMIM22	SNORA12	ADCY2
M1AP	FAP	SNPH	MIR181C	PTPN5	CPA3	SNORD73B	NHSL2	SLAIN1	CLIP3	RNU6-1109P	SGIP1
NPM2	RNASE6	PIGR	GALNT17	TBC1D30	FAM107A	ENPP3	NTN3	CADM2	COL14A1	CCDC158	ART5
OTOGL	TMPRSS11A	SHOC1	MDGA2	ADAMTS3	RGSL1	CYTL1	STAC2	TENM1	APLNR	LRRC4C	C1orf146
FGD3	GPIHBP1	ADGRL4	CCL22	CNN1	RF00026	CLDN3	CPNE1	NTRK3	SPACA1	PAX2	TNNT1
HES2	PSCA	ST6GAL1	FAM237B	CD3D	NHLH2	CFAP100	GSC	LEAP2	C20orf96	VSX2	CD19
GNG4	LMOD2	PIK3R5	C16orf54	HHATL	KCNH4	FAM107A	ATP8B3	SLC6A15	MCHR1	VSTM2L	LY9
AC055839.2	LTF	PHYHD1	SLA2	SLC38A5	GFY	CA6	TNFSF12	MME	LANCL3	LTA	IL17F
DPT	KRT20	CAMK4	FSD2	SOX18	HGF	LRAT	LRRC15	CACNG2	MCOLN2	ROS1	MGAM
TAS1R1	TMEM145	SBSPON	MIR26A2	UPK2	EDNRB	EBF3	IMPG1	XIRP2	KCNF1	TLL2	CRMP1
MAP7D3	MDGA2	EFHD1	MYPN	PCDHGA1	COL28A1	ZAP70	C8A	SOBP	EMX2	SELL	CNTN2
GCNT7	PIGR	IGF2BP2	GUCA1B	GIPR	GRIA3	SPRY3	PCDH8	TRHDE	GPRIN1	TRPC7	CREB3L3
GALNT9	MYH7	ZNF423	MASP2	SYPL2	MAP6D1	CACNA2D1	LMOD1	CSMD1	GJB1	RNU1-43P	JCHAIN
LYL1	SLC44A4	TSPAN15	GRID2	NPB	NMNAT2	ZNF521	UTS2	KCNC1	GPAT2	FBN1	FAM184B
AGTR2	CHP2	TRIM36	SPAAR	CARMIL3	APLNR	HIF3A	APOD	CLGN	NT5C1B	IGF2BP1	TFR2
CORO6	MYH11	CITED1	CAPN11	PLA2G4B	SLC6A3	ARHGAP15	STK32A	RN7SKP127	MMP24	KCNH8	ESR2

STC2	NHLH1	PCDHGB1	ATP8B3	BTBD18	LYL1	RAB33A	FRMD5	OTOP1	CLMP	TSSK2	THBS4
MAL	KCNJ10	AKAP6	STX1B	SRPX	TREH	CYYR1	MYO16	S100A2	RNASE12	CPNE6	SAP25
PTPN22	SLIT2	PKHD1L1	NID2	RTL5	RASL12	SFTPC	MIR708	MDGA2	B4GALT6	GATA4	RNF183
UCP3	KIAA1549L	MOS	CYTIP	SBSPON	METTL24	RNY3	SLC9A2	SOD3	RAB26	ADGRA1	ZGLP1
TFPI	SLC26A7	SYT5	MLANA	MISP	RETN	FAT4	DCLK2	TECTA	SYT5	ATOH1	GABRR1
TTLL6	NELL2	EID2	NCCRP1	BMPER	MAP7D2	HIST2H2AB	KRT76	RFLNA	TH	R3HDML	PLD5
SV2C	FRMPD3	HTR6	TEX49	KSR2	SMIM41	AKAP12	COL9A2	CMBL	SERPINI1	SERPIND1	PHLDA2
TET1	ZNF366	TMPRSS6	GUCY1B1	SAMD15	RNF207	SLA	ARR3	EMCN	PSMA8	ZNF641	DNAH10
RASGRP4	PTX3	FIBCD1	PADI2	CXCL10	ADAMTS19	FBN2	LEAP2	GFRA2	CRISP2	SPARCL1	HS6ST2
DOK2	NXNL1	PARVG	CD79A	DSG4	PJVK	GNG11	STXBP5L	TMEM132C	SH2D6	MYH7B	FEZF2
GPR22	SLITRK1	SLC41A2	MMP12	RASSF4	BCL2L10	CCDC114	CPS1	SLC29A4	LTF	GLRA2	PRR9
PGLYRP2	ZP1	CCDC40	OCA2	KRT8	C2orf74	ADGRL4	CD48	SNORD15A	PRTN3	MIR150	TRANK1
LRRTM4	TMPRSS12	PSD2	TECTA	C1QTNF6	FRMD7	SLC2A2	HTR1F	PRR9	C9orf43	KCND3	KRT36
PNMA2	GHSR	KLF14	SNORD666	BHLHA9	LMX1A	INPP5J	CADM4	ILDR2	SPATA17	MIR26B	RF00026
HIST1H4E	SPACA4	IL17C	PJVK	KCNG2	LGI2	PROZ	C4orf54	RARRES2	ITK	PCDHA10	GFPT2
HTR1B	MIR193B	CD96	CARD11	CD163	SKOR1	NRCAM	SNORD71	PGBD5	CAMK4	CD300LG	HNF1A
ARR3	CLHC1	HRC	ALPK2	BRINP1	GFPT2	SV2B	THEMIS	C21orf62	XIRP1	PTGDR2	RECK
CCDC168	NGB	GULP1	MAT1A	NACAD	RNU6-384P	SPATA9	ITGBL1	DIO3	PIWIL1	PCDH12	TMEM132C
SLCO5A1	CD3D	SMIM22	SLC45A1	STRIP2	RNF17	ANKS4B	OLR1	NTNG1	EFHC2	PCSK2	CD180
GUCY1B1	SPATA46	HEY2	FSCN3	TACR1	MYL10	TEK	ATP8A2	UPK2	M1AP	FOXB1	GPRASP2
COX4I2	CD19	WFIKKN2	SEMA5B	ATP2A3	DYNLRB2	TRAF3IP3	TUBAL3	RNF182	NPW	RYR2	GALNT14
FUT4	SLC1A1	LRRC10	RGS17	LIPH	FOLR1	SHD	FGF17	DBN1	AVPR1B	PTCH2	CST7
ST18	PEAR1	TENT5D	CCN5	FAXC	PCDH15	PODNL1	CCN5	SPATA9	SH2D2A	PKD1L2	ATG9B
OLFML2B	LTA	PGR	FOLR1	IL23A	SNORA23	LBX2	AKAP3	PLCH1	DPT	ASXL3	HK3
B3GALT2	C17orf64	OMD	GRM6	ATG9B	DNAJB7	COLGALT2	LRFN5	TRAF1	TUBB4A	SEMA4F	PLA2G4D
CRHR1	GDAP1L1	CCT8L2	SOWAHD	SOX11	TSPYL5	PODXL	IL19	ZIC3	GRIK2	CLIC6	COL14A1
ZC3H12B	LHFPL4	NTNG1	SLC16A5	RNU6-58P	RSAD2	GIMAP4	FABP2	JSRP1	S100A8	TMPRSS6	CFAP44
GPM6B	SEZ6L	SLC27A2	GLDN	KRTAP15-1	HEY2	THSD7A	PTCHD3	GAD2	CHSY3	PTPRB	SLAMF8
SYNC	TEX101	CCRL2	GPR1	CHRM5	MAPK8IP2	SLAIN1	OR6B1	KCNG2	APOA2	RTL9	MC5R
CSRNP3	KLK14	CCN3	PROKR2	CFAP52	THEMIS	MMEL1	RNU6-1122P	GPR179	CORO6	COL9A2	PLEK
WDR86	GCA	SLC17A8	PLPPR4	C4orf54	GPR22	CADM2	KCNK3	SEMA5B	STC2	ADGRB1	GPR171
TDRKH	NLGN3	VGF	NT5C1A	CMA1	ADAP2	DMC1	MYH11	CACNG3	ENO4	ACCSL	ADGRF3
EFCAB13	ADCY2	GPR4	ADCY8	GPR75	AK9	POMC	FGB	CNTN3	MAL	FAM131B	SLC28A1

NKAIN3	TRPM5	DDX25	CTNNA2	PRSS35	C1QC	IL2	IKZF3	HTR2C	TRIM22	MAB21L1	FBXO39
INSM1	SEC14L5	DMRT2	CCR7	LIPN	STK32C	TMEM217	AC008736.1	NRK	HKDC1	SLC51A	TTR
EMID1	S1PR1	EFCAB12	NEUROD1	MME	PRDM13	PAX2	CCR2	MEIG1	LMLN2	DPEP1	NID2
CAPN11	ACRV1	JAM3	C1orf100	TRIM17	AQP5	VSX2	F2RL2	NID2	CCDC151	SLC36A2	GIMAP8
SAMD15	HAPLN4	SUCNR1	EFR3B	CACNA1E	CYP8B1	KLHL41	RNU6-1304P	TTC21A	HUS1B	SLITRK5	ETV1
RCN3	SCG5	FBLN5	ARL13A	PDIA2	DMRTA2	SOBP	IYD	CNGB1	SNORA11	TRIM63	SCN11A
NXPE3	ACVR1C	CRB2	APBA2	GPAT2	PRR29	SOD3	BICD1	USH2A	IKZF1	ITIH1	FCRLA
BCAS1	EPHA5	UPK3B	CD86	NHSL2	CNGA4	TECTA	VGF	GGN	DOK2	KLK14	DMRTA1
NXPE4	ITGBL1	RCN3	TSPAN10	ATP13A4	HAND1	Z98752.3	BAIAP3	NAALAD2	TTBK1	CD36	DOK7
POPDC2	NEGR1	UCP3	CTSS	C17orf99	HORMAD2	KIAA1755	POU1F1	NFATC4	ASB14	BARHL1	KCNF1
FAIM2	NID2	P2RY14	TDO2	SYN1	FABP1	SEMA6B	UNC5D	GRIN3A	VIL1	PLLP	EMX2
BHLHE22	MMP27	NCF1	KCNAB1	SYT5	TMEM71	BDNF	PNPLA5	REEP2	NGB	LRG1	OPRL1
PSD2	DNAH9	TBXAS1	KCNT2	TNNI3	RUNX1T1	KRT73	CYP2F1	SCUBE3	HEY2	TNNT3	ZKSCAN2
IL18RAP	ILDR2	GUCY2C	RF00019	TRPV2	KCNE2	TRIM46	ATP13A5	KLHL13	HSD11B2	DNAH1	C9orf152
MLIP	C1QC	TP53TG5	EFCAB13	ZNF423	GRIA2	MECOM	P2RY10	GPR85	KCNMB4	OASL	PROCR
WEE2	ADAD1	KRT72	EFCAB9	GRIK2	PFN4	WSCD2	NAALAD2	CHST13	GGT7	COL15A1	CSMD1
BDH2	LMLN2	PDE1A	TNMD	MYO15A	ADGB	GUCY1A2	RNU4-89P	ANKRD34B	GNG8	DISC1	LRRC27
TNFRSF13C	PDPN	MELTF	NCAN	PRUNE2	SLC45A2	NCF4	SERPIND1	PLEKHG1	ADIG	HAND1	S100G
ZFP92	SNORA23	OLR1	A2M	ACKR2	METTL21C	SNORD15A	PLK5	ADAMTS5	C1QTNF7	ILDR2	SMYD1
LIX1	SCARNA1	ECEL1	PMIS2	DOCK10	SLC7A14	S100Z	SAMD15	AK5	LY6G6D	FLI1	SSMEM1
BIK	FGA	FGFR4	RF00153	FAM222A	C1orf158	ILDR2	S100A8	CCDC105	HIF3A	SLC22A3	MYOG
PPP2R2B	APOB	TRPV1	DCHS2	CRHR2	ESRRB	SPO11	PLD5	HOXD8	KMO	ANO4	C3
STPG2	TSPAN1	RTL9	GNRHR	PHOX2B	C1QTNF3	DPEP1	POU5F2	C9	ARL13A	NR5A2	PVALB
HPCA	LGALS2	GNG11	RIBC2	CCL17	SLC41A2	MIR26A1	SEC14L5	SCARNA22	PCDHB6	POU1F1	TMEM271
LRRN3	FLI1	INSYN2B	CER1	PGBD5	ZFHX4	CLDN5	HFM1	FNDC8	DYNLRB2	TRAPPC3L	PRF1
IL17C	MMP24	SOX18	RGS8	GASK1A	SLAIN1	SELENOV	ABCD2	SPARCL1	HIST1H4E	MSI1	CLMP
TESPA1	SGCE	ABCA8	SLC45A2	STRA6	TSSK2	SIM1	STAT4	MYH3	MAPK8IP2	ZNF784	RGL3
C11orf96	PALM2	SLC22A3	SPOCK1	LRRC10B	NRXN3	WDR93	PRDM6	ADAM23	HTR1B	APOA1	RAB26
SYTL5	STARD6	FCER2	DDI1	LHFPL4	TAT	LHFPL4	IL9R	PLA2G5	GALNT17	C21orf62	SYNPR
LRRC36	FAM107A	FAM228A	ZBP1	LTB	CFAP221	ADAMTS3	AVPR1B	GRIN2A	SNORD59A	FRMPD4	STARD8
GPR37L1	FEZF2	RNU6-431P	AC021072.1	TNFSF18	AKR1D1	KMO	BTK	PAX2	CNTF	PKD2L1	ISL2
DCLK2	B3GNT5	INPP5J	SPRR4	NPW	BTBD16	TRPC7	ISX	RGS17	CALHM6	DGKB	LRP11

FREM1	CCN5	CHRNB4	SNORD73A	TENM3	OR4K5	NTNG1	NLRP3	LRRC6	CCL22	NEFL	ISLR2
GRIA3	LMO3	PID1	TRPV2	GPR162	GPR88	RNF182	RF00091	BHLHE22	HIST1H2BM	STRIP2	CTHRC1
TNF	ABCC9	CSRNP3	CD53	CLCA1	LRCOL1	SOX18	CFAP44	DCX	INA	CDH5	WDR86
ZSWIM5	TRPC6	ZNF697	MYH7B	SLC13A4	FSIP2	MYT1	SPATA17	GPR83	STYK1	ASZ1	LOXL1
LRIT1	PDGFD	DGKI	PGF	CCDC65	DSCAM	CXXC4	AQP5	APOA4	CPNE1	PCDHGA3	ERP27
CIB3	CYP11A1	SEZ6L	HOXD13	ATP7B	RRH	CCM2L	HES2	ACRV1	NLGN3	PAPPA	PTPN7
B3GALT1	NEUROD1	CYYR1	PRDM6	CXCL11	KCNS2	CEL	FILIP1	ADGRB3	SUCNR1	F5	SYN2
FCMR	IGSF21	TEK	GIMAP4	P2RX2	GUCY1A2	TSSK2	COL11A1	SLC26A7	PANX3	HS3ST5	SPATA17
CNR2	KCNA10	RNF223	GFI1	LYVE1	TRIM66	CCDC105	DDX3Y	CRX	ACVR1C	TSGA10IP	PHOX2A
FLT4	SEC14L3	CRMP1	GPR37L1	TTLL9	CAPN8	SEMA5B	CORO2B	GJA8	FGF22	RAD51AP2	KCNC1
ADAMTS15	JAKMIP1	KIAA1549L	GLRA2	SOWAHB	MMP12	GPR179	NOBOX	OTUD6A	CD48	FGD5	FRMPD3
TNNT1	SNORA54	SHE	LRRC6	PCSK2	SRRM5	NPB	SLC7A10	GPR174	MYOZ3	TRPM6	SLITRK3
KCNJ9	GATM	TOX	CALCA	OOEP	PRRT1	KCNK1	FAM71D	GRIA1	FOXC2	ADAMTSL1	XIRP1
SCRG1	ITIH2	COL4A3	RNU4-58P	SMPX	NTSR1	GFI1	SNORA5C	SORCS1	ZHX1	ERC2	PIWIL1
CTXND1	MYT1L	TRIM66	GRM3	RASEF	NSUN7	USH2A	ANKRD34B	MAPK4	MIRLET7G	ADAMTS5	NAALAD2
CHAT	CALN1	MYO1A	RBPJL	OMG	OR8D4	KIAA1614	MOGAT1	IQUB	MASP1	PABPC4L	RRAGD
CD160	LMX1B	ENTPD1	ELANE	TTBK1	B3GALT5	USHBP1	PDE9A	MYH15	FRMD5	ZNF423	CFD
INPP5J	CFAP74	KCNQ5	NOS2	SCIMP	OXT	NFATC4	PLIN1	CFAP44	DLL3	ADGRL4	TNFSF15
CCK	IQCA1	LRRTM2	GRIA4	DNAJC22	ALB	INSM2	SLIT2	SCN1A	DUSP2	LGI4	CPB2
PDE3B	RPRML	LHX6	WAS	GDF9	NXPE4	GIMAP1	FZD9	MOGAT1	GUCY2C	ADCY8	DUOXA2
SNORD73A	C9orf131	RGS22	RASGRP2	PLA2G4D	SEMA3A	CADM3	UGT8	ADCY2	PRELID3A	MAK	ERICH4
OR10V1	DOCK2	C12orf71	PLPPR5	LMO2	TUBAL3	RTL5	SOX10	NOVA1	ZNF541	KIF26A	AFM
ACTL9	GRIA1	PDE3A	CD226	SEZ6L	BATF2	REEP2	TYRP1	SYTL5	CKM	USHBP1	TSPAN18
SNORA58B	LRRN2	LYPD4	TMEM63C	RASGRP1	TAL2	LHX9	SLC6A11	LRRC36	CALCA	PCSK9	APOB
CACNA1F	ASB17	CCNB1IP1	LRFN5	DPYSL5	ATP13A5	KSR2	SPEF2	CD300LG	TRIM69	TEK	AVPR1B
CYBRD1	BRSK2	LRRC55	GRIFIN	CD96	STYK1	MYBPC2	MUC3A	ABCC8	CCDC68	FNDC8	SH2D2A
ENPP2	ANKDD1B	TMEM200A	OR13J1	SLC17A8	PCDHGA2	GCKR	HEMGN	MIR99B	MOAP1	PRRT1	BMP5
SPN	PLIN5	TMEM179	HS6ST3	CD80	SNORD73A	GIMAP6	IQCH	WNT1	COLEC12	CEMIP	RNU6-376P
LUM	C4BPA	RFLNA	KCNG1	HSD11B2	KLK12	AK5	ATP8B4	RADIL	MCMDC2	CRYM	TUBB4A
DACH2	ANGPTL3	NEK11	CCDC151	SCTR	ACTC1	SLC1A2	ZPBP	POPDC2	ZFP92	ACTL6B	SYT6
PRM2	ABCB4	KCNV1	SLC24A1	PCDHGC5	CNKSR2	KCNH6	NUP62CL	SHANK2	CXCR6	SYT16	GDPD1
CYS1	DNAH6	SPINK14	CHRNA3	TEX38	MMP25	C1orf115	CCDC30	CCN6	KIRREL2	MAMDC2	GRIK2

ENKUR	CNDP1	DOCK2	KLHDC9	GPR182	RNF125	OLFML3	ARFGEF3	FBXO41	FCER2	NECAB1	SMARCA1
SLAIN1	MIR148B	CLHC1	GAD1	PKIB	MYO1F	SCARNA22	MMP16	RNF207	ADGB	TMOD1	VIPR2
TFR2	CTSE	AC020613.1	HECW1	NRXN1	CACNA2D3	TACR1	SYNGR3	TMEM255A	TSPAN1	FIBCD1	TMPRSS9
FOXS1	FGG	TMEM82	MYT1L	KCNN2	BFSP2	NAP1L5	OR2I1P	IL31RA	CHRNB4	FMN2	CCNB1IP1
TACR3	SYNGR3	MEOX1	PCDHA10	GABBR2	SLC7A3	APLNR	AL353572.3	FGD5	STPG2	FPR1	EFCAB13
DISC1	CCDC89	SMIM18	STARD6	SLC11A1	EBF4	MIR339	LRRC10	PPM1J	TNFSF4	SOX1	CNTN4
SLC5A5	ATP2B2	AC007906.2	SLC9A3	TNFAIP8L2	TRIM63	PTGIS	GRXCR2	GDF10	RRH	GABRR2	SCN1A
ACTC1	TMEM262	TNFSF13	HKDC1	C12orf56	CSMD3	FNDC8	NAP1L2	HTR2A	FAXDC2	GABRA2	SCIMP
TEX35	GABRR2	COL6A6	LYPD2	CPNE1	ST8SIA2	SPARCL1	GBGT1	AC055839.2	MPP4	CYP19A1	GRIA1
LSMEM1	PSPN	VWF	WFDC1	MIR365A	PRKG1	ATP2A3	FGL1	GPR173	CX3CR1	C1QL1	CYB5R2
GPR156	PAX6	ATF7IP2	MRPL53	CLDN20	FATE1	ST8SIA4	ALDH8A1	BMP6	KRTAP16-1	MYBPC3	SLIT2
CLIC6	NTNG1	ADAMTS3	AC010616.1	RNF182	MFAP5	MYH7B	GRIK3	NUGGC	SLAMF7	SMIM22	SLC9A3
ASGR1	ZMAT4	EGFLAM	AIRE	GRIK3	OOSP2	EYA1	MOV10L1	PAQR9	DUSP26	HMCN1	SHANK2
TXK	UBXN10	LTBP2	SCN4A	FOXC2	MIR32	THEGL	TOPAZ1	CRISPLD1	MMP12	FAP	ENO4
KDM5D	CELA1	C4orf45	FAM163B	RBM44	CEACAM20	UPK3B	SERPINB13	NCALD	SLC28A3	SERPINA9	HOXD11
LMX1A	SCRT2	PGBD5	CD4	SASH3	SIAH3	C20orf96	SMIM38	OR52N1	NEUROD1	SLC25A21	SSPO
VIPR2	PDIA2	KCNMB4	UCHL1	IQCM	ATP6V0D2	RIMS2	MPP3	GBX1	SNORA54	MIR26A1	ST18
KCNK10	DYNLRB2	RNASE10	RLN3	MIRLET7G	AP3B2	CAP2	AXDND1	RNF150	IL1RL1	CCN3	SMIM41
ANKRD34B	TRPC5	SFRP5	VWC2L	TMEM121B	NEUROG3	LANCL3	GRK1	PTPRB	PLD6	FOLR2	TRIM22
SLC27A5	TPO	TWIST1	NAGS	GLYAT	ONECUT2	LRG1	HTR2B	GCHFR	TOMM20L	CLIP3	PAX3
SNORD38B	AMPH	PTPRB	P4HA3	RNU6-1095P	RPL36AL	TRIM67	FGA	INSYN2B	PTPRO	L3MBTL4	COCH
CNTF	DKK2	LNP1	ZNF35	MASP1	PCDHGA4	MYH3	DPF1	RF02176	C4orf51	PITX1	TNFRSF13C
ZNF385B	ADCYAP1R1	LRRC36	NRSN2	FRMD5	CRNN	RNU6-58P	ZNF641	S1PR1	TRIM66	ZFP37	PCDH9
GPR151	DPEP3	ADAMTS4	PCDHAC2	ADAMTS12	ADCY5	CFAP52	C3AR1	CYP1A1	TRIM9	C2CD4C	LMX1A
C20orf96	NKX6-1	RAB39B	TSPAN1	P2RY4	LRRN4CL	C7	FBXO43	CDK18	GLRA4	SEMA6B	MFAP4
KCNN4	FXYD1	SRMS	S100Z	DLL3	MAPK15	ELN	SLC30A10	ZMAT4	PDE3A	SPACA1	TACR3
EBF1	ALX1	TMEM178A	EDNRB	MANSC4	TNFSF13B	PRSS35	ZFYVE28	ARHGAP28	RNU6-102P	ZNF521	ANKDD1B
RSPO3	PAK5	GXYLT2	PCSK2	PGR	LRRC10	ESAM	MRGPRD	ADGRD1	LHFPL2	FBXO27	LMLN2
TRIM17	MRAP	UPK2	HLX	BICD1	DIO3	ADGRB3	BSX	ANGPTL1	GFI1	ACTA1	RPE65
LRRIQ3	MAEL	GCK	PTPN22	CD83	TMEM82	ANGPT2	CFAP221	MC5R	EMID1	LEPR	GRIA4
SUN3	KLHL14	GPR82	CA5A	MCMDC2	FXYD1	ADCY2	SYNPR	CDH8	PADI3	EPHA5	SNORA11
HSD11B2	HRK	BOLL	GDF7	CXCR6	LEPR	ARL13A	LKAAEAR1	GNAT2	ADCYAP1	ELN	VEGFC

AGXT	TTC6	TIE1	PTPRC	SLC35D3	NR5A1	CD300LG	ZNF536	FRMD7	SNAP25	TRPV5	CCN4
ZMYND10	HUS1B	PLIN5	GPR141	CARD11	BIRC7	ABCC8	LRMDA	RF00432	COMP	TIMP4	TMPRSS15
PTPN5	HS3ST4	ITGA9	SNORD117	FBXO41	MUC13	MIR99B	ODF3	FMO2	C20orf204	GRPR	F13B
SCARNA22	TRIM50	IL9R	SLC24A5	ZFP37	STPG4	MYCT1	LRGUK	AC022167.5	GREM2	PTPRT	SOHLH2
ALPK3	VASH2	DHH	KRT23	MEIOB	TAL1	SEBOX	COL6A5	CCDC106	KLHDC7B	ASTN2	HPCAL4
SSTR2	LOXHD1	SOX8	CIITA	C1orf115	ODAM	WNT1	DGKB	ICA1L	RBFOX1	ADRA1A	CHRNA2
LIMS2	MMP23B	IQCH	SIX4	RADIL	RASGEF1C	RADIL	INSRR	RBM44	TMPRSS11E	LRRC4	WNT1
RCAN2	TNFRSF9	GPR18	SCN10A	DNAH9	DPYSL4	SHANK2	P2RY12	CNR2	SERPINC1	SLC10A4	GDF10
KCNB1	STAB2	BMX	WDR17	PDE6B	CPLX3	SLC41A2	JCHAIN	GRIK4	LRRC23	MRPL53	GPR37L1
F2RL2	MKX	HOXD3	DRC1	FCMR	PPEF1	C20orf144	CLEC7A	OMD	CLDN10	PCDHGC5	MIP
GFPT2	KLHL4	ASGR1	TRIM71	UCMA	ITGAD	KDR	MUC13	GPR15	SLC27A5	CA8	DISP3
HHATL	CXCR2	PARVB	TULP1	KRTAP16-1	SP5	FUT9	TACR2	MS4A7	ERFE	CCDC65	RHPN1
PJVK	SNORA84	MDH1B	LRRN1	IL17B	SPAG4	KRT72	SRPX2	TMEM249	ENKUR	FGL2	CDH9
ALPK2	TRPV2	TSPAN11	CCDC85A	FGF7	LOXL1	RNASE6	LRFN2	TAGLN3	OTX1	MPO	GJC2
CERKL	RRH	CHST4	RNASE6	FST	C2orf92	SLC8A2	RNU6-799P	ENPP2	BCHE	RTL5	IL20
ZGLP1	TMPRSS11F	CLDND2	PRRX2	ANK1	HTRA3	CREB3L3	DRD3	CDH12	SOX5	GRM8	MAP7D2
EFCAB9	SCAMP4	NPAS4	HSD17B1	CPSF4L	CORO6	TMEM255A	NOX3	LRRC4C	FUT7	SLC47A1	RASEF
TLR6	PDE1B	B3GNT10	NHLRC4	CHST13	CADM2	GDF10	POU4F3	VSX2	TSPAN10	KLHL33	FREM1
DMRTC2	TRIM15	GP1BB	SLC27A5	GRAMD1B	CYBB	PTPRO	BARHL2	FMN2	GATA1	SLC1A2	GGT7
ALLC	KRTAP26-1	MASP1	LSAMP	ACOT11	KDR	KCND3	TLR7	SCRT2	TDO2	MEOX1	ECEL1
RHAG	TMEM71	PTPRO	MMP24	SRMS	ZAN	NUGGC	OR11H6	GCGR	PPARG	MECOM	ADIG
CA5A	CCDC102A	XCR1	SEMA3G	PGLYRP2	ST6GALNAC5	TMEM178A	SIM2	TRPC3	CD93	TH	LY6G6D
SPP2	CPQ	TRPM3	TOMM6	PRR18	SPNS3	CHP2	ANKUB1	CNTN6	SAMD15	TMEM229A	KMO
PTGFR	SEMA3A	PDK4	CCR2	OTOGL	SCARNA22	SPINK4	GABRA1	SERPINI2	PNPLA5	PCDH15	ARL13A
TMEM156	OIT3	SHISA3	SMIM35	CHRM3	ZP1	DSCAML1	SLITRK4	B3GALT1	ALOX15	LRRN1	STMN3
FXYD2	GPR85	MIR628	CXCR2	CHIC1	IL7R	STMN2	HECW1	DNER	KCNAB1	BMX	NPPC
FYB1	SLAMF9	PAX7	LTF	RNF222	4-Sep	RADX	ZNF697	TRHR	TWIST1	PSMA8	ANK2
SNAI1	TMEM95	PDLIM3	KRT20	GJB1	ARR3	EGR4	SCTR	HRH3	HECW2	SHISA3	CHRDL1
KRT34	ACKR1	CA8	SCG5	STK32A	CLDND2	PHACTR1	SLC6A16	MIR154	ATP6V0D2	CRISP2	RNU6-799P
MGAT4C	CSMD3	GREM1	DYNLRB2	ACTL9	TTC6	HIST1H1A	KCNJ8	SLITRK1	CD101	LRRC34	KRTAP7-1
NT5C1B	STMN4	LMO2	NKX6-1	DISP2	POU2F2	NCMAP	ITIH1	SLC8A3	LRRC52	RNF182	PSORS1C2
MASP2	LRP1B	CD300LG	MYOZ1	COL26A1	SDS	ZNF423	SMCO3	TEX51	CTSE	HEPACAM	SNORD59A

LY6H	MIR26A1	PRR19	SRPX2	SERPINA2	IL20	GBX1	RNU6-351P	DMGDH	PRKCG	C9	MYBPH
TMEM114	SPOCK1	CCDC30	SAP25	PITX3	LRCH2	LAIR1	SCARNA3	CSF2	SYNGR3	KCNE4	C8A
TMEM52	HSBP1L1	HCAR1	ASB10	BPIFB1	SNORD42B	SLC27A2	RIMKLA	KCNJ8	LRRC10B	C13orf46	TAS1R2
SPDEF	GPR15	PNMA8C	SH3GL3	EDN3	PAX3	SNPH	RNF186	MYH8	GPR82	FATE1	CPNE9
SIT1	NRXN3	GNG2	FOXA2	GUCY2F	C17orf98	INSYN2B	TMCO2	CNGA3	ATP13A4	SH2D6	LIMS2
TAS1R2	SGIP1	SERPIND1	DAO	ST8SIA3	C1QL3	SHOC1	SP6	CACNA1H	PSPN	NXPE4	IQSEC3
TRPM8	ST8SIA2	PPP1R16B	C14orf180	TMEM211	TNFSF8	HSD11B1	DLGAP3	GRM5	CD79A	SNORA62	COL28A1
RIMKLB	CTNNA2	CCK	SAMD7	FAM43B	LTC4S	PRUNE2	LRRC26	PRRX1	SYT13	RNY3	SGCA
PNMA3	SRRM5	FMO2	LRRC43	SNORD127	CYP21A2	KCNH4	PTPN18	KLHL31	SNORD87	KLKB1	HIST1H2BM
SFMBT2	CFD	SLC5A11	SNORA2B	TNP2	ANKS1B	DPP6	GSG1L	KCNA2	IFNK	PRRX2	CAMP
XKR9	HYAL4	ITPRID1	SLC22A14	CAMP	PKP2	TIE1	IQCD	RIMS2	GAREM2	HOXB1	ELOVL3
MYOZ1	FRMPD4	IL7R	C5AR2	MOGAT1	GJC2	GIMAP7	ABCA9	KCNH1	TRPM2	TMEM156	PANX3
PCDHA10	SLITRK3	PCDHGA2	RNU6-871P	SEC14L5	CSMD2	MYH7	OBSCN	ADCY8	CAMK2A	ICAM2	PLA2G2E
CNGA4	XIRP2	QRFP	OVOL3	CERKL	SNORD63B	ACTL9	KCNN2	RBM24	SNORD38B	ABCC2	SLC12A1
CAMP	OSR2	LRG1	GPR50	SSMEM1	KCNQ3	RHO	GPR75	SPRED3	SLC9A4	LMOD2	NPPB
ADGB	GRIK2	PIK3AP1	CHN1	CRHR1	PDGFRL	C9orf43	LYVE1	C5orf49	FRRS1L	DYSF	PLPPR5
RF02132	DNER	SORBS2	PHYHIPL	F2RL2	SYT14	ZMAT4	CKM	KRT18	GAPT	TMEM178A	ALKAL2
ERG	LHX6	MIR99B	HRH1	MAGEE2	C9orf131	PIK3R5	FMNL1	FAM205C	VTCN1	RF01684	TBX5
FAM237B	JCHAIN	SMYD1	PTGER1	PHEX	GRIA1	TIGD4	RBM44	SORCS3	APOD	KIF26B	SCGN
NLRC4	MMP25	PPP1R1B	ITIH3	SMIM38	EFCAB13	CAMK4	LRRN4CL	UROC1	SUN3	S100A8	GNB3
MYO1F	ALDH1A2	PRM2	FAM205C	ADAMTSL3	PNMA8C	TUBB4A	SNX32	WDFY4	ZNF575	CHSY3	OTC
ADAMTS3	HKDC1	TTBK1	RAB39A	ACOT12	MYT1L	AC020613.1	ATP2B2	TP53TG5	SLC9B1	STK33	NEUROD2
FIBIN	HMX1	SNAI1	MPO	F2RL3	SCN3B	BCHE	EPHA10	GFRA3	MIR628	APOA2	SCN2A
P2RY13	SHH	SLC16A12	KCNJ9	PLA2G3	MROH5	KLB	PLA2G5	NACAD	CCDC69	THRSP	SIT1
SLC5A11	ATP1A4	ALDH1A2	C5orf52	EYA2	KRT20	MC5R	HIST1H2AE	HIST2H4A	C2orf72	EFHD1	CRNN
PRKCG	NR2E1	GREM2	TFR2	ZC3H12D	TMEM210	ZNF853	ARMC12	GRIA2	C2orf73	TSSK3	GPM6A
TRIM71	HTR7	GTF2A1L	FBXO41	GRIN3A	DCDC2C	FMO2	RAB42	STRA6	ANKRD34A	SLAIN1	ZDHHC22
SYT5	TKTL2	SLC2A10	MEIG1	ASPHD1	TLX1	AC022167.5	PDE10A	SLC43A3	TMEM37	ATOH8	RFLNA
CCDC148	CACNA1S	SLC5A2	HECW2	TARM1	HIST1H1T	GNG4	SIAH3	TMPRSS11A	SSTR3	EGFLAM	GPR22
SUSD3	SYT6	TRAM1L1	UBD	DEUP1	KCNK9	CLCN1	CHRNA5	NLGN1	C14orf132	HSBP1L1	DCLK2
SNORD121B	SLC7A9	TXNDC2	KCNG2	RNU6-638P	LKAAEAR1	ERBB4	CFAP97D1	DMTN	ZNF449	ST6GALNAC4	AVPR2
GPER1	CNTNAP4	ANKRD63	SLC19A3	FHAD1	KLF17	RF00026	PLEKHG4	KCTD16	SVIP	HKDC1	ABCC9
SEMA4F	TRPA1	NPPB	C2orf74	RHPN1	SFTA2	ZNF831	RPS12	BFSP2	KCNG1	SSTR1	NPPA

SYNDIG1L	RTP1	ABCG5	ADAP2	ZFP82	ATP6V1FNB	CLEC1A	C8orf74	NXPH1	HPX	KCNE2	RAG1
EPS8L3	ANKAR	GJC2	DSCAM	PRELID3A	GPRC5A	AGTR2	TMEM169	PTGER2	ELOVL2	RGS14	PRELID3A
SCN3B	BAAT	CABP7	NMU	CHAD	LRGUK	OMD	TDRP	NOX4	SEC14L5	HUS1B	ZNF541
CIDEC	PPP1R3A	NDP	ARHGAP36	CASR	FAP	KCNN4	TRPV5	P2RY4	DNAH5	SLC19A3	LDB3
FAM229A	OR4C5	ANGPTL3	CSF3	CD101	ARFGEF3	MAP6D1	TTBK1	CITED1	PTGFR	DMC1	RIMS2
CD34	MAB21L2	KCNE5	PCDH8	APOBEC1	PLP1	TMEM26	EPHA7	HVCN1	CAPN9	SOX18	FAM20A
CALCB	SYNDIG1	EPS8L3	CALY	TSPAN10	KCNG4	SLC6A3	SNORD63B	NRXN1	ARMH1	FAM222A	TRIM69
SLC9A7	PCP4	SSMEM1	C11orf53	CFAP100	SPACA4	DNAI2	RGS5	SMIM38	FYB1	PCSK5	TIFAB
RARRES2	PHF21B	LEPR	SIDT1	PRKCG	CHRD	LYL1	DZANK1	POU3F2	GLIPR2	RNU6-200P	MOAP1
ADAP2	HGF	PDGFRB	NECAB2	HSD17B1	ERG	TREH	PROM1	CES5A	CCDC169	WDR72	ABCC8
SHE	COL9A2	TSHB	ABCA9	RAI2	ZBTB46	AKAP6	ATG9B	MOS	HMX1	FMO4	COLEC12
RBM42	ASCL3	NTN5	SHROOM1	MTUS2	ALS2CR12	SH3BGR	CCR7	ANKDD1B	SNORD18A	PCDH10	RANGRF
APLNR	C9orf24	KCNA3	ASIP	DPYSL3	APOB	HTR6	TRIM50	KCNE5	CERKL	UBTFL1	CACNA2D1
FABP7	DIO1	PLK5	CCDC83	PLA2G2E	PSORS1C2	EID2	C8B	CASS4	FAM78A	PREX2	PRDM6
SCARNA5	SPACA9	TNFRSF1B	CHRNB3	AFF2	RTN1	B3GALT1	TC2N	TMEM44	RNU105C	LRRC55	SORCS1
GASK1A	GLIPR2	PTCH2	CDHR4	NFATC4	SLC36A2	HRH3	SCN11A	KCNT1	C1QL3	INSC	TMEM145
GLIPR1	RNF183	ACTA1	IL25	SRGN	PROM1	DMGDH	LTA	SIX4	ABCA9	HIF3A	DMGDH
INSYN2B	SCN2B	WDR93	SLC24A4	CNDP1	ANO4	GRM5	ODF3L1	CYTL1	C10orf99	DTX1	TMC1
ADCYAP1	ERC2	MIR708	NKX2-6	RTN4RL2	MIR339	MYH8	CRYGN	CCL7	HRH1	PCDHB6	OR13J1
LAMC3	SNX22	MROH5	WDR72	CD3E	TOMM6	ADCY8	GFI1B	RGS7BP	GPRC5A	NFATC4	LBX1
TMEM182	ZYG11A	AGXT2	ALKAL2	KLF14	VAX2	ATP7B	CLEC4E	PRKG1	SCARNA12	SCNN1B	KCNA4
GPR179	RNF207	CCDC60	RF00026	GPRC5B	MAT1A	CXCL11	SLC25A2	ALDOB	TRIM15	TACR1	C2orf16
ABCA8	PCDHB3	TC2N	MIR33A	DNAH10	C8A	FAM205C	RPL10L	LSAMP	SNORD71	CALHM6	NEUROD6
MMP12	SEMA7A	FTCD	OR51E1	MINAR2	INSM2	KIAA1549L	SKAP1	WDR93	KRT28	LRRC75B	DCSTAMP
INMT	TNFSF12	TENM1	TRIM40	SNRPN	CHRNA4	FRMPD3	CPA2	EMILIN2	ARFGEF3	MYOC	GBX2
CALB2	AKAP14	GCNT7	RNU6ATAC29P	MYRF	SAMSN1	ZNF366	PLCE1	SLC41A2	RNU6-1122P	POU2F2	PIWIL4
CR2	CKM	PRKD1	SNORD123	SNORD87	P2RY6	PGF	SPN	MYO15A	SHH	IL4	KCNJ4
TMEM132D	EPHA6	STC2	SNORD92	SEBOX	PKLR	NXNL1	TNFSF13B	ZNF618	EID3	INA	GPR6
ZNF483	RAB17	SGPP2	CLCA1	TSGA10IP	HNF4G	CCDC151	KCNT1	LMCD1	LCN2	SEMA5B	KCNV2
CORO2B	TMEM255B	AC022167.5	RHOH	GSG1	FMO3	GULP1	MYH15	OR10V1	SLURP1	MFRP	RTP2
MAPK10	CNGB1	LRAT	INSM2	TRIM46	RNU1-125P	GALNT12	B3GNT10	MMP13	GUCA1B	RNU6-243P	PLPPR1
LYG2	CLCN1	PAQR6	BARHL1	SMARCA1	RFLNA	PCDHB7	NR5A1	POU6F2	PDE1A	SLC22A2	RNU6-539P
ABAT	ECEL1	GPR21	TRPV5	FANK1	TACR3	CASR	ESRRG	SNORA58B	BATF	PRSS38	RNU6-10P

GAB3	GAD1	RBM42	PPP1R9A	MGAM	TTR	SAPCD1	HSH2D	CADM3	SGPP2	SYNC	PLEKHB1
PRKD1	RETN	PLA2G2E	NAP1L5	ALAS2	FOXF1	RASEF	SLC6A18	IL4I1	TLL1	PTPRQ	SHOC1
CHST11	DPF3	ABCC8	KRTAP8-1	SGCG	HGD	OMG	PLA1A	ZFHX4	CRB1	MLANA	FAT3
TSTD1	ZNF583	HELT	SCIMP	PAPPA	PPP1R16B	ZP1	FAM189A1	EID2	GMFG	FGF22	FBXL7
ZNF354B	IL7R	MORN3	SLC36A2	WNT9A	CD53	NGB	RESP18	RYR3	ZPBP2	GUCA2B	AK9
IQCD	SPAG8	FAM171B	EPHA10	NAALAD2	CNIH3	PTCH2	AKAP2	SLC9A3	TIMP1	ADRA2A	THEMIS
OMP	PLK5	GCNT1	ST8SIA1	ROPN1L	PTPRO	GDF9	SLC35F3	GPR55	FAM71B	KCNH7	GPR85
SYT9	BRINP3	MBOAT2	CACNG1	NRXN2	IGHM	SPATA46	MIR711	GUCA2B	NEK11	FSD2	MPP4
TMEM217	PREX2	MPPED2	MYO1F	FAM13A	ARMC3	CD19	ERP27	C1RL	SUSD3	SLC43A3	MYH3
CHRNA9	PRF1	LMAN1L	ZNF583	RFTN1	SOX17	HBZ	OPN5	PRELP	PLAUR	ZHX1	CX3CR1
LYPD2	F2RL3	ARG2	GYPC	APOBEC3H	SHISA7	GNG8	KLHL33	MYO1G	CFAP52	APOLD1	ZPLD1
ERICH4	GLRA4	RBFOX1	CA14	CACNA2D4	CNTF	GIMAP8	CXCR3	ARNT2	UNC5D	SLC38A4	SCN9A
NTS	C8orf74	MB	BFSP2	RNU6-494P	RNU6-1299P	ASXL3	G0S2	FAT3	IGSF11	CGREF1	C16orf45
ZSCAN10	SSPO	ZFP82	ATP6V0D2	CD27	HOXB1	IL18RAP	HCRTR2	DGKB	FAM166A	MT3	CAPZA1
BATF3	CSMD2	CD34	KLRD1	KCNC2	TMOD1	CLIP3	IL12RB1	GABRA2	OR6S1	NTRK3	TMIGD1
TKTL1	CYTIP	SHANK2	CRABP1	BTC	FLG2	GFPT2	AQP4	PAX9	STOX1	AEBP1	KCNQ3
NRL	KCNQ3	GPR85	PRF1	JAM2	ZPBP2	RNU6-384P	TBX19	SLC22A16	TM4SF19	CD4	RGS7BP
SPEM1	SPATA45	CRACR2A	ATP1B2	COMP	OR10V1	TEX38	LRP2	FGF12	ADAM32	CRTAM	TYRP1
PXT1	IL4I1	GPR22	PIK3R6	MCOLN3	KCNK13	SNORA23	FKBP6	PDE10A	CD244	SYT7	ANKS1B
PNOC	RNASE12	ST18	CPQ	CLGN	C16orf54	ADAP2	LHX6	CHRNG	SLC9A7	CKM	CPN1
USP29	SRSF12	C14orf132	DNAH3	ACVR1C	TMEM255A	PRDM13	PROKR2	ADRA1D	CFAP73	ALDH3B1	PLCE1
AURKC	RF00604	KCND3	BATF2	TLR6	SERPINA5	AK9	ANGPTL3	COL11A1	C1QB	CTNNA2	SCARNA1
RF00090	EID2	NXNL1	BTK	TMEM236	CCDC69	CCN3	ELAVL4	CHRNA9	SNORD117	CXCR2	CYP2F1
KRTAP27-1	MIR103A2	NEGR1	TRDC	BATF	REC8	CYP7B1	TRIM40	FGF5	IL17B	CACNG3	FLG
HOXB13	ACMSD	DKK2	PHEX	NPFFR2	GUCY2C	CCDC168	PDCL2	KCNJ5	SEZ6	SLC2A10	PCDHB1
RUNX1T1	ZNF536	MYL10	SERP2	CYB5R2	ILDR2	LEF1	S100G	SLC17A2	GLIPR1	CR2	RN7SKP56
C15orf48	ATP13A4	CFAP61	SYTL5	RSPO2	CXXC4	CHSY3	C9orf131	ADH4	MAPK10	PIPOX	IL1RL1
LRGUK	BARHL1	F5	RTN1	OR1M1	EPHA10	FUT4	RNF222	GLRA3	TEPP	ITIH4	AURKC
SEMA3G	NKX2-1	RBPMS2	GPR15	CSTL1	C21orf58	PEAR1	CLDN10	TAS2R16	SMC1B	CNMD	TOMM20L
FOXF1	USH1G	SEZ6	PTP4A1	FCRL1	MIR221	ST3GAL5	PAX6	PRLHR	PGLYRP1	ABCC12	PTCRA
SLA	PRDM13	TACR2	AK9	C17orf107	KCNB1	UBE2QL1	SKOR1	GJA10	LOXL2	KIRREL2	SLC8A2
TMEM26	GALNT17	CHGB	ABCB4	CER1	CEL	TMEM232	FSTL4	CA10	AMH	FAM167B	TSSK1B
BTK	TMEM82	IGSF23	TNFSF8	C3orf52	CACNG2	OR10V1	SLC13A3	CCDC192	MIR365A	SLC11A1	ASB5

FAM184A	DISP2	FAM166B	CNKSR2	HAS1	FNDC8	MFNG	DDX4	RPL10L	SLC5A1	CXXC4	LMO2
ARID3C	TNMD	NME9	ESRRB	C14orf132	MYPN	DDX25	CCDC33	LAYN	ADAM11	TNR	UCP3
RASSF2	FANK1	OTOP2	KRTAP15-1	RINL	GRID2	RNF144A	SLC12A8	LIN28B	OVOL3	ADAM28	NLGN1
PLEK	MEP1B	MAS1	PSCA	WASF1	MYCT1	KLK14	PCSK1	RF02209	TNFRSF8	RUNX1T1	PAX6
PCDHGA2	RPE65	SCARNA18	RNU1-43P	SPATA20	RIBC2	FSD2	SNORA55	FAM81B	TAL2	FAXDC2	HECW1
RGS4	IQSEC3	RF00019	C1QC	SPOCK1	STK32B	MIR26A2	ANKDD1B	ZPLD1	ODF3L1	NELL2	SIX3
SCN3A	NXNL2	DTHD1	SNORA54	SCAMP4	LIN28B	SLC9A3	ALPK2	PCDHB1	SHCBP1L	S1PR1	PTCHD4
CYP21A2	NR5A1	PATE3	XIRP2	ASPA	PTCHD4	GPR55	IL1RAPL1	CBLN2	SEMA7A	PPP1R3A	TTC9B
CLDN20	HTR1F	NSMCE3	OSR2	P2RY13	TMC1	WDR86	MIR133A1	KCNC2	EGR4	SOAT2	SEL1L3
TOX	TMEM210	C6orf201	SHH	SLC29A4	HS3ST5	GUCA2B	SLC1A7	P2RY12	SAMSN1	SLAMF7	FGB
ANKRD31	FAM71B	KIAA1614	CR2	PLD6	OTX2	SLC39A4	CCDC146	ITGA9	CDH17	C3orf67	CDHR3
NANP	CFAP61	TMPRSS11A	HLA-DRA	FGL2	MYL1	SAT2	BHMT2	TRPC5	CNTN5	PPP1R42	ADAMTS18
LTC4S	SRPX2	ST3GAL5	LMOD1	ACSM5	KCNJ6	ADGRB1	VGLL1	SSTR2	SCARNA3	TFPI2	HTR6
AJAP1	TSHR	RIMS1	CHRNA4	PTGER2	BRINP2	RCN3	TBXA2R	IL1RAPL2	GUCY2D	RNU6-895P	NAV3
GCNT1	CDX2	SCNN1B	C17orf107	SBK2	LIN7A	ACCSL	RF00622	GABRA1	CCKBR	PLD6	MISP3
CD300LG	C8orf34	DDX60	SAMSN1	DACH1	C14orf39	ETV2	L1TD1	GRIK1	PLA2G2D	CLHC1	RBM46
SLC6A16	PTCHD4	ATP2A3	OTX2	LRRD1	HCN1	DLL3	SNORD17	ST8SIA2	IQCD	PTPRO	DBN1
SNORA62	SHOX2	TTLL6	ODF3	BCAS1	GRK1	DUSP2	EFR3B	GIMAP1	CCDC170	CLEC14A	PADI3
IL18R1	SLC4A1	KNDC1	LMOD3	GPR4	CHRNA5	STK32B	ABCG8	SEMA4F	RS1	GPER1	C11orf87
MMP11	ZC2HC1B	PATL2	ACOD1	PRR5L	ZIC4	MIR302D	SDR9C7	HDAC9	TBX21	VWF	SNAP25
CD163	KLHL1	KCNA6	SHISA9	GJC3	ABRA	MANSC4	BTBD18	ST18	OSCAR	C4orf51	FGF6
S100G	FGF8	CCDC170	C6orf118	C12orf71	OR52L1	PAX9	TRANK1	CLCN1	HCK	SPACA3	VSIG10L2
LNP1	TAC3	TMEM119	RIMBP2	FSCN3	EDDM13	GLRA3	GPR17	GUCY1A2	VWA5B2	CA14	C20orf204
CFAP46	CHRND	PIP	LHX5	ARHGEF38	ADGRG5	SLC51A	STK32C	KCNN3	LEF1	SPRY4	RF00432
RASAL3	SLC4A10	ODF1	F9	TRPC5OS	RNU6-271P	GRIK1	DENND3	C16orf86	REP15	ITGB1BP2	SPO11
ATP8B3	CLSTN2	MEI1	ANXA10	10-Mar	SRD5A2	ELF5	GAREM2	CNTN4	STAC	KIF1A	FRMD3
PDE7B	HDX	RN7SKP122	UGT2A3	ARHGAP20	GPR25	ELFN1	MAMDC2	BOLL	PLPP4	GLRA4	RBFOX1
PYY	GSX2	C10orf105	DCDC2	KCP	SCUBE1	RAB39A	ADAMTSL2	MEGF10	POU5F2	1-Mar	TMPRSS11E
SLC25A18	HLA-DRA	STPG3	BHLHE23	BMPR1B	ENPP4	NDNF	SEMA6D	LRGUK	NYX	SEMA3A	PODNL1
TCERG1L	AVP	KCNQ2	ONECUT3	DNAH11	P2RY10	SLC12A1	AANAT	NDNF	TMEM121	ACSM3	SERPINC1
CPNE7	IQCA1L	SLC34A3	RNU2-35P	SUSD2	LINGO4	HAND1	ACOX2	C9orf131	ERN2	RNU6-102P	SHC3
CHST10	ELFN2	TMC3	NKAIN2	NEIL2	KLHL41	SPINK8	GUCY2C	ZNF423	AL162596.1	SULF1	TESPA1

GXYLT2	SPTSSB	TBX21	TRBV28	HCN4	FAM13C	SLC36A2	ASB18	CSDC2	PLA2G3	LHFPL2	CDHR1
DPP6	OR56A4	HSD11B1	RNU6-750P	PGF	SCARF1	GCSAM	CYBA	GPR75	LAIR1	GFI1	CBLN2
ST8SIA4	TMEM174	NKG7	RF00402	TLE2	LEP	NXPE4	NELL2	BHLHA15	RNU6-1299P	EMID1	DNAH6
RNU4-89P	FAM19A1	CTHRC1	CDK5R2	CAPN6	CREG2	COL15A1	CCDC60	MINAR1	HIST1H1A	RNF207	ABCD2
ADGRG7	CEND1	SEMA3A	RERGL	DNM3	KRT4	MLIP	ACP7	PTGDR2	RELT	IL36B	RF00026
DZANK1	MIR200B	TSSK2	RNU6-1124P	RF02132	HAPLN4	ZFP92	APOBR	GPR156	LIN7A	FFAR2	PAPPA2
C1QA	PSMB11	IL31RA	MIR200A	LAMA1	IGF2BP1	MYH1	LENEP	BRINP1	ABRA	QRFP	RBP4
TTC21A	OR5AR1	TRAT1	HOXD1	CDH9	ERFE	CARD11	PCDHA10	MIR339	NANP	TNNC2	MCOLN3
CCN6	RNU6-782P	RGS4	SRSF12	LTBP2	SLC6A19	RUNX1T1	GRM8	TMEM262	SNORD11B	UNC5C	BCHE
TUBAL3	CFAP99	SFRP2	HIST1H4E	HSD17B13	GRP	KCNE2	PRSS27	TRPM5	TNFSF9	HYDIN	TMEM117
RAB26	PLPPR4	CPNE7	ACTN3	MINAR1	DDAH1	TMEM236	KCNAB1	ATP7B	LRMP	MED12L	PSTPIP1
F13A1	NMU	HECTD2	ARFGEF3	CFAP46	PCDHGA3	TSPAN1	OR12D3	CCBE1	NOX1	SLC27A5	PRODH2
B4GALT5	STRC	OTOS	SERPINC1	CCDC78	NDST4	SLC45A2	TRIM36	OTOGL	ZNF366	ENKUR	TNNI3K
MYBPC3	SLC11A1	BATF3	IKZF1	SRGAP1	SMPD3	CMKLR1	GFRA2	TOX	SPAAR	PIEZO2	GYPC
DTX1	CHRM4	FOXD2	TEKT1	IL31RA	HIST1H2BG	RRH	P2RY4	SLC12A3	SRPK3	GMNC	FAM184A
SNORD94	PKIB	DYRK4	NTN1	COL8A1	CLEC14A	BTBD16	SLC9A4	GPR21	HCN1	PADI2	SNX20
GALNT15	ZEB2	MYH7	CCDC184	SYNPO2L	TDRP	LRCOL1	PCNX2	CCDC60	FGL1	KLHL41	ASIC3
MIR423	IRF8	SGIP1	NRN1L	SYT7	ADAMTS7	SRSF12	ADAMTS20	B3GNT7	SPINK4	COL5A1	PPARG
BIRC7	CCDC27	PHACTR1	CACNA1B	CDH23	DEPP1	MYBPH	CDH15	SNORA27	CLSTN2	ZNF582	OLAH
SMCO3	RNU12	ZAN	DLGAP3	F13A1	GKN1	CRABP1	HIST1H4B	ROR2	CFAP99	C1orf54	KRT18
SCRT1	FGL1	AL162596.1	KLHL40	NTM	TMEM229B	IL17B	CHRM5	SLAMF8	ASB4	CADM2	PNPLA5
RCVRN	ATG9B	TYROBP	FGB	AGXT	TC2N	BATF	SAMD11	ADIPOQ	BVES	GDAP1L1	SEMA3B
CHGA	MORN3	LRRC8C	ACP4	C16orf86	HTR7	ROR2	HSD17B2	SPP1	SLC25A18	TAGLN	ALOX15
LOX	CCL5	MCMDC2	MC1R	MMP8	XK	STPG3	PCOLCE2	CRYGA	NR1I3	KLF14	CCDC88B
TEX43	CXCR5	GLRA4	TAS1R1	MPO	RAP1GAP2	PADI2	SPDYA	TMEM72	EN1	GPSM3	LRFN5
SCT	SRARP	PTPRN	DNAI1	PPP1R1B	DNAI1	SLC10A1	WIPF1	SNORA74C-1	RF00212	NACAD	HECW2
ANKRD34C	CLDN5	CRHR1	TMEM74B	SYNDIG1L	FAM83E	ANK1	RBM46	LHX6	KLRK1	LTBP1	CXCR3
KRTAP24-1	RNU6-1044P	INSYN1	CYBRD1	GALNT17	SERP2	SNORD66	SERPINC1	TMEM169	SLC10A6	CD93	ACSM4
TMEM235	BMPER	ACSM1	SPNS3	AMPH	FAM180A	STARD6	TNNC1	FGF17	SLC26A9	SAMD15	A1CF
RNU1-75P	NCF4	VIT	SLC28A3	GPR62	CABCOCO1	TRPC6	TESPA1	TMEM132B	CHRM4	OPCML	PALM2
KCNMB3	NR1H4	KLHL29	JPH3	ZNF804B	STKLD1	PDGFD	PADI3	TCF24	ADAMTS12	PARVB	PNMA5
ZNF382	MOS	KRT8	SEMA6B	STOX1	SGSM1	TMEM132B	HRCT1	SCARA5	DZANK1	KLHL29	ONECUT2

CASQ1	PRR19	MPZ	PRR5	MIR133A1	RNF157	TCF24	FLT4	ABAT	GAP43	KYNU	LRRC10B
SNORD89	RNU4-58P	ITM2A	KCNK16	TMEM163	RGS8	SCARA5	KLHL13	AK7	C11orf91	TBXA2R	RAB37
PCDHB2	PHOX2A	C1orf162	HOXA13	IL16	ZNF354B	CRMP1	GNG3	RAI2	BTK	FAM107A	ZNF697
RSPH9	PLA1A	ANO3	HSPB9	SMIM33	KRTAP26-1	AK7	FGF18	SNORD42B	SHANK1	GIMAP6	ADAMTS4
CLVS1	TPH2	SYNDIG1L	LRRN2	DNAJC6	C13orf42	SHE	LRMP	SLC47A1	LRMDA	LHX6	PCSK1
ZNF582	TEX22	ESRRG	FLT4	NECAB1	ECEL1	SNORD42B	ESR2	TBX2	GNG13	SPINK14	NAPSA
KLHL13	GCM2	PKD1L2	RND1	PANX2	PARVB	GATM	SLC18A1	ADGRE1	RN7SL230P	SOX17	DES
WNT8A	SLC6A1	KCNG4	SLC34A2	DLGAP1	SSTR2	MYT1L	ST3GAL3	ZDHHC19	KCNK1	DEUP1	SNORD110
NECAB1	ADRA2C	LMX1B	APOB	CYP27A1	PRR19	SNORD62B	GGN	MCOLN3	SNORA5A	ANKRD63	S100A2
STAC2	SERPINA11	PAQR8	CCNJL	NFAM1	PLPPR5	SEMA3G	ALPL	FAM19A5	CD3G	SCARNA18	CD79A
TPBGL	MIR128-1	ENPP6	OIT3	A2M	GPR179	HIC1	MAGEE2	PRF1	ATP1B2	B3GNT4	CLGN
CCL7	CNKSR2	UBXN10	HRNR	IL20RA	ZNF35	MYO1A	GCM2	GABBR2	DLGAP3	SLC13A2	SYT13
KCNMB4	SNORA55	SNORA2C	ADIG	SLC9A7	EPHA6	FER1L6	M1AP	ADAM21	RAB36	PEG10	CSF2
RIMS1	CCDC105	FAP	SLITRK4	WDFY4	ITIH1	TRIM9	CFAP46	POU3F3	CD28	BECN2	KCNJ8
ENPP6	TRIM46	CEP295NL	FOXF2	TRPC4	SFRP2	CCDC175	KCND1	CBLN3	CPZ	ADAMTS20	MYH8
COL8A2	ABCG8	PADI3	PTCRA	LMCD1	MIR423	PRR35	SNORA2C	COL8A1	B3GALNT1	ATP13A4	KCNC2
NLGN1	PTP4A1	SCARNA5	NDNF	CORIN	SLC6A1	CRP	SCARNA6	CHST7	NRN1L	CEL	P2RY12
ATP2A3	RYR3	NEK5	RGSL1	UPK3B	ACTG2	CLNK	CSF2	CYP7B1	CNGB3	BHLHA9	SMIM18
APOBEC3H	ALDOB	BICD1	KLF12	SP8	MYBPC3	TNNT3	CNDP1	LRRC18	FAM169B	PROK1	ST8SIA3
COL19A1	TSSK1B	NR1I3	TIMP1	TNFRSF1B	SNORA54	GRM6	SYT16	KCNQ3	LRRC26	ADAMTS13	AL096814.1
ELFN1	SLC51A	RPTN	ETV1	DDN	NKX6-2	GPR1	IGSF11	ADAMTS15	IHH	LHX4	METTL11B
HMCN1	NDST4	ALPL	FUT7	EXOC3L4	C3orf67	TNF	ACTG2	PPM1E	LRRC71	HES3	NPFFR2
ADAMTS7	TSSK3	CXXC4	FOXI3	SLC9A5	C1QL4	SRMS	A1CF	TSPAN18	KRT71	MT-CO2	HS6ST3
C1orf158	MEIS3	CDH15	SNORD38B	RASGRP4	WT1	CIB3	LONRF2	DNAAF1	CLEC3B	GIMAP4	RAPSN
FGFR4	OPCML	IQCD	HEYL	PDGFD	NPFFR1	ADCYAP1	RF02187	RAX	PRR22	FOSL1	ZC2HC1B
RNU6-1095P	DPEP1	CNGA2	SLC4A5	GP1BB	BARX1	SGIP1	SLC30A3	MGAT4C	FKBP14	GAREM2	MIOX
GPR18	KCNE3	GRM8	TM6SF2	CBLN2	CLDN18	COMP	PTPRH	GRM2	IQCG	CCDC198	BARHL2
ASB10	TYR	TNNT1	BCL2L15	CD69	RALYL	SLC9B1	NANOS3	TRPC7	SNORA55	FAM110D	CYP26A1
ALX4	IGSF9B	FAT3	CARD9	ESRRG	TDRD5	MCOLN3	DPT	F5	JAM3	DNM3	NPFFR1
RF00091	VWA3B	MYT1	C11orf96	AGBL4	OR52N5	TBATA	TMEM117	THBS4	METRN	HID1	CRYBA1
HAPLN2	FAM222A	ADAMTS12	RPRML	ATP1B4	ARMCX4	SOX17	KLRK1	HK3	ATP13A5	PRKAR1B	PTH2R
HAO1	KLHL10	ASPA	FXYD2	SLC22A6	AFM	H1FNT	RF02271	EPHA5	TMEM136	TMEM74B	SPTA1

NOVA2	CACNA2D1	ACP7	MAPK4	BSND	VASH2	RPRML	TH	OSR2	CCNJL	ZNF605	TEX12
PRAM1	CNTNAP2	EN1	RNU6-120P	NUTM1	HIST2H2AB	RBPMS2	EMILIN2	GLP1R	ADAMTS19	HTR2A	CPNE4
TEX44	RUNX3	PAX5	DYSF	GPR158	PHOX2A	SMIM18	KCNF1	RADX	RNU6-290P	PAK5	ATCAY
HJV	IHH	NKAIN3	PDGFRA	HSH2D	AC008736.1	ATP4A	SACS	FRMPD3	PEAR1	MIR711	ONECUT1
C1orf54	GDAP1	GIMAP8	SLC26A10	RN7SKP89	KLRK1	ADAMTS15	A4GALT	RPE65	SHANK3	HCN3	FOXI1
OLIG2	CCDC159	MYOZ3	VAV1	P3R3URF	SNORD121B	MRPL53	ARHGDIG	SLC19A3	SPEM2	SUN3	RNF148
SPEM2	ABCC8	GLYAT	ISL2	TMEM232	PGLYRP1	COL6A6	NLGN3	IQSEC3	RNU6-1044P	P2RY10	FOXD1
MFSD6L	C19orf81	CORO2B	NAPSA	KLHDC7A	LRMP	VWF	GPR82	SLC12A1	CAPN12	PTPRD	IFNK
SNORA63E	TRIM9	CCDC175	KCNE2	SRRM4	GBP5	LY9	NPPC	ABCC9	PNCK	LOXHD1	TRPM2
MIR345	STK31	SCRT1	SBK3	CPNE6	WFDC2	IL17F	DNAAF1	ADAD1	KRT27	CACNA1H	FGF18
MIR106B	FBXW10	SCART1	NMNAT2	DMBT1	BVES	TTC25	RNU6-1280P	TMC1	TNFSF13B	SLC9B1	CBFA2T3
RNU2-58P	GPR34	MUC13	PP2D1	IL27RA	LINGO3	CHRNA2	GPD1	CD69	ASCL4	MIR628	CLDN20
SUSD5	RAI2	STPG4	HVCN1	TCHHL1	S100A2	DISC1	ADAMTSL3	SIX3	TEKT1	GJC1	DDIT4L
SDR42E2	CLDN14	TAL1	CCNA1	AIF1L	TMEM26	SLFNL1	KRT36	GUCY2F	IDO1	CCDC69	CCDC196
MISP	SKOR1	KCNA4	ZEB2	COLEC12	CIDEC	TNP2	KLHL14	METTL11B	AATK	EMCN	HDAC9
NAP1L5	SNORD62B	CCN4	INHBA	LRRC4B	RANGRF	CAMP	BICC1	FOLH1	SLC26A5	GASK1B	ASB2
UTS2	AIF1	CHRDL1	GATM	TDRKH	C12orf75	CNTN2	GNG2	BEST3	TFAP2D	ACBD7	RAB39B
TM4SF20	ADAM11	MCEMP1	CA3	COL25A1	JPH4	FUT7	ATP13A4	HNF1B	MRAP2	CPNE7	FOXD2
FBXO39	CCBE1	SOAT2	SNORA23	TSPAN1	ANKRD40CL	LIN28A	ITM2A	MEP1B	SAMD13	FBLN2	IGFBP2
PRAP1	CHRM3	CPLX4	PRSS27	AGBL2	SNORA62	CTXND1	MYO15A	AKAP3	TTC24	HIST1H4B	SV2B
C16orf86	RBFOX1	IGSF1	FHAD1	PCNX2	WIPF3	GATA1	NR4A3	CEACAM18	GPR17	CHADL	SLC25A34
PLA2G5	TBX15	ACTG2	FMNL1	SNORA12	TNIP3	CHAT	DUSP13	MYRFL	AFP	PRUNE2	RN7SKP127
SEBOX	ITGAL	RF00212	ZDHHC22	SEMA3B	SNORD53B	PLA2G3	SYTL5	ARHGAP36	MYL3	CD96	KRT72
FRMD3	WDFY4	C2CD6	ADAM11	INHBA	IFITM5	ASPHD1	KLK6	CSF3	TMEM233	ZNF449	CNGA3
ELOVL2	UNC45B	SNORA47	RANGRF	SNORD11B	PTPN22	C4orf45	FOXF1	ASB10	LDOC1	HOXB9	GRID2
MIR221	S100Z	MEOX2	PCARE	NLRP6	GCNT1	IQCG	GPHB5	LRRC17	SELPLG	SLC17A8	DAZL
COL28A1	ROPN1L	ZKSCAN2	PIK3CG	EMCN	SHISA4	SLC44A3	CCDC152	C3AR1	CLDN19	MT-CO3	NOBOX
FRMD7	HAAO	CHST11	ADGRF1	KCNJ9	HAVCR2	TAL2	SNORD62A	RSPH6A	SLC27A2	INSRR	SLC34A3
MPP3	LRCH2	TSPAN12	SULT6B1	AK5	SLC27A5	PRSS57	GALNT16	PNMA8A	CD2	KIRREL3	SLC6A12
PCSK2	ZNF423	C10orf62	OPN5	LRRTM3	EREG	SNORD117	DNAH10	OR2A5	HFM1	BST1	BRINP2
LTK	CPNE9	COL28A1	HGFAC	SHANK2	NOX4	PRRT1	CLDN20	GPR20	DOC2B	CDKL4	ALDH8A1
PKD1L2	CLIP3	MYRIP	RSKR	MB	USHBP1	NSUN7	CFAP54	LRTM1	C9orf24	SRSF12	NDST3

GRIK3	INSC	GASK1B	PDZD9	NTN3	LBX2	OR8D4	CCDC36	MSGN1	FAM155B	ARMH1	PABPN1L
SLC6A15	BOLL	ITGA8	ALDOB	ADAMTSL1	TBXAS1	SEMA3A	EBF2	CFAP65	12-Sep	EGR2	SSTR3
PDE6B	ITK	SEMA3E	ESPNL	AVIL	CKM	KLK12	ARL11	FBXO40	COLQ	KCNJ10	RNU1-100P
SARM1	KCND3	MAP7D2	ISM2	KIAA1614	KCNH5	HID1	SORCS1	PLCXD3	SNORA80E	RASGRP3	RNU6-931P
SYNJ2BP-COX16	RNU6-290P	MYBPC3	C5orf49	HIST2H4A	TFPI	SRRM3	CPA3	KCNK3	RF00340	CACNA2D2	ZIC1
ITGAX	SPATA17	CCDC92	CFAP57	EMID1	FBXW10	LRRC52	CACNA1H	GK2	CALY	TEAD2	FASLG
VNN3	HECW2	TNFRSF11B	CLIP3	STOML3	KIAA1324	DNAH6	MMP12	OR6Y1	LBX2	SEC16B	TPPP2
SPINK6	HECW1	B3GNT6	SLC29A4	MATN4	CYTL1	TSPAN18	ADGRF3	IL1RAPL1	BANK1	DNAJC22	HORMAD1
ZBP1	CD38	COL6A2	CDK14	COL15A1	CLHC1	RIBC2	RASGRP2	OR9Q1	SCGB1A1	CERKL	CCDC22
SAPCD1	SPO11	WNK3	ZFHX4	C20orf144	LRP1B	EFCAB9	SLC25A21	MAGEL2	TSKS	CASQ1	SCGB3A2
ACTL7A	C7	SNORD17	LAMA1	SLIT2	RNF183	RF00153	CIDEC	MYH13	LINGO4	CCR2	DLGAP2
ANK2	PATL2	STXBP6	C12orf75	SARM1	TMC3	ERG	ADGRG5	AGBL4	PROCA1	FAM78A	TAS2R41
RADIL	SLITRK4	CDH5	C19orf71	SNCAIP	HNF1A	CHST2	HMX2	GPBAR1	Z98752.3	RNU105C	RF00026
NID1	OLIG3	COL14A1	AJAP1	MEGF10	ZNF521	GCK	CDC20B	RNU6-178P	OBSCN	SRRM5	EIF2S3
SLFN5	CDH12	PCDHGA11	SYNPO2L	HIF3A	GDF11	PHLDA2	LRRC9	RNU6-1279P	FAM89B	DPP6	BTN3A1
AGR3	NKX3-2	FGF18	GNPNAT1	ADAMTS8	RF00604	GPR18	PLA2G10	RNU1-14P	PTPRN	SLC45A1	HPX
BLK	MROH7	CCN2	KRT73	HYDIN	ARPP21	TRDN	CD6	KNDC1	SLC34A2	LVRN	SEC14L5
SNORD63B	TRHDE	FOXE1	INMT	XIRP1	CPNE9	BLK	SALL4	DDX3Y	AC087651.1	MYOZ1	DNAH5
NPW	KCNC1	LSMEM1	UNC80	HCAR1	BCAT1	LSMEM1	FGF16	TAAR5	SNORD62A	TMEM163	SLC38A1
DGKG	MAPK4	PCDH12	ZSWIM5	COL6A2	ISLR	FRMPD4	MPPED1	CCIN	MYO15B	TMEM215	SNORA58B
TNFSF13	FUT9	DIO1	AC008736.1	RBM24	CDH20	HUS1B	MRGPRG	OR52D1	KCNIP4	BATF3	MIR27A
RNU6-200P	SMIM41	LAYN	SYT2	PNCK	TRPC7	PARVB	SIX1	SNORA35B	BRMS1	GBGT1	PPP1R3G
RHOC	CACNA1H	CHRNA9	RGS14	TMEM132D	MLIP	HIST1H2BM	MIR652	RF00411	GPR151	RNF151	ARNT2
TSLP	FMN2	RS1	TTLL9	PLLP	ATOH1	AL096814.1	MIR874	RN7SL838P	TMEM8A	SPINK1	MTUS2
GFRA3	FGF5	PRMT8	VPS25	HAPLN1	ADGRB3	GLIS3	NLRP12	PCDHA2	SERPINE2	HRASLS5	EPHB1
DUOX2	PRLHR	NDST3	TG	CHRNA1	ATF7IP2	LVRN	RNU4-34P	AC010616.1	PACRG	LONRF2	CARMIL2
STAT4	NT5C1A	SNORA5C	CYP17A1	DHRS2	IQCH	CFAP65	RNU6ATAC14P	DAZL	KCNK16	RNU6-11P	KRT2
TACR1	TBATA	PTAFR	SNX20	ASIC4	NCAN	CXorf21	RF02104	LVRN	ADAP1	RNA5SP463	HCST
SYN3	H1FNT	RNU6-243P	C11orf91	LMNTD1	MIR628	CAMK2A	RF02271	HTRA3	SULT6B1	LARS2	TEX54
CH25H	GP1BB	DISP3	RIPOR2	CCDC146	SNAI1	P2RY13	PDGFRL	CACNA1I	MMP19	CNTN3	GLIPR2
TNFRSF13B	F5	KIAA0319	TH	DOCK2	GATA1	RECK	SLC5A5	ELAVL4	CFAP70	ATP6V1G3	ZNF385B
RGS6	GK2	TWIST2	ARMC12	CCDC33	IQCA1L	KRT71	PALM3	UBQLNL	ADGRG3	CPXM1	EPHA3

SNORD98	PEBP1	HABP2	APOD	FLNC	TRDN	C16orf89	DSG4	SKOR2	C19orf38	SRPX2	SNORD18A
HAVCR2	TAL1	ROBO4	C12orf56	ANKRD65	IGSF1	TSPAN33	SRRM5	ZIC5	SLC44A3	MYT1L	SLC9B2
RNU6-638P	KCNA3	OR6X1	PPP2R2B	CACNB2	PCDH12	DLL4	KIAA1211	RGS22	PRSS35	RTN1	RCN3
PFN4	CYP19A1	RNU6-929P	STPG2	WDR38	NDST3	MMP23B	KLK13	TUB	IGF2BP3	CHST13	KCTD16
LRRC19	FAM166A	CLEC4G	PRELID3A	HERC6	GK2	HAAO	KLKB1	SGCZ	IGFBP6	HOXC9	ACSBG2
DOC2B	PIWIL1	HIST1H2BE	SYT9	ARID3B	THEMIS2	CDCP2	XIRP1	FGF14	DLEC1	ANGPTL1	FADS2
ZAN	PRDM5	ST6GALNAC4	KLK6	UBXN10	NPS	CD180	ST8SIA1	MUC5B	TEX14	MINAR2	OTOP2
HS6ST2	KCNA4	C1orf146	IL1B	GNG2	SYT16	HCN4	SNORD127	GFPT2	TNN	ZPBP2	ABCA9
CHRD	LINGO2	RPL7A	PATE2	EGFLAM	IRX6	NXNL2	SMC1B	RTN4RL2	ZC4H2	ALS2CR12	MROH2B
CRACR2A	MYL1	GNG13	LOXL1	CYP2U1	MSTN	HAPLN3	TNNI1	KLHL33	SLC41A3	NEK11	C10orf99
MMP21	C13orf46	KYNU	TTN	C19orf66	NEK10	MIR423	HGD	ZNF697	ANKRD40CL	CFAP52	HRH1
P2RY4	ALDH8A1	DGKG	TSSK1B	FGF18	RNU1-100P	KCNJ11	PLIN4	DMBT1	RUNX3	ADAM32	BEND6
MAMDC2	ANKUB1	IL2RB	STAP1	ISLR2	ETV1	GALNT14	RPL36	PPP1R9A	NPHS1	GJC3	RGS18
ST6GALNAC4	CNGB3	C20orf96	PTK6	CFAP45	B3GNT4	MKX	GABRB3	PDZK1	FFAR4	ITGA9	SP6
THEMIS2	SCN2A	PSTPIP2	LCP1	SCML4	CDH10	CALML4	TSGA13	CXorf21	ESPNL	SYNPO2L	NKG7
RBPMS2	NDST3	DLL3	PAX8	LGR5	NPAS3	UNC45B	NEK11	PKD1L2	CLEC4A	ARL11	B3GALT2
NPS	KCNJ4	KCNMA1	TMEM88B	KCNK10	GFI1B	METTL7B	GDF7	AQP5	C2CD4D	FGF17	SCARNA12
GRIN2B	CLVS2	MIR10A	CHAC1	ADAMTS5	RFX6	CHRNA4	CPB2	CYYR1	PTPRC	FSCN3	PRRT4
KCNS2	ABCC12	RBM11	SNTG2	UBAP1L	WSCD1	ZNF575	MYL3	HTR6	S100Z	C12orf71	ENTPD1
TNP2	ADAMTS13	FAM184A	MFNG	BMX	CCDC178	EBF1	PPP1R42	KCNE2	RNU4-89P	SNORD117	TDRP
THBS4	RNU6-895P	AC055839.2	PDE6B	PPP1R14D	MYO3A	DNAI1	C1QL4	MAP7D2	CADPS2	SPP2	TMEM169
GNRHR	IRX6	GLIS3	CAPN8	EBF1	RP1	GPR65	MYOD1	TMOD1	LY6K	KCNA3	CD163
LRRC17	MYOD1	ERICH5	ALOX15	TMEM150C	NEUROG2	SCART1	MMP20	GRM8	C18orf54	SPTSSB	PPP1R27
NPPB	TUBB1	LMX1A	3-Sep	SPARCL1	CSF3R	LGI4	PRTG	ANO3	PI16	TEPP	NRXN3
SYT16	GPC5	SPACA9	NOX4	KLKB1	DKK4	C2orf73	FAM50B	MSH4	CCDC155	PHACTR3	SFXN4
ZNF804B	NKX2-2	OXT	GPR182	ADAM11	SPATA19	DENND2A	NOL4	P2RY13	F7	VGLL1	MAP6D1
CPB2	DRC7	PRAM1	TRIM63	CCRL2	RSPO4	ANKRD34A	KLHL34	PLIN1	PAPOLB	PEBP4	CORIN
KCNA6	IGDCC3	CASQ1	MTUS2	TRPM3	SLITRK2	CFAP69	OR6F1	RFTN1	SLC39A4	RXFP2	B4GALT5
SLC1A7	RUBCNL	TMOD1	FSTL4	LRIG1	TAAR9	FOXF2	OR4D6	FOXF1	GPR183	LRRC66	RFTN2
CCN4	GPR176	NKD2	EMID1	HCN3	SMCO1	SUN3	TMIGD3	SFXN4	SNORD63	PLEKHG1	TNF
FOXH1	BHMT2	RNU4-89P	NHLH2	SHANK1	ZG16	PTHLH	RNU6-174P	FSTL4	QPCT	EGR4	EID3
SAXO1	MC2R	GSDMA	SLAIN1	NT5E	VSTM4	CNGA2	GMNC	TNFSF12	KIT	SMOC1	APBA2
AFP	OR6K6	PNMA3	IKZF3	DAGLA	MIR216A	AGXT	TOX	AGTR2	CBLN1	SERPINF1	UTS2

LRRC9	DNAJB8	RSPO1	HAVCR2	RTP4	MIR203B	GPM6A	EEF1A2	SLC6A19	EOMES	CCN6	NEFH
LHX4	ATP6V1E2	IRF4	CBFA2T3	GULP1	UBE2U	CRNN	FCER2	DTNA	CCT6B	ARPP21	GUCA1B
ADAM33	AC073611.1	CFAP44	STX19	HAS2	IGSF21	ACE	TRIM63	TSPAN33	KPNA7	SIX2	AC021072.1
PHACTR3	MUC4	NES	SYNE4	ADGRB1	LY6H	RN7SKP231	RTL9	PEBP1	RIPPLY2	EPHB2	BMPER
ENPEP	PLSCR5	ZFP92	SLC6A15	CCN2	MAMDC2	GDF5	APBB1IP	ALX4	OR6C3	HCK	PDE1A
RLBP1	CCDC141	CNTN4	CALHM4	ZNF382	C20orf173	ERC2	KCNH7	ITIH3	SPPL2C	GIMAP1	BATF
TMEM74	ODF3B	KANK4	G0S2	AIFM3	DOK5	SLPI	SNORD11B	TRIM36	NRGN	NALCN	PLIN5
MIR151A	PDZD3	TMPRSS7	SLC39A4	APBA2	PATE2	CYB5R2	FXYD4	KDR	NOTO	GBX1	DKK2
CCDC190	SLC29A4	ELAVL2	SATB2	SFRP5	BRMS1	AKAP14	FAM169B	SOX30	CNIH3	SKOR1	HTRA3
TRIM34	DNAI2	ARHGAP20	NWD2	NEK5	FYB2	UPP1	OAZ3	FBXO27	MRLN	TNC	SNORA2B
OR11G2	TNFSF11	RRH	F13A1	SETBP1	APC2	ASPA	NRXN3	CAPN11	STKLD1	TMEM59L	NLRP3
OR5A2	4-Sep	RAB3C	LPAR4	GLIS3	ARHGAP30	SVIP	LIPN	NTN3	PGR	FABP4	SLC22A6
SFXN4	MYRF	RNU6-290P	RHOF	EBI3	TMEM8A	ASCL3	RN7SKP56	FBXL7	UBASH3A	DLG4	OTOS
VIL1	TWIST1	PPARGC1A	RTBDN	SYN2	PLVAP	PPP1R1B	RNF17	KCND1	COL6A3	AMER2	PAMR1
HIST1H2AE	TMOD1	PIPOX	DPEP3	SDSL	ANXA9	TTR	PLA2G2E	THSD7A	ST3GAL3	REP15	SNORD123
EFEMP2	TTC16	PLEKHS1	BCO2	C20orf96	NYX	PABPC4L	FRMD7	ZC3H12D	FNDC7	HIST2H4B	MFSD6L
CPSF4L	VEGFC	ASCL5	AK5	DENND3	CCDC30	ETV1	SPATA45	HCN4	ISL1	DPYSL3	MMP20
TRPV1	KCNV2	LGR5	TMEM35A	C19orf85	SLC18A2	DMRTA1	HVCN1	FGF7	SPATA20	GPR75	IL13
LRRC15	ILK	CACNB2	EXOC3L4	OIT3	PAX7	RNU4-58P	VIPR2	C7	CASKIN1	GRASP	NPHS2
PCDHGA3	C1orf162	TBC1D9	TBX6	RBM11	IKZF1	IFIT2	SNORA20	MYO7B	SLIRP	AIF1L	PCK1
LGR5	SPRR4	SNORA55	HPSE	RN7SKP231	IGF2BP3	LRRD1	IPCEF1	RNU6-511P	C2orf40	SNORD34	RPH3A
MYO15B	C3	HSD17B2	MATK	FUT7	COL6A3	RHAG	SMIM22	KCNJ11	RAB44	THSD7A	TEX29
HIC2	PTPN7	EML1	MCOLN3	FLT4	CFAP54	GJC3	PRR18	MAEL	ST3GAL1	SLC35F1	EDIL3
RTN1	LEF1	NECAB1	GRIA3	HOXC10	HRCT1	LHFPL2	ANO4	C5orf52	TNIP3	RPRML	ZEB2-AS1
PLXNA4	PLCB2	EPHA3	AIF1	SCARA5	CELF3	CD4	CCDC158	DOCK2	SGCD	PTHLH	RNU6-969P
SYT17	PTGER2	HEPACAM2	PIEZO2	NUP62CL	CCDC159	P4HA3	TBX21	SLC5A11	RAB3B	PPM1E	SYCN
PACRG	ATOH8	KCNQ3	GSG1L	ADCY10	AXDND1	C2orf40	SGCE	RTL5	CHST1	SH2D4B	RNU6-701P
KCNMA1	MOGAT1	CHRD	DRP2	RNU6-290P	DERL3	SNORA62	C1orf105	FBXO39	SH3BGR	SCN3A	RF02187
ANKRD40CL	CRABP1	TSGA10IP	CRTAC1	IL18	CTSK	TAL1	DLGAP1	FSD1	WFDC5	NOXRED1	PHYHD1
CCRL2	HLX	RF02176	HIST1H2BG	TRIM67	MC1R	LEPR	NLGN1	TCHHL1	SCARA3	DNAH9	ITIH3
TMEM151A	FGB	ITGAL	ALB	CCM2L	VWA3B	FNDC7	KLHL38	SRRM5	C11orf96	CYYR1	MYH11
EREG	SP140	KIRREL3	CPNE9	JAKMIP1	PRSS42	CABP7	TLR4	GIMAP8	TMOD2	CNR2	MYO5C

SACS	LHX3	FIGN	NEUROG3	GPR18	CHSY3	MAK	ELOVL3	CRP	PJVK	KCNT2	NEXMIF
NCALD	NPHS1	SPATA17	GABRA1	CASS4	KCNS1	WNT8B	IGF2BP1	CCDC85A	COL2A1	CCDC81	TAS1R1
FLNC	FFAR4	MYH6	FUT4	USH1G	DLGAP3	TIFAB	COL2A1	C5AR1	ARTN	LHFPL5	HIST1H2BD
SLC9A2	BMX	SELE	AL096814.1	C14orf180	FZD9	KCP	RNU6-1299P	ZNF831	AC011529.1	IRF8	CD244
NTSR2	CHRDL1	CDH19	MOAP1	NKAIN3	CUX2	PREX2	UPK2	PRMT8	CD27	LRRC4B	SOX30
NAALAD2	FER1L6	PTGIS	ELOVL2	PTAFR	CCDC102A	LTC4S	FAM184A	CPNE7	ILK	RTKN2	APBB1IP
NXPH1	LIPN	CPA3	FAM89B	PNMA3	OLIG3	ANKS1B	NCKAP1L	CDH15	ITGAL	HIST1H1A	C1QB
MYO15A	FBXO16	MMP25	P2RY2	CLVS2	PCDH9	LRRC27	FYB2	DENND2A	TMEM45B	C4orf54	GABRB3
FBXL2	TULP1	PDE10A	HOXC4	TMEM130	DLX6	TSHB	SLC12A3	CFAP69	HEATR4	ITIH2	IL17B
SBK3	EFR3B	CHGA	ELF3	ABCC2	RARRES2	KCNK9	ZEB2	TRANK1	SYNE4	SERPINA5	MAPK4
RGS8	SHOC1	MIR128-1	KRT4	SNORA17B	SCARNA5	SCN3B	PENK	CCL2	CDK14	PNMA1	GABRG1
WASF1	EML1	ASMT	MTCL1	KIAA0408	ESPNL	IFI44	MRLN	PTHLH	RF00602	CABP7	REC8
KLHL29	SAMD11	TM4SF19	A4GALT	PPP1R1A	3-Sep	TNFRSF1B	ARMH1	ANK1	LENEP	IQUB	OR12D3
PAQR6	POMC	RN7SKP11	AIF1L	AK8	HVCN1	SYN2	RF00432	PRKG2	MFSD2B	DIPK1C	SLC3A1
P2RX5	TBX6	LRRC74B	AMH	GLP2R	GYPC	CCDC102A	KCTD16	GDF5	KLHL22	LRMP	SYTL5
RNF150	SERPINA5	CALCR	IYD	DCC	TTN	OR2K2	PCDHGB4	SLPI	SLC35G2	NOX1	GUCY1B1
SLC24A5	SNORA21B	ASB15	FZD9	C2orf88	BIN2	SIT1	NALCN	UPP1	RN7SKP11	ZFP82	SDS
NPY	PRR15L	STRA8	GRASP	CADM3	CLDN23	MYOZ1	ONECUT2	KCNQ4	ZNF473	STMN2	SMC1B
RBM46	HMGCLL1	ATP4B	TEX45	STPG1	PCARE	STMN4	TMOD1	C1QTNF6	LCK	CDKL1	PGLYRP1
KIF1A	CHRNA2	NKX6-2	PLEK	HECTD2	RNU6-1044P	NR2E1	CXCR6	IFIT2	PIK3CG	GUCY1A1	SNORD53B
SLC17A7	PGR	RTL3	SERPINE1	KLHL29	ABHD16B	HTR7	TCAP	NOG	INTU	CHRD	IYD
SEMA3E	TP53TG5	USP51	GNG5	HDC	KCNIP3	ANKAR	FAM19A5	PLB1	LCA5	GPR34	MIR365A
FOSL1	B3GNT6	PABPN1L	ANGPTL1	SCARNA11	PHF21B	LRRTM3	TMEM136	PREX2	P4HTM	SRPK3	MIR23A
HEPACAM	TCAP	ECT2L	BPIFB4	RASAL1	NOL4L	SLURP1	GALNT9	FLNC	FXYD4	CHGB	TNFRSF8
GLI1	C11orf16	PAPPA2	LOXL4	PPM1E	NHLH1	MB	ITIH3	FAM20A	RASAL3	EFCAB10	KIF17
MCOLN3	TSGA10IP	CDC20B	PLCH1	TRABD2B	HS3ST1	MYCBPAP	RNU2-58P	SYCE1L	ANKDD1A	TAS2R3	TAL2
EBI3	HTR6	RF02140	GJA8	ADH7	SPATA6L	CALHM6	SNORD18A	IFI44	LYZL4	KLB	RNU6-384P
RNASE10	TMOD2	CD163	SPATA45	NTNG1	ITIH3	CPLX1	GABRA4	ELN	ZBTB46	SHROOM3	OLFM3
POU2F2	CNGA3	CTNND2	TMEM178B	ANKRD34B	AMDHD1	SYNPO2L	NPW	TDRD6	LHFPL6	SPINK4	CLEC5A
MMP9	USP13	TAC4	CTSK	LAMC3	SNORA27	FABP3	PPM1E	RAB3C	FAM186B	ZNF853	KCNG3
FBP2	HCK	SNORA80E	NTSR2	RAMP1	TMEM132B	ART1	RASL10B	ABCG8	ARMC2	MYL1	SNORD94
SYTL3	PCDHGA1	HMCN1	STYK1	COL4A4	EEF1AKMT3	C11orf53	MEIG1	LRRTM3	C1QTNF3	KRT34	LSMEM1

OPTC	RAB42	SMIM38	RASGEF1A	SLC14A1	KHDRBS2	GP5	C1orf158	MB	SAG	BCAS1	TP53TG5
RRAD	SYN2	NDST4	LGALS2	HIST1H4E	ARHGAP8	GPR62	LMX1A	PTCH2	KIF6	LAMC3	GUCY2D
CHRNA1	AK5	GATA2	CD74	KLHL13	RAB44	ASMT	BARHL1	C17orf98	SAT2	SLC2A2	CCKBR
ZNF641	NDP	FAM107A	HOXA1	SCRG1	BEND4	C9orf24	KLHDC7B	PABPC4L	PCDHGA2	C13orf42	RNASE6
KLHL31	B4GALNT2	PROCA1	IL23R	RUNX1	MRO	C1QL1	TBXAS1	PRAP1	CROCC2	TMEM236	TGM2
CCDC151	CNN1	CCDC102A	SLC51A	RTKN2	TMPRSS11D	RGL3	NR1H4	SMCO3	SRMS	PRPH2	CKB
KCNJ6	CHRNB4	DACT1	SPINK4	UPP1	FGB	MAGIX	GPRC5D	C20orf144	ANXA3	FCRLB	OR2I1P
STPG3	SNORA27	KIAA1211	LDB3	CALCB	SLFN5	RAB26	KRTAP15-1	VSTM2A	SAMD9L	IGSF1	A4GALT
FSCN3	ZAP70	ARHGEF9	MATN4	CCDC106	APOBR	MYBPC3	MASP2	PPP1R27	STBD1	SERPINA11	SNORD66
TMEM200A	CARD9	LHX2	ELF5	CBFA2T3	GABRB1	GMFG	CCDC170	GDF9	CLEC6A	ROBO4	TTLL6
SLC9B1	SFRP5	ZNF521	SNORD87	PCDHGA5	GIPC2	MMP19	HNF4G	C1orf100	RPS12	HIST1H2BE	RS1
IL17F	CCDC65	KCTD4	TEX22	ROS1	PPP1R3D	FAM171B	ABRA	CCDC152	CD53	HJV	KDM5D
SPAG4	PCARE	NXPH1	BEST2	ASB11	CD52	TMEM130	EDDM13	PDGFRA	CDH11	RSPO1	SCN4A
TMEM163	TEK	DUSP13	CCT6B	RAB39B	SERPINF1	ACTL7A	CCN4	ACCSL	OPN1SW	MCIDAS	DRC7
DUOXA2	CFAP52	PCDHGA4	CCDC24	SLC2A10	PRRT1B	GPER1	SNORA47	KCNH7	P2RY2	FGF16	OSCAR
GPR50	STK33	SLC12A8	TNF	CCDC151	CCNA1	SCN2B	SNORA63E	OR2I1P	CAVIN2	CELSR3	GABRQ
CHN1	LIMCH1	ARMCX2	SYNGR3	ADH4	PYROXD2	SYNGR4	SLC22A2	MECOM	CP	MYLK2	FAM135B
KCNQ2	ATP6V0D2	KIAA1324	FBXL22	RGL3	LCP1	CABS1	LRRC74B	LTBP1	GP1BA	TEX46	PENK
HPSE2	SLC24A1	SCRG1	ARAP3	ADAMTS13	HSPA12B	TRO	TTC9B	STC1	AC005551.1	OR9A2	DPY19L2
PKLR	AGXT2	LRRC39	ENHO	CCDC184	GMFG	GABRG3	SLC35F4	TNFSF15	LPXN	CCR5	ST6GALNAC5
TLR7	IGSF11	MAGEE2	AWAT1	NOBOX	NPM2	MIR199A1	FSIP1	TENT5D	GGACT	NDST4	ABCG8
ASPHD2	GGT7	KCNH2	EAF2	LBX1	PSTPIP2	RNU6-365P	CACNG5	RN7SKP56	SLC30A1	CPA4	LEF1
RNU6-243P	RNF222	AMZ1	XPNPEP2	DUSP27	ATP8B3	GFRA4	SYCP2	FXYD2	GALR3	NTN3	NRCAM
CCDC184	AMBP	GUCY1A1	KCND1	BARHL2	A3GALT2	OR6S1	TAC1	TAL1	MEIOC	CLEC3B	MFAP2
EQTN	IL13RA2	SLCO2B1	PAPOLB	TG	SHH	CTHRC1	OR11A1	C5	GNG5	RELL2	PLEKHS1
ACP4	CRMP1	SERPINB11	GSG1	ELAVL3	ADAP1	TM4SF19	MT-ATP6	CD40LG	LTK	AQP9	PLPP4
C3orf67	RASAL1	RNF150	FABP12	ABCA13	LRP11	DRC1	RNU6-270P	GDF15	C16orf54	PCDHB7	POU5F2
RNU1-100P	RHBDL1	DAB2	SPRY3	SLC25A41	C9orf116	CASQ2	RF02174	TMEM130	CLEC7A	GREB1	IL9R
CCDC22	SNORD15A	FBLN2	IGF2	P2RX1	RIIAD1	PITX1	RF01879	CCDC42	B3GNT6	KCNAB3	GDF11
CABP5	EBF3	NTRK3	DOCK3	COX8C	MDK	IDO1	BX255925.3	PLD4	RN7SKP231	FKBP14	AC055839.2
VMO1	SPATA9	NTM	NLGN3	SNCA	FSCN2	BTLA	RAG1	CTCFL	HLX	FAT4	LRRC75A
KLHL30	RNU4-1	TSPAN2	HS6ST2	HSD17B3	SPATS1	MBOAT4	TMEM121	RNU1-123P	PKP2	IQCG	ATP2B2

ZCCHC13	ADAMTSL2	RASGRF1	IGSF21	FFAR1	ACSS3	RNU6-470P	SNORA12	RNU6-351P	GHRL	TGM5	MMP13
EMX1	ISLR2	FOXC1	ALS2CR12	FAM183A	NPY	CFAP73	PSPN	ERICH3	CCDC30	PDZD3	ZYG11A
GDF6	TXLNB	AANAT	ONECUT2	OR9H1P	RPTN	FAM166B	LPXN	PKD1L1	XK	SLCO2B1	CD7
KCNIP1	CFAP70	GCNT4	HEPACAM	UBQLN3	PALM2	MAS1	RTN4R	ACE	RIBC1	COL6A6	CNFN
DNAJC5G	C3orf62	GSAP	PYY	UNC13C	HIC2	SCARNA18	FBXO27	P2RY14	GREB1L	PLPP7	ITGA11
ADAM12	ADAMTS19	CALD1	CCN6	MIR187	ARG2	SPACA1	GJC2	KALRN	CEP295NL	RAMP1	CABCOCO1
OSCAR	KRT82	AGR3	C4orf48	CLDN19	AOAH	SCARNA5	LDLRAD1	SVEP1	PPP1R3F	MAPK15	AMN
KRT40	SGSM1	CPLX1	GPX3	AL096814.1	TNFSF13	GLIPR1	LMO2	KCNH4	NR2F2	C3orf18	PLA2G3
MCIDAS	CCNJL	1-Mar	STOML3	USP44	LRRC27	PRRX2	CNR2	SOX18	SCARNA7	PLCL2	TGM1
LRIT3	RNU4-2	ANGPT2	HIPK4	CEP112	CCDC177	CES4A	SOX5	WNT2	KCNJ14	RGS6	SLAMF1
FRMPD2	WDR38	GPC6	WNT8A	TTC16	CRYBA2	MYOM2	SYT17	GULP1	GPD1	CAMKV	PPP1R1C
RNU6-1122P	TMEM173	GPR3	ASB14	ITIH2	ASPN	LOXL2	C12orf60	KHDRBS3	PATE2	ARHGEF17	LAIR1
CYYR1	SLC26A1	COL4A4	CDHR3	HLX	SLC25A43	AFM	P2RX3	RFX4	CHST9	TMEM44	SELP
CYTL1	CAPN8	FCER1G	FXYD4	FBXO39	GNPNAT1	PCDHB3	SERPINI1	CYP2U1	ELAVL2	AJAP1	STUM
KCNE2	CILP	IL13RA2	PPP4R4	PCSK6	B3GNT3	SLC10A4	SLC38A5	ISM2	MIR194-1	TSHZ2	SCARF2
SMYD1	ABCG5	RBP1	AC004233.2	DNAH1	SYNM	CORIN	NOXRED1	CCDC177	CD247	RUNX1	MAJIN
GRM8	WIPF1	PRDM5	CLDN7	CCDC168	C3	FSCN2	SCARNA7	STK32A	CHIC1	KRT19	DNAI2
ZDHHC22	SLC28A1	GDPD1	SDR9C7	GPAT3	ABCA8	SHCBP1L	CD86	VAX2	ALAS2	NEU2	ARHGDIG
GDF11	HDAC9	ITGB1BP2	DEPP1	SLC6A16	PAH	FAM124B	QRFP	FRZB	DOK6	FGA	STC1
GNAT1	DDR2	FER1L6	NANOS3	CD34	PTGS2	IL1RL1	SLC7A11	CNTNAP2	ZP1	CAPN12	FAM217A
RF00019	CTSW	DOK1	COLEC12	WAS	HGFAC	GDPD1	PSTPIP1	SFRP4	TIGD4	VWCE	TMEM71
PLIN1	CCR10	TMEM255A	P2RX2	ADD2	MYCBPAP	PTGER1	CD84	ANKS4B	KCTD7	PCDHGB1	RELT
CDH9	SLC15A3	THSD1	CLDN20	ARMC2	CCDC60	HEATR4	LOXL1	KCNH8	GDPD3	LRAT	SNORA21B
GMNC	CD101	AGTR2	ELFN1	SPINK4	SLC39A5	CYP2U1	RF02175	R3HDML	NT5C1A	HPCA	MRVI1
PAX8	ZBTB46	MRVI1	LY6H	SFTPC	MIR27A	PATL2	RPL7A	ITIH1	PPP4R4	TBX2	TCF24
ICAM2	KLF14	RBM46	ZPBP2	BCL2L15	NR2F1	TMEM119	MAP7D3	ARHGAP20	RPGR	KCNQ4	SFRP5
TMEM171	P2RY10	SGCE	PTPRQ	EPB41L2	ECT2L	ODF1	RBP7	PHOX2B	PCDHAC1	MMP21	TUBAL3
LRRC34	C1QL1	CYP2U1	GNAT1	KCNT2	KCNK1	RN7SKP89	EID3	SV2C	RWDD2A	AMDHD1	DLGAP1
LRG1	PRSS16	AATK	SMIM24	PLOD2	ESR2	SCARNA12	GNG13	RNU6-200P	KBTBD13	RNF32	SNORD11B
TRIM63	SCUBE3	CNTN2	TMEM182	BANK1	JAZF1	HCK	MAPK8IP2	SCG5	SOWAHA	ASCL4	PCP4L1
STK32A	JAM3	ADGB	S100G	PDE7B	TTC9	CDH2	ARHGAP40	STK32B	LHX1	JMJD7	NLRC4
AC004233.2	DRC1	SH3TC2	MMP23B	ADAM21	MORN3	LINGO2	RILP	LBX1	NYAP2	MYRIP	TNFSF9

HRH1	LIPC	CRISPLD1	KCNK13	CXCL12	ACAP1	OR51G1	MPO	KCNA4	HMX2	SDSL	CACNA1I
RAB37	LRP11	PEAR1	C10orf99	SERPINI1	AMH	FCRLB	PTGDR2	PIPOX	MYH6	CACNA1C	KCP
KLHL38	EXOC3L4	COL8A2	PLP1	STAB2	FLT1	RASGRP3	PLD6	C2orf16	CLEC11A	PSTPIP2	RNU6-929P
MFRP	CYP1A1	ACSM3	LRRC26	CLIC5	RGS16	STAC	ADAMTS12	TNNC2	RAPGEF3	RF006004	NFE2
MYO16	MPPED2	SLC1A6	NEFH	SLC5A11	NXPE3	NEUROD6	LIX1	ACTC1	RNF24	ADGRL3	PHACTR1
FHAD1	HS3ST1	RTL5	ACTL10	CD248	TEX15	CCDC81	P2RY14	EFCAB9	KEL	PDGFRA	RBM24
CHRM5	LINGO3	RILP	MAP1A	CUBN	HIC1	TMEM215	PLCD4	DHH	FAM124A	C11orf16	CCL17
KRT8	LST1	ADAMTSL3	COL27A1	CASQ2	CHRNB4	TTC34	KCNK16	GSC	NGF	IDO1	ZNF366
NRROS	PDE1C	GPR183	GJC3	SHROOM4	SNORD38B	OR1Q1	RGS1	FOXD2	DEPDC1B	FHL3	SPAAR
FAM186B	FADS2	ENKUR	DNAAF1	ANGPT2	ACBD7	RNU6-650P	FBXO41	MYO16	GMPR	SCUBE2	TRPC5
AIM2	C16orf54	ENPP3	C16orf46	DNAJB13	IL1F10	NTS	FAM78A	SLC6A12	PGBD1	EVL	SEC14L3
ARFGEF3	HCAR1	BDNF	ASPG	PLCB2	GPSM3	C15orf48	BRINP2	FCRL1	MOK	SPATA6L	ALDH1A2
EHD3	APOD	CLDN5	HCLS1	HOXC9	ATL1	AVIL	CCR9	RASGRP3	RNF224	BCO1	SLC7A9
COX7A1	NOX1	MMP19	VASH2	JAM3	OGN	LRRC34	TEAD2	CNTNAP4	MTMR7	CHAD	HCN1
GKN1	TMEM121	NEXMIF	RASL10B	POU6F2	RNY3	FMO3	GNG5	SRPX2	ACOXL	STXBP6	KLHL1
MEOX2	ACBD7	KRT34	BRSK2	ZNF287	CDH6	CLVS1	LRRC75B	TRO	NR1H3	LDOC1	ELFN2
ANKS6	FAM228A	CHRNA2	CORO1A	ITGA9	TMPRSS11E	PCP2	JAM3	MIR133A1	IL7	C1QTNF6	CDH10
PTPRT	RPL7A	TGM2	JMJD7	SCN2B	FAM186B	PAMR1	IGF2BP2	KCNA3	CFAP126	TTC25	RNF186
ACSM1	SCARNA8	PODNL1	RNU6-1280P	PIH1D2	PHACTR1	VSIG4	SLC29A4	PHYHIPL	KIAA0895	F13A1	RIMBP2
COL6A2	DES	UNC5D	TNNI2	COMMD5	EDN2	RAPSN	SNAP25	RNU6-871P	ATP12A	JAM2	RNA5SP194
LMOD3	CD207	ASPN	GALNT12	SCN1A	TM6SF1	STOML3	KRT23	BTBD17	ADAMTS2	C1orf100	CALCR
COX6A2	SPAAR	HOXB13	CH25H	EGR2	EMILIN2	ALK	TEX14	PON1	WFIKKN1	MYOZ2	ENPEP
HIST2H4A	PIPOX	ACTN2	SGCA	CAMKV	LGALS12	AMZ1	CLMP	MPL	RPL36	C4orf48	TSBP1
SCARA3	BCO1	ENO2	SLC10A6	ARMCX3	SNORD73B	TMEM171	GNAT1	SLC1A7	CD46	LTBP2	USP13
PDLIM3	NPTX2	GPX2	FGF14	CATSPER3	DYNC1I1	SSPO	ZNF648	KERA	ETV2	FSTL4	RF021004
SLC13A4	MINAR1	LMCD1	RNF17	MYO15B	ANGPTL1	ZPBP2	TNFRSF13C	GABRA6	CAMK2N2	C17orf64	SMTNL1
ECM2	CCL20	TBC1D30	CCR9	SAMD12	CRYAB	DPF3	JMJD7	TSHR	DGKG	LSAMP	C1orf94
ACTN3	SPARCL1	CACNA1S	LRRC46	HS6ST3	TBKBP1	OAS2	ANO3	SLC6A18	DLX5	TTLL9	SPATA32
BPIFB4	PCSK9	B3GNT4	CCDC87	SVEP1	C11orf86	KCNK13	3-Sep	HAPLN1	STK10	CLDN5	SLC36A3
PPARGC1A	RNF125	CD200	KCNB1	MORN4	RGS9BP	EGR2	CCDC68	RGR	RHOBTB3	SLC27A2	MUSK
GABRD	CATSPER4	CCDC106	STAC2	AC139530.1	CFAP57	C21orf58	LRRC19	CLDN6	BDKRB2	GALNT9	ZIC2
LINGO1	SHISA4	DBN1	ENPP4	GLIPR1	LGALS2	SNCAIP	WDR66	CDH2	GJB2	PLIN1	CTXN3
SFTPC	SYP	MED12L	FOLR2	NBEA	ASPG	TMPRSS15	CCR10	PDE6C	SHISA8	MUC17	RNU6-1234P
PCDHGB1	GPR21	KIAA2012	TMEM88	RF02271	CD160	AJAP1	SNORA80E	RBFOX3	SPATA46	AOC3	KLRK1

SYNGR4	SLC1A6	DNAJC6	CNNM1	SERPINF2	HPSE2	KLHL29	C19orf81	MSTN	GCA	SYT4	MADCAM1
CARMIL3	NLRP6	CAMK2N1		TNFRSF13B	GSPT2	MIP	RNASE10	TMEFF2	FMOD	TMEM217	FHL2
BRSK1	SERPIND1	NME5		SERPINA9	CACNG4	FGF21	MIR26B	DUSP27	ALOX15B	HTR2C	GSG1
FABP4	PRSS53	CACNA1C		ILDR1	TIGD4	MIR103A2	NOXO1	PTF1A	ADGRF2	HFM1	CD37
PPP1R3C	SELENOV	CYP8B1		IQCD	MYH1	MMP11	PTPN7	GALNTL5	DMRTB1	UPK3B	SLC10A6
HCLS1	ANAPC15	WFDC5		ZNF583	ARMC12	TAC3	RFTN2	AJM1	HIST1H2AE	CRHR1	SLC26A9
PRCD	PADI2	SGSM1		RYR3	MKX	CHRND	C8G	CDX2		RNU6-1095P	SLPI
CD37	CORIN	DOCK10		APOM	CCNB1IP1	SLC4A10	CD53	TMEM52B		ABCA8	HIC1
PPM1N	OMD	EBF4		RNF150	DNASE1L3	ELFN2	CD72	NECAB2		CMKLR1	CCNO
LRAT	DIO2	RPS12		DNHD1	TMEM37	FOXH1	ADGRE1	HCRTR2		GPR18	DCT
CFAP77	PAX5	PTPN5		PPP1R32	PCDHGB5	ASB4	ZFP69	RAG2		MRAP	ADAMTS12
JAM2	ANGPT2	RECK		ACYP2	SYT11	RIPOR2	TFPI	FSHR		CLDND2	STOML3
IL23A	RANGRF	TNFAIP8L2		KRT7	KRT76	MIOX	AGBL2	GPR101		SCART1	ASPHD1
ASB14	OR2I1P	CYP4F3		ZNF575	S1PR4	FMO1	KCNT2	MUC5AC		RNU4-58P	DZANK1
TSPYL5	KHDRBS3	ITGB8		CCBE1	RIMS4	GRIN1	DCLK3	4-Mar		RTP1	P2RY13
PIK3R5	KCNF1	MMP13		KATNAL2	FGG	ICAM2	TMPRSS6	LRFN2		C9orf24	BTK
OAS3	ENPP4	DOK5		FBN2	POU4F1	RAB36	KIF5A	NEK10		KCNA6	TYR
HPN	OTUD6A	GPR156		IL2	MIR150	UBD	TNNI3	XKR7		C10orf105	MB
GYPC	SMIM38	EHD3		AREG	TNNI2	CHRDL1	PTPN22	OR5M8		ACP7	CHD5
DENND3	FIGN	PPP1R3C		M1AP	SAT2	TSPAN12	ROPN1L	RAB9B		AC119396.1	ABCA13
CHADL	IL17B	FBN2		MAN1A1	MRLN	WNK3	TFR2	PKHD1		GPR176	GRIN2C
BTC	SLC34A3	LINGO3		CD37	MIR23A	CLIC5	CNR1	OR5AU1		TRH	SOAT1
SYT1	CTSK	KATNAL2		CXCR4	HIST1H2BM	LGR5	SGPP2	LINGO2		CABP4	NXPH1
RFLNA	STK32C	PHKG1		RNU6-431P	SNORD45A	ADGRG7	INTU	OR9A4		NMUR1	SLCO5A1
SLC12A3	SOX5	ADAMTS6		PLCXD2	LRRC75A	ANK2	KYNU	KCNA5		SUN5	KRT75
SPNS3	ASB5	BMPER		UCP3	TSKS	RF00026	KRT8	OR51G1		NKX1-1	KCNK1
UBA7	EYA1	COL4A1		SARDH	TEKT5	MYBPC1	RNF223	FAM19A4		GABRA3	SNORA5A
PLCH1	NEIL2	GATA6		COL23A1	STMN2	SNORD94	LOXHD1	P2RY6		MC4R	UPP1
RUNX1	BFSP1	RF00604		BHLHA15	RAB26	LOX	CACNA1G	ADRA1B		CYP26C1	TLR6
GUCY1A2	SNORD11B	HIST2H3D		KCNQ5	IFFO1	DYSF	HIST2H3D	SOX14		BPIFB6	CD3G
KCND2	PNMA8C	MME		PTH1R	CROCC2	FAM13C	TERB1	IRS4		TIGIT	PODN
C1orf146	GIPR	TNFSF18		IL4I1	RAB33A	SCARF1	PCDHGB1	OR1N2		RAB17	COL4A4

SELP	CHD5	M1AP		C19orf38	BMP3	EHD3	CNFN	PTAFR		MYH10	VSTM4
MIR194-1	MRO	ZBTB46		POSTN	EPHX3	CHRM4	RYR2	C8orf34		FAM78B	SIDT1
DEGS2	RAB19	KLHL13		CACNA1F	SERPINC1	FLT3	SMYD1	TMC2		TNFSF12	RAB36
RN7SKP127	ANO4	HDC		SNORD17	ZNF385C	MYRIP	CHIC1	TEX33		EXOC3L4	CNR1
TMEM232	SYN1	NLGN1		FRMD3	EN1	LEP	RGS14	CHRNA10		ADAP1	SLC46A2
FAM81B	FRMD5	SRGN		HIPK4	SLC38A3	ASCL1	CLHC1	LGI1		GNAZ	MYH7
SHISAL1	ANK1	CPA2		NFE2L3	TNNT1	CDH10	BTN1A1	OR1I1		SULT6B1	IHH
AKAP3	UNC80	NRCAM		DACT1	ABLIM2	ANGPTL8	DOCK10	CRYGB		BLK	C16orf86
PLCXD3	MIR339	SLC35D3		PABPC4L	ELOVL2	RNU6-1204P	NCCRP1	OR51A7		SPATA21	GCM2
C2orf73	C20orf173	LIPH		PKHD1L1	ADM	PTX4	F8	OR51F2		BFSP1	C1QTNF2
IL19	MYOM2	C17orf97		HPCA	LST1	OR4A47	FAM20A	NAP1L2		KCNH1	AIF1
C6orf201	PHYHD1	ARHGAP9		TMEM271	ANXA3	CREG2	C1orf146	MIR1251		SLC27A6	AC008403.1
PHYHIPL	SNORD62A	ELMOD1		LRRC36	MAPT	ETNK2	PRKG1	ANKRD66		MMP19	KRT71
KLHDC7A	C19orf85	LHFPL5		STPG2	PSPN	TAC4	MRVI1	PRPH2		RENBP	CORT
SRD5A2	KLK12	TCTEX1D4		OPN3	ETNPPL	THEMIS2	FAM174B	FCRLB		PLEKHA4	KRTAP11-1
HIST1H2BE	PLVAP	RADIL		SEMA4F	CCL28	LRRTM1	CALR3	SIDT1		DOCK2	PRR22
C20orf204	WFDC2	EYA2		KIRREL3	PDPN	CAPN12	LY6G6F	FEZF1		PIGR	CRABP1
RBP4	RNU6-384P	ANKS6		C1orf146	GHRL	CD248	KISS1R	PRDM5		DUOX2	SLC38A5
CCDC196	EPHX4	NCMAP		ZNF697	RAB3B	CCL5	NUP210L	FBXO43		PRSS35	RHOH
GCM1	DCLK1	DCLK1		TMEM108	PTPRT	HCN3	TMEM74B	HPSE2		HMCN2	OTOA
NR2E3	NHSL2	SLC7A3		S1PR1	GASK1B	ATP1B2	SLAMF9	SOX11		HIPK4	CYTH4
AZGP1	RBM24	ACYP2		ASTN1	MKRN2OS	KRT82	CDK14	RASL12		DNAJB7	MYOM2
DLK1	ADAM22	FNDC1		CDX2	TRPM1	SAXO1	RWDD2A	KCNS2		ANK1	SPAG8
H1FOO	HIST1H2BG	CYP1A1		DYRK4	RNU6-1280P	PCP4L1	BVES	PCDH8		EBF1	ADAM23
UPK1B	TSPAN12	SHCBP1L		LIN28A	EID2	TNFRSF11B	IFITM5	KSR2		ATP2A3	NRP2
SHISA6	NPB	LBP		CHN1	MYH10	B3GNT6	GUCA1B	NELL2		DNAH11	JAM3
OAZ3	SYT7	IL27RA		MIR345	SYT1	CYP26A1	THY1	PPP1R14D		CLDN15	SLC26A1
PCDHGA12	CCR9	KCNK10		GP5	P2RX3	B3GNT4	C21orf62	FRMPD4		ZC4H2	AC093525.2
S100B	NEURL2	DENND3		TBX4	TMEM88B	TTC36	SPATA20	OPRD1		CACNA2D3	CPLX1
DAGLA	EDN2	CTXND1		GGT7	CD19	XK	GDAP1L1	SMARCA1		FST	HEPACAM2
FCER2	ATP1B2	FSTL1		POU4F3	SLC12A8	LRRC71	AC004233.2	CHP2		PTPRM	MPP3
FAM13C	SPRY3	EMCN		CFAP97D1	FMO2	MGP	GDPD3	HECW1		GPM6B	RAC2
KRT18	SPACA1	GNG3		SAMD13	PLA2G4C	RP1L1	TMEM59L	SELP		SLC18A2	GRM5

PRRX2	YPEL4	SLIT3		HNF1B	RPS6KA2	SCGN	KCNA1	ACP7		NECTIN3	SLC2A13
HOXC4	CDH22	ANKDD1A		GJD2	ABHD18	PCDH10	ADAMTS8	SNPH		SLC41A3	ATP13A5
PRR36	GABBR2	GPRC5A		TBXA2R	RCSD1	OLFM4	EFHD1	KLRD1		OTOF	WFDC12
GABRB1	CP	RAMP1		BEAN1	USP50	CDH7	TNFSF15	AK9		SPSB4	CNGB1
CACNA1C	LARS2	SPARCL1		GNRH1	HOXD3	ASPHD2	CATSPERZ	RUNX1T1		MIR7-1	DOCK10
HACD4	CYSTM1	ANK2		GAST	GUCY1A1	ROBO3	LTF	PCSK1		CES5A	CCNJL
OPRD1	RFTN1	PLIN4		SLC10A2	SLCO1C1	DHRS7C	PNMA2	ST6GALNAC4		SEMA3G	CD248
CCN2	ISG15	LANCL3		HTR3A	HPSE	ZDHHC22	MRAP	GABRA4		OPN3	ZEB1
LTBP2	FYB2	ERG		GPR26	OR52B6	SCN9A	RN7SKP11	NRXN3		ANKRD40CL	ADAMTS19
F2	ZFP37	CMKLR1		TSBP1	PLXNA4	SNORA17B	TMPRSS5	RPL7A		MSH5	CCDC24
ADORA1	GGN	CMPK2		CLDN9	NCKAP1L	TNR	GLDN	ARHGAP15		KIAA1324	PLCB2
ITGB1BP2	CDC42EP2	APOA2		AC138647.1	PRAF2	MIR200A	PIH1D2	ASPHD1		SNTG2	RASGRP4
TOX3	ALPL	C3orf52		NLRP3	PACRG	NPPA	PROCA1	SLC6A16		GPR183	PEAR1
DCDC2B	GZMM	ABAT		FBXO16	OPRL1	SEMA6A	HTR2A	NXPE4		RASAL1	DOK5
PKN1	MME	NT5E		ICA1L	ITGAX	PCDHB6	RIMKLB	MYBPC3		SLC23A3	SAPCD1
DIPK1C	ARMCX4	DOC2B		SPRY4	SPRR4	SMPD3	TRIM17	SP8		HSH2D	TCAP
CADM3	OBSCN	SCARF1		IGSF9B	DCLK2	GRIN3B	TRPM6	HSD17B14		RPL7A	IMPG2
LHFPL6	PDZK1	PEG3		CD200	MYBPC1	C19orf85	METTL21C	WDR86		ZNF583	SOD3
DPYSL5	CFAP69	ADCY1		NPC1L1	TMEM51	NPAS3	PRTN3	TNFRSF13C		TENM3	KCNMA1
BEND4	SNORA2C	MMP11		FKBP14	CCDC87	RBM11	STYK1	FAM237B		OAS2	NHLH1
CEP295NL	CFAP100	TRPM2		NAP1L3	RTBDN	ROBO4	PTPRC	ST6GALNAC5		CCT6B	HCAR1
SLC25A43	WFDC5	MRGPRE		PRDM1	GRM7	RNU6-929P	CMA1	BICD1		FGF1	RNU6-1044P
LYVE1	ZNF648	CLDN8		SPATS2L	ANKRD34A	TEX52	C4orf48	MSLNL		CCDC106	SNORA53
PRKAR1B	LYZL4	DMTN		ARHGAP44	DPYS	IL2RB	NPS	DLX6		CAPN8	TRIM46
HSD17B8	MIR200A	TRPC4		TSPAN12	DGKI	CLEC14A	ZFP57	EPHA10		CNIH3	PNCK
TMPRSS9	MUSK	CYP27A1		BHLHE22	COX7A1	SHANK3	PWWP3B	LTA		RSPH4A	SFRP2
C17orf97	HS3ST2	ABI3BP		GRM1	GCK	PRAM1	ST6GALNAC4	VEGFC		EML1	KRT27
MAGIX	NCF1	NHSL2		MAOB	SATB2	C1orf54	CRACR2A	ALPK2		SERTM2	KCNN4
RIPOR2	AGBL2	COL5A2		GATA6	TMEM198	SDR42E2	KHDRBS3	ZSWIM5		PTPRU	TNFSF13B
STRIP2	HIC1	C1QTNF6		PTHLH	MS4A10	SLC30A8	SLC25A18	CCKAR		STKLD1	LY6H
PLA2G4B	ACAP1	SLC1A2		SLC43A2	CELF4	HDC	CD101	ALK		AIPL1	MYH15
RAB36	AIF1L	FEZ1		ZNF77	NHLRC4	NKD2	SHC3	TMEM171		SULT4A1	ZNF831
CYP27B1	OCA2	FBXL16		KRT23	DDR2	PTPRQ	CASC1	MAP3K15		COL6A3	SPACA4

MAPK15	RARB	CATSPER3		SOX9	FKBP6	NAPSA	EMX2	HEPACAM		MROH8	CASS4
CAPN6	CADM4	ZNF365		SEMA3E	AMBP	ZDBF2	CNTFR	RAB39A		SLC35D3	HAPLN4
CRYBA4	RGS16	HSD17B13		LRAT	RGS9	NTN1	IFFO1	KCNQ5		CMYA5	BTBD16
SLC6A13	ABCA4	B3GNT7		OLFML2A	ACKR1	BASP1	SLC28A3	C1QL1		FNDC7	PROKR2
GUCY1A1	CTHRC1	CD27		PRR5	AKAP12	CGREF1	LIPH	OAS2		PIP5KL1	A2M
COL25A1	FAM83E	FBXO16		ALPK3	DNAI2	KANK4	PTPRD	EGR2		SPATA20	CYS1
SLC9B2	GMFG	TTC9		TLR3	DAB1	NID1	ADAM11	C17orf64		CASKIN1	NPAS4
DMBX1	NEK11	RNY3		EGR4	NEXN	ZBTB32	GPR141	CD8A		TRIQK	ELAVL4
ZMAT1	PCDHGA5	DENND2A		LPAR3	SNORD98	CLDN2	SLC38A1	SPOCK1		SOSTDC1	UBQLNL
CD72	TMPRSS6	TBX1		WNT11	FAM89B	SLFN5	NIM1K	AJAP1		SPATA33	SKOR2
SAG	PIK3AP1	DNAI2		ACTN3	ABCG4	TOMM20L	GRID2IP	TMPRSS6		FES	MIR708
BRMS1	GRID2IP	PLIN1		NEURL3	LRRC26	ADGRF5	PTPRT	DSG4		COL8A1	PRMT8
HDC	DNALI1	TREX2		FNDC1	CGREF1	AEBP1	MED12L	BCAS1		FER1L6	SLC5A2
EDNRB	FGF14	CFAP77		RF01976	BMP4	EQTN	LRP8	MMEL1		GFRA2	SLC24A1
TSNAXIP1	IZUMO1	STMN2		AC020613.1	CD84	CRTAM	LCK	CD40		PDLIM4	NR5A1
HES7	PCDHGB2	UBA7		MAP3K21	CPNE4	SELPLG	GPR22	UTS2		SLIRP	FAM71D
TRABD2B	PLAGL1	AP3B2		ADGRL2	NECTIN3	PCLO	C1QA	IQCA1		C2orf40	FEZF1
DIPK1B	ZNF593	SIGLEC1		HMCN1	SLC1A3	CBFA2T3	EBI3	ASTN2		TEX45	PRDM5
AKAP6	GAL3ST3	MUC17		TGM2	AOC3	KIRREL2	FOSL1	GAD1		PODXL2	FBXO43
DLEC1	HIST1H1B	CHST13		SMOC1	C21orf62	ADAMTS13	AC139530.1	MYRF		PRRX1	HPSE2
FAM149A	CD164L2	RUNX2		NUDT15	CEP295NL	TNFRSF13B	TMEM25	THEGL		MIR193B	CCDC146
C11orf91	LRRC24	FGF1		AC073111.5	ALOX15	ASB15	GASK1A	ASIC2		IQCH	TBX4
C16orf96	ATP13A5	RTN4RL1		GEM	ADARB2	PAPPA2	RNU6-1044P	PLLP		GRID2IP	CEND1
SLC41A3	TMEM179	SNORD42B		TOX3	GRIP2	STKLD1	KPRP	NKAIN3		CHST2	ACTG2
RBPMS	SHANK2	PCDHGB2		SUSD3	NGF	OTOF	NKG7	GPR88		KRT12	KIAA0319
CORO1A	MGP	TENM3		AMOT	C17orf64	CCDC190	TRIM66	DPEP3		SYNE3	RP1
TMEM255A	AMDHD1	APC2		DAB2	RASGEF1A	FAM155B	CCDC69	SHOX2		GCNT7	UBE2U
PROZ	ELAVL2	C2orf88		FSD1L	INSYN2	NAV3	TEX54	FGF21		PECAM1	MC2R
NCAM1	S1PR4	DAGLA		PDE5A	SCN4B	SPACA3	KBTBD13	FBXO15		STAP1	RNU6-120P
AC011529.1	IQCG	DNAH2		CFAP69	SLC51A	SIX6	PLEKHA4	SLC15A5		KCNA1	PRRT1B
CMTM3	HSD17B2	TNFSF12		FBLIM1	MAJIN	CRHBP	SNORA58B	RNU12		PJVK	NOL4
TAGLN	UBD	GPRC5B		STARD8	HEATR9	GALR1	CMYA5	NPAS4		ITGA1	SYCP2
TGM7	ADCY4	ADAMTS5		COL14A1	AC118754.1	SCGB1A1	CX3CR1	TBX4		SSPN	KIF19
TBC1D9	KCNIP3	COL5A3		RHBDL1	GAD1	PLAC8	CD7	SEZ6L		SIAH3	CPB1

TUBB4A	HSPA12B	CDH11		FZD7	DEPDC1	ZSWIM2	RUNX3	SPOCD1		NWD2	VTN
GPR183	STAP1	B4GALNT2		TMEM63C	IGFBP3	CLDN14	GRM7	POU4F1		AC011529.1	PRG3
SERPINF2	HSD11B1	GRM1		GRIN2B	HYKK	OR8S1	MIR193B	DPP6		GUCY1A2	TMPRSS5
C19orf67	TNFSF10	TGM5		REP15	FGL1	SCGB3A1	PLCXD3	NOXO1		CD27	GPR45
KIAA1324L	RNF128	RBP4		AK7	RPRML	WFDC2	PHYHIPL	WSCD2		CAPN6	TLR1
CYP27A1	GFRA4	MN1		GRIK1	FIGN	SULF1	ADAM12	RRAGB		INHBA	MOGAT2
LRRC27	SDCBP2	LTA		ACE	DENND2A	FBXW10	UBASH3A	AKAP6		KLHL13	TRIM38
ENPP5	KSR2	EPHX4		KCNJ10	KCNT1	LINGO3	SCAMP4	OLFML2B		FAM13C	VXN
DNAH2	SNORA14B	SPRY4		SLC24A4	ITLN1	GDF11	CAGE1	HRNR		ILK	SOX2
DNHD1	PKP2	RNU6-622P		TNFSF10	SLC5A5	CDHR1	DMBT1	CD86		RAI2	RN7SKP204
ADAMTSL3	PRKCQ	LRRC34		CLIP3	TSPAN33	AIPL1	SCN3A	RIPOR2		CFAP77	TMEM200C
MSI1	HEATR9	RNF222		NPR2	SH2D4B	C20orf173	PPP1R27	INSYN1		PLA2G4C	CALY
WFIKKN2	BCHE	SNORA58B		NDP	CD38	COMMD5	ZFPM2	AC021072.1		COL11A2	SEMA6D
EGFLAM	KRT26	COLEC11		LHFPL2	SHANK3	CD38	MYO1F	GRIN1		RGL1	LBX2
GGT5	ATP6V1B1	SMPD3		ATP10A	QRICH2	FFAR2	ATP1A2	HGFAC		HEATR4	FLT4
TAL2	EAF2	CGNL1		CLEC3B	IFIT2	RASGRF2	KDM5D	EBF1		SKAP1	TSKS
BIN2	DNAH11	ZC3H12D		BTN3A1	FGF16	ACYP2	LAPTM5	KCND2		SYTL3	DKKL1
ODF3L1	TSPAN33	GSPT2		ISL1	MT-ND3	NEFH	FKBP14	CLIC5		FBXL13	IGF2BP2
OPN3	KLHL32	CCDC89		ZNF365	KLHDC9	KATNAL2	MMP21	CD36		VSNL1	FAM155A
TMEM25	GCHFR	MYH11		SPINK6	LRG1	ASIC3	CTSK	CSRNP3		RF00602	LINGO4
GNG5	LAMA4	ARID3B		CHRM4	SLC18A3	GUCY1A1	GPR6	ADGRL3		PCDHGB2	EDAR
C19orf57	MIR365A	RHPN1		FOXC1	C3orf18	OTOG	ZIC3	KRT9		DNAJC12	PP2D1
ABCD1	MECOM	MTFP1		IRX1	SLC17A9	RXRG	ICA1L	SLC10A1		SULF2	RIPOR2
AGR2	DOCK10	SPAG8		COL5A2	MAP9	ANKRD1	ZNF618	CPXM1		STRA6	PRCD
DNAI1	RIBC2	CSRP2		INHBB	NPR3	CHRNA6	ADRA1D	RUNX2		FBXL2	OGN
CHRNA3	CACNA1I	SSC5D		SNORA2C	ST18	SLC6A5	FEZF2	IL16		VSIG8	Z98752.3
CAPN12	HOXD1	DNAH10		SHCBP1L	LSP1	GPR119	LY6H	ADAMTSL1		ZIC5	EPHX4
RNF152	PLEKHG1	CCDC69		RGS20	SLC16A3	GJD2	LIN7A	NDP		FMNL1	CD40
PPEF2	NYX	ARG1		PLIN4	TSSK1B	COLCA2	ALOX15B	LDB3		NEURL1	CYTIP
RAB2B	CDH5	NRIP3		OTOP3	CCDC73	RNU6-931P	KRT35	KRT19		EFHB	OBSCN
PRSS35	CTSS	TRIM9		FBXO27	SP6	PPARG	RORB	HSPA12B		RELN	AGR3
SCARF2	C11orf65	BMP6		LGI3	MIPOL1	KCNQ1	LARS2	KIAA1324L		CD5	FBN2
CAMK2N2	MMP13	EPB41L2		KRT80	S100G	RNF112	COL3A1	IGF2BP1		MYO1H	ENPP6

C18orf54	TIMP1	ALDH3B1		PDLIM3	SPTBN4	ARAP3	AKAP5	RASGRP4		INHBB	BRINP3
CCDC33	ACSBG2	LRFN3		ODF3B	PAX8	TNFSF11	SERPINA5	EREG		EHF	FAM89B
DBN1	NUGGC	SNORD63		ABI3BP	SULF1	CFAP70	MIR221	MFAP2		HIST2H4A	LBP
CUX2	RTL9	MYL9		ARMCX6	PDZD3	PLVAP	THRSP	TEX49		AQP3	NOXO1
A3GALT2	GPR25	NRXN1		FGF22	SLC4A5	HSPB9	HPSE	RNY3		CACNA1G	IL31RA
SERPINC1	CD83	SERPINA12		CHADL	AMHR2	PECAM1		HMCN1		FKBP10	CXorf21
FAM19A5	CCDC87	JAM2		HRASLS	KLK13	NNMT		KLK13		SACS	ARG1
CASC1	TRIM66	PTPRM		HTR1B	NCAM1	MAP3K19		SOX10		LCA5	PTPRN
PSORS1C2	SCUBE1	STRA6		PDF	IGFBP2	DES		DYNC1I1		KCNH5	PHKG1
DACH1	IL1RAPL1	FAXC		KIRREL1	MROH6	FSTL5		CHST2		TOMM6	RRAGB
ANKRD33B	RIMS3	EDN1		TNFRSF11B	GPR137C	SPATC1		ADCY1		ARHGEF40	FSTL1
C3orf18	AC021072.1	NPTX1		ARHGAP28	SLC30A2	RNU6-622P		TMCC2		VPS25	ITGAE
KLHL3	GNGT2	PLPP1		PDGFRA	ZFHX3	CD5L		RNF180		TBXAS1	CCDC89
LMCD1	TECTA	ULK4		NTRK2	FAM19A5	ECE2		APOLD1		ARHGEF2	SLC34A2
MMRN2	CLDN15	IMPG2		NEXMIF	SH3TC1	MIR98		LIPN		STPG3	SNORD62A
SMIM1	HIST1H2BD	TET1		LIPC	CNNM1	OR52W1		SLC4A5		SNCG	NCF2
SCNN1G	PCNX2	DLX6		FGF1	LCP2	PCDHA1		NPPC		LPAR3	CNN1
RNU6-1299P	B4GALT6	HIST1H4L		TMEM238L	PTPRD	DPEP2NB		IYD		EGFL7	F8
PLEKHG4	AC005551.1	MYO15B		CH25H	C1QA	NMBR		SPTBN4		SBK3	CRACR2A
FAM217B	C4orf48	KCNS1		SYNE4	SLC1A6	FOXI3		PCP4L1		FAM186B	FREM3
PTPN18	LCK	KRT79		ADAM22	SLC2A13	NTSR2		SERPINA9		SNORD35A	TRIB2
GRAMD1B	CACNB2	CCL2		SSTR4	TNNC1	TGM2		CASQ2		PTGDR	RHAG
CIITA	SLC5A8	OPRD1		FAM171B	MLPH	RND1		AANAT		RTN4R	ROR2
CSRP2	ZNF449	ETV2		LHX2	TMEM100	NCAM1		IL2		TGIF2	FOXF1
ARHGEF25	AQP5	KRT18		SLIT3	CASKIN1	SBK3		ROPN1L		DCST2	GPR151
DMTN	DUSP13	PECAM1		CD7	SLC7A11	PI15		ST8SIA3		GABRB1	MEF2B
LAT2	PTPRN2	SETBP1		TSPAN13	ARHGAP22	SCN4B		GPR149		PDE7B	CFAP299
GNPNAT1	SERPINI1	KLHL41		CPT1C	RNF180	SLIRP		GABRA5		PIK3AP1	CYP27B1
CDH23	OPN1SW	DNAH9		SGMS2	CELF2	FAM83A		HDC		FNDC4	SCHIP1
LHX2	SHISA8	FAM13C		NANP	LTA	PRR22		PTGDR		FGFR1	TNFRSF1B
INVS	LOXL3	AVPR1A		SLC35G2	CALR3	KLHL6		USP44		BGN	ZFP57
HEATR4	EFHD1	FADS2		FER1L5	AKNA	NPHS1		LUM		ZNF593	TLR9
PLA2G3	TNFRSF11A	TSPAN33		C18orf25	RIPOR2	IL13RA2		ZNF582		HTR2B	HRNR

APOLD1	BMP3	GFAP		TRPM6	TMEM269	NPTX2		SHOC1		AADACL3	KCNS1
POU4F1	RAD51AP2	KRTAP11-1		FNDC4	LAMA4	WNT11		CYP27A1		ADGRE1	C19orf71
RPS6KL1	PCP4L1	MYOM2		GNG3	CACNA1A	CARMIL2		RAB3IL1		KRT7	RNU6-750P
AMIGO2	CFAP126	PRUNE2		PTGER4	SPSB4	FNDC1		EPSTI1		TRAF3IP3	GFRA3
ARC	SYTL2	CD93		FXYD6	ANKRD53	RARB		SPATA21		SPINK2	ADGRG3
COL27A1	DNAH3	GPRC5C		ARHGEF17	FOXF2	SIX2		SALL1		GSAP	TMPRSS11A
FSTL1	TSGA10	EVL		AGAP2	RNF32	MYLK		ADCY10		SAT2	SLC44A3
PLAG1	PRKAG3	RARRES2		TNF	ASIC2	HCST		TMC3		PCDHGA2	FOXS1
RALGPS1	MYRIP	PRKAR1B		MARK1	GPR68	PLXNC1		LPL		AGER	ARHGAP30
SPIN4	GRIN3B	TMEM151A		CCL7	BRSK2	GLI1		RBPMS2		RILPL2	TRIM67
CYGB	FOXC2	RNF144A		ZNF853	FOXS1	CASKIN1		CD19		PRR16	AQP5
NPR2	C7orf31	STAB2		EMILIN3	PRR15L	FAM3B		BASP1		GRAP2	EPOR
MRVI1	CLDN23	VCAN		AEBP1	QPCT	ETNPPL		C19orf81		AK5	EPHA10
SELENOM	AK7	CLVS1		LAMA2	KCNE4	CHADL		EPHA6		KLHL3	PHLDA1
COL4A1	ANKDD1A	SELENOM		CRYBA4	S100A8	TEX47		LY9		TMEM26	KCNH4
CHIC1	SRPX	CHODL		PIK3CG	CMPK2	CA3		SIM1		GPRIN3	KCNJ9
SLC18A2	ARMH1	FERMT2		GIMAP5	NCF2	TTN		RAG1		P2RX7	MILR1
MAK	ITGA1	MEF2B		MSRB3	PKDCC	HEYL		ALLC		ANKRD53	GPR173
RUNX2	SNORD71	KRT17		MYBPC2	TUBB4A	PCARE		CHGB		PYGM	ADGRA2
ZC4H2	STX1A	COL4A2		NES	GPM6A	TCTEX1D4		CDH10		SPOCD1	RNF17
RAB33A	IL10RA	C19orf66		INTU	RHOC	PIP5KL1		RNF186		HSF5	GSPT2
TCHHL1	GHRL	ENPP5		PEG3	C10orf95	SST		RNA5SP194		ZNF189	DLEC1
CYP8B1	CAPN3	AGXT		SLC10A1	MGARP	SNAI3		HIST1H2BE		TLE6	HACD1
COMMD5	GAREM2	VAMP5		KIF26B	PRIMA1	ST6GALNAC1		TEX22		SLC7A8	CLSTN3
THSD1	PGM5	HEATR4		RGS4	DPF3	GIP		CALCOCO2		MSH4	SUSD4
ZNF879	CAMK4	GDAP1L1		SMPDL3B	TTC25	IL10		DNAH12		SLC12A5	FADS3
PCDHGA9	DMBT1	EFCAB5		P4HTM	NOXO1	PMFBP1		C12orf42		C1QA	TEX14
SLFNL1	TRPC4	MSRB3		PPP1R3C	MLKL	CDH16		MTNR1B		CDH15	PIK3R5
ZKSCAN2	TSGA13	SYT1		CPA2	TTC7B	TPSG1		MIR15A		GALR3	EAF2
AC138647.1	IL5	USP43		EFEMP2	LRRC46	LRIT2		RNU6-842P		GLIS1	GRIN3A
KLHDC9	PRSS27	FLNC		ZAP70	ALDOA	RNU6-105P		AC119396.1		CUL9	SLC26A8
PPFIA4	RBM20	DLG4		PIEZO2	CARMIL2	ERICH6		ANGPT4		NES	TNN
MYLK3	RILP	RAB37		RAB39A	ITGB7	RN7SKP13		GRIN2B		NFASC	PFN4
ADAMTSL1	MFNG	KRT77		SYT2	SLC4A4	GRASP		SLC4A4		ADGRF5	CUBN

COL4A2	DPP10	C9		LIN7B	F2	ENO2		ECM2		GPR63	HLA-DOB
QRFP	ARHGAP15	ST6GALNAC2		RAB19		PRR15L		OXTR		DNAH3	RUNX3
ATP7B	TMEM88B	LIPN		ARTN		SLIT1		KCNC4		KALRN	OSBPL10
BST1	WDR49	RF00602		C2CD4C		ANKS6		PARVG		MEIOC	SLC6A17
ERFE	PTH2	HNF1B		GPX2		ANKRD33B		MYOC		C2orf74	FAM161B
GADL1	ZNF287	ARHGAP44		PTGDR		TSNAXIP1		PCLO		ALX4	TREX2
SHC3	TEX45	CD72		TP53TG5		MCTP1		SLC38A4		CLEC7A	HCN2
NUP210L	SGCG	OLFML2B		FLRT2		TMOD2		FSD2		RNU6-1304P	FOXF2
USHBP1	CMYA5	SVOPL		LRRC24		GJD3		STX19		IL10	SNORD42B
KRTAP16-1	TMEM229B	TIMP2		ESYT3		DUSP4		CPNE9		PDCD1LG2	ESPNL
LDLRAD1	AADACL3	PRSS35		FBLN5		LGI3		CA7		CPSF4L	CCDC159
PPP4R4		LGI3		ST8SIA4		PRCD		RUNX1		ENPP2	DHRS9
PYGM		KCTD11		ISL2		AMPD1		ADGRB1		SNORD17	IL1B
TMEM240		FOXS1		EVL		ARTN		TCFL5		PDE6B	TMEM173
TGM5		CXCL9		NTRK3		SLC26A8		PCSK5		NIPAL1	LTB
CHRM1		TMEM262		AMN		TMEM88B		RYR2		CCBE1	WNT9A
NLRP3		IL19		GPR173		OAS3		SLC14A2		PPP1R3D	RF02160
PCSK1		KCNC2		CFAP74		PDF		MYOZ1		GHRL	CLEC4A
ZNF239		KLHL3		JPH3		SHISA2		HOXD10		LURAP1L	CTSW
JAZF1		PRR18		CGNL1		PHKG1		SULF1		FKBP1B	NKAIN1
CAMK2N1		ADAMTS7		CXCL9		LIPC		FAM131C		ANXA9	DND1
AFF2		CHRM5		PHLDA1		KIF17		WFDC2		CCDC30	C2CD4D
WDR66		BEAN1		TIE1		PRRT3		GJC1		DLX1	CPQ
NEU2		CNTF		AC011529.1		SLIT3		CNN1		ATP6V1C2	CITED1
ANKHD1		NANP		STK36		SH3RF3		GPAT3		XK	ADAD2
MROH8		MIR106B		WNT1		PP2D1		FAT4		TRAF1	PTPRC
ARHGAP44		BLNK		HIST1H4B		BAIAP2L2		C3orf80		C17orf98	S100Z
SLC2A13		RHOC		APOD		CCNA1		MEST		SPX	RNU4-89P
HSPB2		EGR2		SOSTDC1		AWAT1		PRDM1		ARHGAP6	LRRD1
ELN		ECM2		SELENOP		PRRT1B		CCN2		RIBC1	CAPN11
GULP1		SPON1		EGFL6		AGAP2		MPPED2		EFNB3	MDGA2
MANEAL		SCRN1		MMP21		ARHGEF6		ARAP3		ZNF786	BCL2L15
AWAT2		CD37		DOC2B		SH2D4B		PAX3		GREB1L	C18orf54
ITGB8		PRSS12		GREM1		LBP		SLCO2B1		CEP295NL	PRSS12
SVEP1		SOX9		PLCH1		RELL2		TSPAN2		JAZF1	ABAT

AEBP1		PCDHGC5		UROC1		FAM89B		AFF2		ARL9	IKZF3
PTGDR		ARC		UBA7		P4HTM		ETNK2		STYXL1	HDC
LRMDA		BIK		HHIPL1		DIRAS1		SLC7A14		TOX	SNORD53
KCNA7		APOBEC3H		ADAMTS20		AOAH		MPP3		GPR156	PI16
CSF2RA		SEMA6A		PSMB8		PPP1R1C		POU2F2		SAMD12	LRRTM2
ABI3		PDZRN3		DDAH2		ZNF385C		ZIC1		ADAMTS15	CYBB
C1QTNF6		CNN1		BCO2		GRIN2C		SNORD63B		SLFN5	SYBU
ZNF784		TBX2		SLPI		NR1I2		PREX1		CMTM3	CCL11
ANKS1B		PCDHB7		MEIG1		TECTB		MAGIX		NEK2	ZC3H12B
ADAMTS17		EQTN		ACTL7A		GDF3		SLC38A1		KBTBD4	DERL3
CNTN2		HERC6		ADCY7		DRD2		FAM57B		KCNB1	LST1
STMN2		PLCL2		CTSZ		GOT1L1		RSPH4A		TRPV2	OR10V1
STK36		GRB14		RIMS2		KIF2B		UBXN10		THEMIS2	INPP5D
DAB2		RUNX1		PLAG1		CXCR1		CIDEA		PCDH18	ARSJ
ARMCX6		GPSM1		SLITRK3		TEX48		EBF3		KLHL10	KLHL38
IL17RD		CCDC148		SNORD117		CCDC153		PAPPA		TNFSF13	SLC39A4
RAMP2		HSD17B11		ARL11		OR2A12		COL28A1		ITGA4	KITLG
RTKN2		PALM		CIB3		RN7SL645P		FAXC		KCNA2	NXNL2
CELF3		DDX4		WDR17		SPRN		HOXB1		OOEP	KIAA1755
STC1		TEX14		RIMS1		OSR1		GLB1L2		SLC16A12	TNFRSF11B
DNAJC6		PABPC4L		CCIN		CCDC103		PI15		KANK2	TBC1D30
FYN		GLRB		KIAA0319		SLC15A3		FST		GPRC5C	KIT
HRH2		AC011529.1		HIST1H2BE		LYZL4		SCARNA1		METTL21C	LRCOL1
CDH11		SLC15A1		ANXA10		IGSF10		SAMD12		ZCCHC3	BAAT
STRA6		AC118754.1		CHGA		SLC10A5		INCA1		ARC	PLOD2
TMEM253		AC015802.6		PRPH2		RNU4-2		TMEM229A		FAM189B	NOTUM
TNFRSF11B		GLI1		PRDM5		TMEM173		PRRT4		RFTN1	DMRTC2
SCNN1B		EPHB2		GATM		RSKR		CCL11		XRRA1	MRLN
RNF17		ADORA2A		DHRS7C		HSD17B8		SLC9A5		ARHGAP45	TMEM238L
ST3GAL1		CALHM5		NNMT		MYL9		CRIP3		NHSL2	WIPF1
PTPRB		FOXF1		RNU6-105P		KIF6		GASK1A		PDLIM7	PGR
WFDC12		NEIL2		RF02187		GRIP2		NAV3		FLNC	UBASH3A
JAKMIP2		ACTL9		TRIML1		HES7		TAGLN		CASC1	AMPD1
EPGN		ADGRB1		NKX1-2		SATB2		TNFRSF13B		ERICH5	FAM169A
ZHX1		DPP6		BTN2A2		CCNO		FABP7		ELAVL2	NKPD1
COL5A2		PCDHB2		GJA5		P2RX6		GXYLT2		EME1	SNORD63B

PI16		MIR221		KL		PIP5K1B		DNM1		MIR194-1	SPNS3
DSG4		STK32A		MIR10B		EMP3		PRKAG3		CATSPERD	SPRY3
NOS3		LBH		LEMD1		SLC39A5		RNU6-431P		AARSD1	SYT8
ENO2		RELN		RF00413		SMAD6		MYLK		CCSER1	INSYN1
REM2		CXCL12		HPGDS		RPL3L		FLT3		ALAS2	CEP126
CCDC69		RAB26		TPO		ARHGAP6		NR2E1		SNORD55	P2RX2
KCNG4		GASK1A		HOXA2		ALDH1A3		SPATC1		IQGAP2	RAB44
PTPRN		SDK2		CHP2		NELL1		MGAT3		PI15	BATF2
DUSP18		FST		FYN		AMIGO2		PLEK		FN1	CYP21A2
DUSP10		RGS20		MYT1		COLEC11		LRRC46		FEZ1	HAVCR2
HGD		ANKRD60		CHST10		GSPT2		MMRN2		PCBD1	TNIP3
METRN		PLCD4		LINGO2		GNGT2		IL2RB		ADAMTS17	C1orf115
FAM187B		KLHDC8A		KCTD4		SLC2A13		ONECUT2		TIGD4	TBX6
FBLN2		EPS8		BCL2L14		CALHM5		NCF2		RAB33A	CYSRT1
SPOCD1		STKLD1		HIST1H4D		IL1F10		PCDH9		HHIPL1	STX1B
NFE2		OLFM2		CIITA		ZEB1		RF02160		GNG7	FSD1
PENK		MERTK		ST6GALNAC2		TGIF2		TCERG1L		REEP2	TEX101
KIF6		FNDC7		NME5		LRFN3		LHFPL5		TRDC	SGCD
SPON1		ILDR1		PSTPIP1		MYOM1		FBP1		KIAA1614	ENTPD3
ADRA2A		SHISA8		COL8A2		IMPG2		PADI1		SH2B2	RAB3B
SELPLG		TSPAN32		ITGB8		ANKRD53		EYA1		RET	SLC4A4
PROX2		RBPMS		HEG1		AOC3		RSPH9		IGSF10	PDE6A
PTH1R		CCDC88B		ADCY1		VXN		FAM3B		SAPCD2	SLC7A11
MERTK		FBLIM1		CLEC6A		FKBP10		CXXC4		UNC80	CHST1
BGN		AGMAT		THSD1		SEZ6L2		UBD		SPOCK2	SH3BGR
EPHB1		RNU6-494P		CNTN2		HIST1H4L		PCOLCE2		MMEL1	RSKR
STYK1		ANKRD40CL		PLPP1		TBKBP1		PDE6A		WFIKKN2	BPIFC
RASD1		HOXC9		KCNJ14		MYLK3		CSMD3		GREM1	PARVG
NEUROG3		ARHGAP28		SH3TC2		TMEM198		BRSK1		CXCL12	COLGALT2
CCN3		CCDC187		PRKAR1B		GSTM2		SSC5D		SETBP1	PCLO
ADGRL3		ELN		ATP6V1B1		FERMT2		KLHL32		EBI3	4-Sep
PLXND1		RNF207		STBD1		MEF2B		RAB42		PCDH8	COLCA2
AMPD1		CEMIP		HID1		TRIB2		LOXL3		CHRNB3	C11orf96
TGFB1I1		RAP1GAP2		ANGPTL7		NOS3		HS3ST3A1		CDH7	AL121768.1
GRIN1		DNM3		KCNRG		CFAP299		SCARF1		CLVS2	JDP2
RTN4RL1		TMEM150C		APBB1		FAM227B		POLN		UBQLN3	HSPA1L

BEGAIN		HENMT1		AC124319.1		IGLON5		HOXD11		OR2A12	ZC3H12D
CCDC114		SHISA2		CDHR3		ADORA2A		PLA2G2C		HSPB7	NPS
ALS2CR12		MRLN		PDE6A		GLIS1		DNAH3		SLC17A1	PGLYRP3
ANGPT1		ACTL7A		CCR10		SCN5A		MEF2C		MCF2	LPL
APLN		DPYSL5		GSTM3		APOL6		MKRN2OS		CATSPERB	LRRC46
FBXO2		SCARNA7		CFAP70		SLC9A3R2		RBM11		EPX	KLK10
TMEM8A		KLK5		GPX3		GJB2		CFAP77		AL589666.1	STAC2
MEGF10		SLC40A1		VSNL1		PYGM		TTC16		PKD1L1	HSD17B8
HELZ2		RWDD2A		FAM78B		ABCC6		FOXF2		PROSER3	ITGAL
PLCXD1		CALML4		FAM171A2		ADM		KRT84		FYB2	TMEM45B
CRTAM		SCUBE3		HCK		EFHC1		CACNA1E		RUNX2	HORMAD2
ZC3H12D		RNF152		CYBRD1		LBH		TSPYL5		RPL36	ANGPT4
EDNRA		GSTM3		NEFH		MYBPHL		KANK4		SCML4	INSYN2
KIF27		CEP112		ADGRL3		PRDM8		PCDHB7		GRAMD1B	RPL36AL
GPR137C		DAPK2		ETV4		NOTUM		MIR27A		PIK3CD	NRAP
NGF		PAPPA		NRIP3		NEURL1		DPYD		TRIM71	PRR15
CHST8		SOGA1		NWD1		HENMT1		DACT1		ADD2	LINGO3
IQGAP2		GARNL3		AMIGO2		BGN		GPR34		CCDC18	CDK14
ARHGEF15		SAT2		CPA4		SH2D7		SERPIND1		NOVA1	ASPG
ADAMTS20		CELF3		ATOH8		CCDC154		NFAM1		CARD11	LENEP
KCNE4		MIR186		FZD3		PRG4		PRSS57		KIF21B	ROM1
GPRIN3		MAP3K21		LTBP1		PRR16		KRT24		NT5E	GPR137C
ARHGAP28		SLC18A2		TMEM88		IGF1		CYP46A1		P3H3	TSPAN2
DLG4		DMBX1		CLDN8		GPR68		GALNT12		MAP2	IFI44
FN3K		SNORA20		ANGPTL2		SERPINE1		GAB3		ZNF213	KLK7
RHO		CYP1B1		HECW1		CABP1		ZNF536		LHX2	HCN4
LOXL2		NODAL		ASTN2		TMEM178B		TNFRSF9		KIAA0895L	RN7SKP11
TIMP2		PANX2		SLC15A1		CHCHD10		CPQ		MARK1	SELENOM
COLEC12		KALRN		KRT28		INSYN2		ADAMTS9		ASPA	CNGA2
PCDHGC4		PROM1		AQP9		MYL6B		KRT35		TGFB3	RNU6-622P
HEG1		UTS2		TSLP		ENG		RASGEF1A		NTRK2	PNMT
USP35		HOXB1		KIT		DUSP18		SEMA6A		GAS7	PCDHB2
AARSD1		ARHGAP24		CMYA5		MKRN3		TERB1		ETV2	SNORD49A
REC114		RYR3		MYLK		PADI4		PRRT3		SLC25A2	TC2N
CYP2U1		MISP		BST2		KCNC3		SH3RF3		EFR3B	KCNC4
SDK2		NALCN		FOXI3		SYDE1		PCDH15		ADCY7	SLFNL1

LBH		C2orf92		SHD		UBXN11		SLC12A5		PSD2	SCARNA22
CHRNB1		BMF		PCDHB14		PLPPR2		TEKT5		WDR93	ARID3C
ABCB5		PLAUR		TGIF2		SCG3		KRT36		PGF	LCK
BMF		SCML4		CRIP3		H1FX		TSPAN13		GULP1	ZNF850
MAJIN		PGLYRP1		LRMDA		PLK3		IRX4		AZIN2	CA9
SLC18A1		CD248		IL34		NR1H3		C10orf62		MAP1B	PCDHGA5
SOX9		PIP5K1B		OGDHL		CHRNB1		CD80		STAB1	FLVCR2
C2orf88		ADAMTSL1		GNGT2		HUNK		STK36		CAMK2N2	MKRN3
GPC6		ATP6V1C2		PLCL2		MIR374B		TRIM6		WNT2B	CD300LB
PAQR8		PTGDR		OSBP2		SNORD10		PRR36		RPS6KL1	PYROXD2
NKD2		HSD11B2		ABLIM3		GNG7		LMOD2		MYOM1	IL10RA
GASK1B		RSPH4A		BRSK1		RNU6-133P		WNK3		CAMKMT	AKAP6
PCDHGA8		EPOR		SLC15A2		EPHA8		GFRA1		TRIB3	HOXA10
IRF4		ATP6V1B1		CLVS1		NAV1		KRT8		DGKG	HES7
ZFP30		SPINK5		PXDN		DIRAS2		RNF151		PKNOX2	RIMKLA
APOBEC1		NOXRED1		TMOD2		SHC4		PDZD3		IL1F10	TSPAN8
ENPP3		ABCB5		MPPED2		DACT2		INPP5D		RF01159	LIPG
SGCA		ALCAM		KCNH7		FKBP11		HGD		SOX9	RASAL3
NFE2L3		HTRA3		AGMO		NAALADL1		DCHS1		HPGD	BICD1
ACOT11		PLEKHG4		PCDHGB2		CC2D2B		CACNA1F		BIN1	FSD1L
SRRM4		RTKN2		FEZ1		TUBG2		ANGPT1		IL22RA1	TMEM25
DNAJC12		LRIG1		PALM		PCBP3		DCLK1		TIFA	CCR8
CA7		LINGO1		DCDC2B		NFIL3		DIPK1B		EHD3	GNG4
NFATC4		EDNRA		C7orf31		OSGIN1		WAS		CALCB	ZBTB46
MN1		GEM		SYT9		ZNF250		LYPD1		GJA3	MAGEE2
LIPH		TMTC1		MPIG6B		OTUD7A		FFAR2		KRT17	MESP1
NLGN2		ITIH5		TNFAIP2				APOBR		NOG	CIDEA
LRP2BP		TMEM121		GRIN3B				NAPSA		CDO1	KCNN2
ZNF521		NYAP1		TRIM6				TFCP2L1			HECTD2
PPM1J		GRIN3A		FSTL1				MED12L			CFAP100
ADCY1		RHPN2		SLC6A15				DSCAML1			CDKL3
MIGA1		GPR153		PDZD9				HOXC13			PRDM8
DDX4		NFE2L3		MEIS3				KCNQ2			C4orf19
SBSPON		APOBEC1		STX1A				UNC13C			AMOT
HIPK4		GPR173		HTRA4				SLC6A5			ARMC2
MYL7		CMTM8		TIMP2				SLC5A5			C1QTNF3

RASGRF1		NPB		DAPK2				GNAZ			NRXN1
ABI3BP		MESP1		SMIM24				TACR3			TMEM88
NT5E		C1orf158		CGN				MIGA1			HOXA4
IL7		TRIQK		TRPV1				IGSF10			SAG
CCL2		IGSF10		EPCAM				DTX1			ACTN3
BMP6		KRTAP7-1		COL4A1				MPO			GPAT3
LGALS12		RNU6-638P		PTPRK				LRRC4			HOXD10
SETBP1		DNAJB13		CMTM3				DNAH2			OIT3
PODXL		NPAS1		GPR135				GPX2			DIPK1B
TMEM98		TMEM100		FAM221B				TMEM151A			CCDC173
ITGB7		GPRIN1		PCDHB6				CRACR2A			MT-ND6
MYORG		CASQ2		SCRN1				AIPL1			PIH1D2
ADAMTSL4		LRP2BP		AD000864.1				TMPRSS7			RBM11
COL15A1		ADAMTSL4		RAD51AP2				RELN			ELF5
ITPRID1		UPP1		CCNO				ETNPPL			WIF1
C5orf49		CBLN3		NOS3				NKX2-1			FBXO48
MORN4		SCN5A		DIPK1B				CHGA			C9orf131
ARHGAP30		PTPRK		FGFRL1				TMEM132E			SRMS
SLPI		B3GNT3		SHROOM3				SLC17A6			TNFRSF13B
FSCN2		MARK1		DIXDC1				TBX18			SNORD45A
CEP112		IGFALS		PTGES				SYTL4			ANXA3
NKAIN1		SPATS2L		TET1				DPP10			IGFBP5
BCL6B		ZC4H2		COL6A1				LRP2BP			CD84
SNORD49A		TBKBP1		SYCE1L				HECTD2			USP50
GUCA1A		PLXNA4		MAPK11				NOSTRIN			SAMD9L
LY6G6D		SCARA5		P2RX6				PLCE1			SNORD98
YPEL2		EPCAM		MECOM				FOXE1			KLK6
FXYD6		FZD7		ARHGAP40				NCCRP1			ATP6V1B1
FAM189B		HES2		DBN1				GRIP2			PLA2G5
COL8A1		SCHIP1		MAP3K15				CPN1			TNNC1
GPAT3		WDR63		PCED1B				SYNJ2BP-COX16			OTOGL
C22orf23		TAGLN		SNORD53				OSBPL6			RNU6-638P
SOX18		SAMD12		TLR4				RHOH			RPS12
TLR4		TMEM252		DPP10				LRRTM1			HOXD9
MYH10		PRDM13		LRRC32				ACSM4			TSPAN12
NAALADL2		COL8A1		C11orf91				MPZ			GPR68

CTNND2		ANO4		FAM187B				MFAP4			CD53
SYDE2		RLBP1		ACSS1				DUSP13			POLN
TBX1		STBD1		EML1				SATB2			EMILIN3
PACSIN1		MIR7-1		XRRA1				KLK6			DACH2
CTRL		PCSK6		ATP1B1				GPR22			CHRM1
UPP1		WSCD2		TEK				CD248			RTN4RL2
THSD7A		AMIGO2		DLG4				SLC35F1			HRCT1
TSPAN2		SCARNA6		FERMT2				RNASE1			ELF3
KIF5A		TMEM200B		MIGA1				RILP			NXPE3
SLC25A23		SCUBE2		BLNK				CCR5			OPN1SW
KALRN		FBP1		COL4A2				SOSTDC1			P2RY2
SHROOM3		TM4SF1		AFF3				APOM			CAVIN2
NEFH		PCSK9		DNAH2				RHOF			EFCAB5
PYROXD2		S100B		PTPRN2				DIRAS1			NEURL2
ARSA		TMEM98		RASSF2				IPCEF1			ZC3H12C
ARHGAP24		CAMKV		FAS				MRVI1			AC005551.1
VAMP5		CCDC177		ARHGAP24				GATA6			OSBP2
SPINK2		SLPI		SERPINB11				RSAD2			GGACT
ERO1B		GRAMD1B		AQP11				RHOC			MBLAC1
PCDHGB5		DIRAS1		OTULINL				COL5A2			AGTR2
TERB1		DPYSL3		SCEL				NT5E			CATSPER3
EGR2		PHLDA1		CLMN				EDN2			ZAN
HOXA2		NKAIN1		LAT2				NHLH2			RAB3IL1
RIIAD1		SNORA62		ACTN2				CCR2			OTOP1
TENT5C		GNB4		SPOCD1				CACNA2D3			TMEM132D
ARMCX2		COX7A1		ACSF2				PCSK2			ASPDH
ENO3		DCLK3		SPINK2				MAJIN			TRPM1
DOK5		TMEM249		PRKCQ				GUCY1B1			LTK
LOXL4		FXYD6		SIGLEC1				MYL9			C16orf54
RNF157		TRABD2B		DPYD				TYROBP			SLC24A2
FBXO27		OPTC		APCDD1				GCH1			KLHL31
		ANKRD65		MED12L				CCDC102A			B3GNT6
		IGFBP6		KIF27				B3GALT2			C3orf62
		LTBP1		ALDH3A1				PCP2			RN7SKP231
		CAPN6		CA7				PM20D1			GPR21
		SHROOM4		CHST2				CNTN2			ENDOU
		AFM		PCDH19				RAMP1			SPI1

		DLEC1		NR1I3				TSNAXIP1			LYPD5
		SLC41A3		MGP				FOXC1			HS3ST1
		ATP1A2		MYH13				TM6SF2			RASSF4
		CHI3L1		AJAP1				CYP1B1			TEKT5
		GRID2IP		PDZD7				CLEC5A			APC2
		SNX32		GLI1				SRGAP3			HLX
		ABCG4		GPRIN3				UPK1A			C20orf173
		ENPP1		GRK4				TMEM204			PTPN22
		SASH3		NEK11				SNORA2C			FABP7
		FSCN2		VAV1				KCNN2			FAM217B
		FBP2		VCAN				CALHM5			PDE1B
		CPED1		CYBA				ITGB7			SMTNL2
		SSPO		SLC16A2				SLC39A5			XKR8
		PI15		LMO1				MSANTD1			MIR339
		ICA1L		BMP6				RGS16			PKP2
		LRRC10B		UNC5D				HSD17B1			ENPP3
		GRIK3		PHKG1				PGLYRP4			FRMD7
		DNAH1		MDGA2				PPP1R1C			WFDC3
		SLC9A5		HOXD1				APBA2			BBS10
		KLHL4		PDZD4				ZEB1			NR2F2
		KCTD14		DHRS9				KIF26A			ST6GALNAC3
		RASGRP1		PSD				MYOM1			GRIK3
		AEBP1		TIGD3				NEFH			CSF1R
		NDN		RARB				SLC38A3			PPFIA4
		ARHGEF17		EPS8				CA6			KCNJ14
		ENPP2		EPPK1				RLBP1			SCAMP4
		LOXHD1		JMJD7				CPSF4L			TDRD6
		CLEC14A		LPCAT4				EVX2			SH3RF3
		ZSCAN2		PKIA				SLC7A3			C12orf60
		VSIG8		LNP1				LRG1			MN1
		FLVCR2		IL19				ZEB2			ACTL10
		SNORD71		SLC25A23				CACNB2			CST6
		GP1BA		AGR2				AMOT			LKAAEAR1
		HEG1		FBP2				HYKK			GPD1
		SDSL		ACTA2				CFAP157			LIX1
		SEMA6C		CORO1A				C11orf16			TSTD1
		FBXO2		CCL20				DKKL1			LRRC39
		NLRC5		ITIH5				CUBN			SERPINB12
		CLDN4		CFAP299				DNAH9			PATE2
		ZNF648		GALNT16				ANO4			DOCK3

		ELK3		SPRED3				LRRD1			ERICH3
		SNORD59A		RBPMS				RINL			APOH
		PLVAP		MLANA				APBB1			COL5A3
		DNER		HRC				TMEM95			FBXO24
		PKD1L1		CTNND2				ALDH1A3			CNTD1
		NRXN2		TERT				GCK			CD247
		ADGRL2		FMN1				LEPR			CHIC1
		ASXL3		IGSF9				TTC12			CCK
		FAM13A		C4orf47				GPRC5B			PCDH17
		IL7		YPEL4				RGL1			NRK
		CPA4		PLAUR				ADRA1A			FNDC11
		FZD3		FCHO1				LAT			DOK6
		KCNQ4		KLHL3				ANKRD65			SOX11
		PCDH1		DGAT2L6				GALNT14			DMBT1
		CHIC1		ENC1				NRCAM			CLCN1
		TEX26		EGR3				SLC5A8			RASL12
		CAVIN2		LPO				SETBP1			KIAA1549L
		DACH1		IGF1				TRPC6			ZP1
		ACTA2		FGFR1				CTRL			LHX3
		OPRL1		BIK				UBE2QL1			TMEM232
		PPARG		CATSPERD				LRRC39			POU6F2
		TMEM59L		EPHB2				FHL3			TMEM121B
		PPM1N		CAVIN2				FGF1			SSTR2
		TMIGD1		TMEM200B				RGS20			IL1RAPL2
		NREP		TGM5				ZBTB32			KCNS2
		OSBP2		ETNK2				RNU4-2			RGS22
		CCDC173		C20orf194				MMP8			NT5C1A
		SLC9A3R2		TAS1R3				AVIL			CIB3
		RN7SKP70		SERPING1				FOXP2			TBATA
		MINAR2		CLDN1				OASL			COL26A1
		FAM149A		PDE1B				PRKAR1B			SNORD127
		SFTPC		ICAM1				PLXNC1			PRSS57
		ESYT3		LINGO1				SLC35D3			MAEL
		TSTD1		STAC2				OGDHL			CHST4
		XIRP1		AIPL1				HIST2H3D			TUB
		REEP2		SYT12				LAMA4			SGCZ
		SCARA3		HYAL3				LGI4			IMPG1
		TNFSF13B		NLRC3				NOBOX			CACNA2D4
		IQGAP2		SYNE3				GRASP			NOS2
		RASD2		C1QTNF12				CDK3			P4HA3
		B4GALT4		TBC1D9				GLIS1			RNU6-365P
		ADH7		ARG1				NALCN			PCDHAC1

		CST6		HELZ2				SPATA7			CLVS1
		TGFB3		PCSK5				SCN5A			PCP2
		C7orf31		CHKB				GDAP1			SLC4A10
		CD83		INPP4B				RSPH1			CDHR4
		ANAPC15		ARID5A				NPAS1			RNU6-1204P
		CDO1		UCP2				SDS			SRARP
		ICA1		DCLK3				COX6B2			ACOD1
		SYNPO2		CSF1				CD5			F9
		DBNDD1		SPTB				PROX2			CFAP97D1
		KIRREL1		SLC9B2				CHRM3			HMX2
		NACAD		LEXM				TBX15			MYH6
		DOCK4		FBN1				CPS1			TRIM34
		EGR3		KHDRBS3				ABCC6			WT1
		SPATA20		ADGRV1				RF02271			CRHBP
		KLHL31		RAB17				SORBS2			KEL
		UPB1		INSL6				ADD2			MRO
		ZNF385C		SLC39A4				TXLNB			CCDC36
		SLA		DNAJC28				FMO1			NR1I2
		CFAP54		RBPMS2				ADM			DRD2
		APOM		KLK5				CNFN			CXCR1
		GPR37		RFX3				HAS1			IPCEF1
		SCEL		RPS12				SSTR4			TRIML1
		IL4		NUAK1				RNF32			HIST1H4D
		REM2		PDK4				FOXA3			OR52J3
		EMB		RSPH9				DNAI2			LEXM
		SPON2		ARHGAP4				ABHD16B			HEATR9
		IL17RD		TNFAIP3				PTGER1			KCNMB1
		GSTM2		ARHGEF25				ADGRA2			MYOCD
		HES3		UTS2				AVPR1A			DRD1
		SPATA3		MYH7				NEURL3			MSR1
		EFNB2		AGMAT				MYH11			IL6
		PPP2R2C		EMB				CORO1A			CDK15
		LRP3		IL17RD				CACNA2D2			SPAG17
		FBN1		ELAVL2				FES			CAVIN4
		LPCAT4		SACS				SLA2			ABCG2
				CALCRL				HAS2			UNCX
				LIFR				GAL3ST3			PRSS37
				RNU12				WNT2B			FGF20
				PTPN18				DNAJB7			TBX20
				SGK1				MIR99A			GLB1L3
				COX6B2				STAB1			SLC9C1
				RBP1				MORN3			PMCH
				FMNL1				DUOX2			VNN1
				FBLN1				SLIT1			TLR8
				ENPP1				RUSC2			SLCO4C1

				NOX1				FAM222A			TRARG1
				TRIB1				TC2N			ENPP7
				ITPKB				TRPV5			DOC2A
				ZNF449				CHD5			CLEC12A
				SSC5D				HIST1H1D			OSM
				AKAP6				FBXW10			OR6A2
				LMX1B				C10orf95			OR4X1
				CSRNP3				ENTPD3			MUC21
				SELENOM				GSAP			AC187653.1
				ATP6V1C2				ZNF334			LHX8
				SRCIN1				MYPN			GALNTL6
				SMIM1				RAB17			WDR49
				AP002956.1				SHROOM3			GSTA5
				GAMT				FCHO1			HSD17B14
				OPN5				INPP5J			PCDHB3
				ADGRA3				BBS10			TRMT13
				AC008403.1				MYH10			JAKMIP2
				CHI3L1				PPP1R3B			TMEM240
				SLC41A3				HOXD9			GJB2
				HSD17B8				LRRC75B			EPSTI1
				EFNB3				TDRKH			FBP1
				MCF2L				C1QC			SHISA8
				CCDC36				PCDHGA5			SEC31B
				SYT4				MMP17			RSAD2
				FTCD				LGR5			FERMT2
				CACNA1C				MIR103A2			SMIM38
				ITGA8				TRIM67			SPATA46
				SFXN4				SRARP			GCA
				ADAMTSL4				GDAP1L1			DEGS2
				GDAP1L1				DLG4			FMOD
				NECAB3				RBP1			SNX22
				IGSF10				SPRY4			FBLIM1
				ISM2				HOXC9			TSSK4
				SEMA6D				GNGT2			ARHGEF33
				PCDHGA7				CCDC154			HIST1H2AE
				FBLN2				LRRC3			
				PPP1R1C				LRP1B			
				SDK2				APBB1IP			
				FGF2				PLAG1			
				RBM46				NME5			
				TOGARAM2				PRR16			

				CYP27B1				NRAP			
				CCDC88B				BARHL1			
				WFDC3				TIMP2			
				GAB3				B4GALT5			
				ATP8A2				TGM5			
				NAT14				TMEM229B			
				FNDC7				RIMBP2			
				DLC1				RSPO1			
				WIF1				SPDYA			
				SORCS2				OTP			
				LCN2				OR52J3			
				OXTR				AKAP12			
				ANGPT1				RGS14			
				AARSD1				SOAT1			
				BEND5				ADORA1			
				CD3G				TTLL1			
				KCNAB2				CACNA1A			
				RAB2B				DNASE1L3			
				SCARA3				KCNT2			
				GJB4				NLRC4			
				LPXN				BGN			
				LGALS3BP				CHCHD10			
				TVP23A				LGALS2			
				RGMA				DCN			
				NID1				SCIMP			
				CHD5				SGIP1			
				BCL6B				CCDC24			
				KANK3				EML1			
				KLK8				SP5			
				ALCAM				PTGES3L			
				RASL10A				TMEM198			
				SFMBT2				SH2D5			
				SHE				SLC11A1			
				PLCL1				MYL6B			
				JPH1				ZNF382			
				HIST2H3D				SLIT2			
				DUSP6				SH2B2			
				DUSP1				ANKLE1			
				NHS				TM4SF1			
				IRF8				AARSD1			
				ZFP92				ABI3BP			
				KCNU1				PIP5K1B			
				BARX2				BEGAIN			
				CADM4				ACOX2			
				EFCAB12				PPFIA4			
				CALHM6				IFITM5			
				MAGI2				DNM3			
				CYP7B1				AGAP2			

				RAMP3				PKNOX2			
				ACSBG1				ATP2A3			
				CREB5				BICC1			
				SOGA1				FAM229A			
				SOX5				STYXL1			
				ANKRD61				NFASC			
				CPLANE2				ARID3C			
				ADAMTS15				C3			
				IRX2				CCDC173			
				GPR63				NKD2			
				RELN				PHLDA1			
				INPP5D				PIWIL2			
				RHBDL3				KCNC3			
				EDN1				GPR162			
				IRX3				SHC3			
				ZNF879				RASAL1			
				HPN				SLC26A10			
				PRSS53				SLC12A8			
				SLC2A4				CLDN8			
				CYP2R1				GFRA4			
				MMRN1				AP000812.5			
				LEF1				COL6A6			
				ACSM3				SCN2A			
				GMDS				KIF17			
				THBS1				VILL			
				BDNF				C1orf162			
				SEMA6C				UPB1			
				TMEM86A				DACH2			
				HDDC3				TREX2			
				SOCS3				C19orf71			
				PRSS22				TOX3			
				MZF1				INSYN2			
				DPYSL2				ABI3			
				ZNF8				CCDC150			
				DKK3				GPR137C			
				RPS6KA6				WNT8A			
				FLNB				WNT11			
				ZFP2				TRAT1			
				DOK3				HIC1			
				PTPRM				CXCR4			
				CDKL1				SNCAIP			
				MMRN2				RAC2			
				GCHFR				HPN			
				SPEG				SKAP1			
				GDF7				PLPPR2			
				RTN4RL1				DNAH1			
				APLN				TTC25			
				TXNDC8				FRAS1			
				COL5A3				DPYSL3			

				SPATA33				AMBP			
				TBX1				DMRTA2			
				AWAT2				PLP1			
				RDH5				CSMD2			
				TNFRSF13C				EGFL7			
				CAMK2B				SLC4A3			
				ZNF239				GNG3			
				RASD2				PDE7B			
				LPCAT1				IZUMO1			
				TNIK				WDR66			
				ENDOD1				SOX9			
				GLRB				KIF5A			
				ING4				CACNA1C			
				SPATA45				FBXL22			
				OAS3				WDR38			
				CCL5				C4orf47			
				FAM131A				FLVCR2			
				WSCD2				SELENOV			
				EDAR				LGI2			
				C8G				HPCA			
				CHRNB1				MLXIPL			
				PRDM8				CD200			
				NLGN3				MSH5			
				DZIP3				CALCB			
				TNFAIP8L3				ADCY5			
				WDR25				SNX32			
				ANO9				RCN3			
				KCNG3				CXCL12			
				EHF				CARD9			
				ADGRF5				NSMF			
				ADGRG2				RF01159			
				CYS1				KRT7			
				TEX26				PXMP2			
				GAS7				RASGRF1			
				GPR27				10-Mar			
				SNX22				PRRX2			
								MXRA8			
								C2CD4C			
								BACH2			
								LCP1			
								CLBA1			
								SLC27A6			
								FBXO47			
								GALR2			
								STARD8			
								ENOX1			
								SAMD14			
								KLHL41			
								SGMS2			

								IMPG1			
								HPGD			
								HIP1			
								PGM5			
								PLA2G4B			
								SOGA1			
								GLI1			
								SSC4D			
								TLR2			
								TMEM269			
								ESR2			
								VWF			
								PPP1R3C			
								SLC6A17			
								PLEKHO1			
								ITPR1			
								ACYP2			
								AIFM3			
								TNC			
								SHISA2			
								FHL2			
								SYT2			
								TMEM88B			
								ARMH4			
								SULT4A1			
								CERS4			
								CRYM			
								FLG2			
								COL6A2			
								CCDC103			
								SNX22			
								MANSC4			
								PIK3R6			
								RSKR			
								PDLIM4			
								INHBB			
								COL5A3			
								APLP1			
								CTSW			
								ZFP69			
								CTNNA2			
								MORN1			
								CFD			
								CLDN20			
								IL10RA			
								CHRM1			
								EMP3			
								IQGAP2			
								AREG			

Table S3: Hallmark pathways from all our RNA-seq studies

Tail_sc-RNAseq_pathways

NAME	Diff	SC1	SC2	SC3	G1S	G2M
E2F_TARGETS (131)	-4.682936	-3.6657124	-4.268467	-3.1023793	-1.3501003	-1.1582348
G2M_CHECKPOINT(109)	-4.0574727	-3.5039718	-3.9589846	-3.154362	-1.5346452	1.4125943
MITOTIC_SPINDLE(55)	-3.7995632	-3.45657	-3.3746545	-3.5983226	-1.9686298	1.148271
SPERMATOGENESIS (20)	-2.7097	-2.587747	-2.7308521	-2.6092844	-2.0825965	-2.01912
DNA_REPAIR(35)	-1.7658774	-1.2542319	-1.3261507	-1.0925092	1.5067235	-1.2052015
ESTROGEN_RESPONSE_LATE(39)	-1.0820348	-1.0364676	-1.1823704	-1.311109	-1.3219357	-1.206096
UV_RESPONSE_DN(17)	-0.8684176	-0.8568197	-0.4748836	-0.8989706	-1.5496964	-1.1688973
GLYCOLYSIS(35)	-0.7186033	0.5066259	1.1794835	-0.8322288	0.9271684	0.9493796
MYC_TARGETS_V2(17)	-0.6163698	0.47856164	-0.6939467	0.7717562	1.862138	-0.6633685
OXIDATIVE_PHOSPHORYLATION(34)	3.8014102	3.8727715	3.9656787	3.8933487	3.4391928	3.7819068
MYC_TARGETS_V1(101)	3.2650836	2.9192746	2.8684375	3.50464	4.7686462	3.7057416
UNFOLDED_PROTEIN_RESPONSE(22)	2.0615308	2.0750618	1.7570882	2.1654615	2.4180565	2.0971475
PI3K_AKT_MTOR_SIGNALING(18)	2.0148757	1.7436715	1.8168856	1.9228346	1.5121639	1.8904669
INTERFERON_GAMMA_RESPONSE(15)	1.7909826	1.4254903	1.6139947	1.7082126	1.0122232	1.0722735

COMPLEMENT(19)	1.7091873	1.564375	1.4140358	1.6596674	1.0857165	1.5047451
P53_PATHWAY(37)	1.7050356	2.3698084	1.8601553	1.9064758	1.5264822	1.0347332
APICAL_JUNCTION(24)	1.6896509	2.106274	2.0134456	1.8080944	1.4377779	1.3275843
APOPTOSIS(36)	1.6242682	1.845518	1.410226	1.2935796	1.3854384	1.0857083
HEME_METABOLISM(19)	1.5273745	1.5359646	1.47111	0.9921816	0.9104973	1.1543444
HYPOXIA(41)	1.4429158	1.0555362	1.8087212	1.3543615	-0.5798251	-0.5913035
FATTY_ACID_METABOLISM(26)	1.3684269	1.4507499	1.0484419	1.3456621	1.195047	1.5306946
ADIPOGENESIS(31)	1.3648088	1.4306811	1.3495574	1.1902834	1.0909387	1.1220694
MTORC1_SIGNALING(61)	1.3341583	1.3332473	1.3095369	1.6075851	1.5658602	1.2920396
MYOGENESIS(25)	1.2682966	1.189895	1.2733841	1.0881729	-1.5470449	-1.1128021
IL2_STAT5_SIGNALING(25)	1.2464702	1.5840027	1.5088308	1.5381008	1.010398	0.76815104
TNFA_SIGNALING_VIA_NFKB(32)	1.1795988	0.81324124	0.8638118	-1.0219656	-1.3939989	-1.5722883
PEROXISOME(16)	1.1494766	-1.0203288	-0.9958598	-1.0092525	-0.6897997	-0.8614714
COAGULATION(21)	1.1192429	0.8508343	0.70759463	0.8164171	-0.7656635	-0.6505861
CHOLESTEROL_HOMEOSTASIS(19)	1.0921057	-1.130683	-1.0657239	-1.3410021	-1.0363894	1.30462
UV_RESPONSE_UP(25)	1.0530409	0.98483425	1.1967087	1.4645655	1.3650792	0.8406757
ESTROGEN_RESPONSE_EARLY(24)	1.0086446	-0.8372409	0.78612363	-0.540132	-1.2021458	-1.2737598

ANDROGEN_RESPONSE(17)	0.982604	0.7368959	0.8731565	0.94490206	-0.708591	0.84426224
KRAS_SIGNALING_UP(16)	0.87573624	0.8926478	0.6622392	-0.5920608	-1.2808753	-1.2886429
XENOBIOTIC_METABOLISM(18)	0.8652188	0.8839879	-0.8824338	-1.1358254	-0.6629924	-1.1481693
EPITHELIAL_MESENCHYMAL_TRANSITION(35)	0.8568717	0.9170984	1.5241637	1.1169033	-1.1393188	-0.9202461

BACK_Lineages_BulkRNAseq_pathways

NAME	K14_NES	Aspm_NES	Slc1a3_NES
ADIPOGENESIS(23)	-1.7230686	-1.6615951	-0.7113095
APICAL_JUNCTION(55)	-1.3602146	-0.636548	-1.1650925
XENOBIOTIC_METABOLISM(40)	-1.273821	-0.5180924	1.0235921
KRAS_SIGNALING_DN(79)	-1.2222909	1.0439161	-0.837944
KRAS_SIGNALING_UP(73)	-1.1887958	-0.705478	0.9697699
HYPOXIA(38)	-1.1769724	-2.436133	-1.0642399
EPITHELIAL_MESENCHYMAL_TRANSITION(82)	-1.1077985	-2.444594	-1.0821555
UV_RESPONSE_UP(28)	-0.978177	0.9317005	1.0360665
INTERFERON_GAMMA_RESPONSE(42)	-0.8350972	-1.5736722	-0.7196346
IL6_JAK_STAT3_SIGNALING(20)	-0.7998071	-0.8605501	1.0866358
TNFA_SIGNALING_VIA_NFKB(37)	-0.7233527	-1.689807	0.7619891
FATTY_ACID_METABOLISM(20)	-0.7127058	-0.6498675	-0.8703838
SPERMATOGENESIS(44)	1.7043755	-1.2103025	-0.9694198
UV_RESPONSE_DN(25)	1.5465708	-1.4077727	0.6895311
ESTROGEN_RESPONSE_EARLY(39)	1.3811834	-1.5613638	-0.9670543
GLYCOLYSIS(27)	1.3259623	-1.6409675	1.1435146
HEME_METABOLISM(27)	1.325411	-0.8607146	1.2895303
ESTROGEN_RESPONSE_LATE(34)	1.2173046	-0.9858574	-1.3250542
COAGULATION(43)	1.1804487	2.1603937	0.9711534
P53_PATHWAY(18)	1.0687017	-1.6918521	-0.9272006
COMPLEMENT(56)	1.0328388	1.3844367	-1.1598985
ALLOGRAFT_REJECTION(76)	0.90808254	-1.060405	1.6945944
APOPTOSIS(29)	0.85158426	-1.1295991	1.2176819
IL2_STAT5_SIGNALING(50)	0.84490097	-1.1987575	2.1733627
ANGIOGENESIS(16)	0.77023053	1.131217	1.1706219

PANCREAS_BETA_CELLS(15)	0.7282419	-1.1135167	1.7134359
INFLAMMATORY_RESPONSE(81)	0.6873166	-0.8574358	-0.5551702
MYOGENESIS(70)	0.5473834	-2.2354105	-1.1164178
BILE_ACID_METABOLISM(26)	0.4445975	0.9281388	-0.9497377

TAIL_Lineages_BulkRNAseq_pathways

NAME	Dlx1_NES	Aspm_NES	Slc1a3_NES
EPITHELIAL_MESENCHYMAL_TRANSITION(81)	-2.6186883	-2.3714032	-3.4202883
UV_RESPONSE_DN(34)	-1.9197372	-1.9594172	-1.7762134
P53_PATHWAY(16)	-1.7161264	-1.1403478	-1.575166
APICAL_JUNCTION(62)	-1.6988373	-0.9111538	-1.3946847
ESTROGEN_RESPONSE_EARLY(47)	-1.6603141	-1.7536302	-1.9194853
XENOBIOTIC_METABOLISM(40)	-1.4936395	1.4369602	-0.9087182
BILE_ACID_METABOLISM(28)	-1.2516438	0.6665449	1.0057685
UV_RESPONSE_UP(26)	-1.2073126	0.58741003	-0.7453425
IL6_JAK_STAT3_SIGNALING(21)	-1.1945552	-1.3556325	-1.5200282
ADIPOGENESIS(23)	-1.1065606	0.95920795	-0.8430871
IL2_STAT5_SIGNALING(50)	-0.9799851	0.8211293	-1.5377597
HEME_METABOLISM(27)	-0.8823531	0.9291757	-0.6240804
ESTROGEN_RESPONSE_LATE(39)	-0.8815707	0.91418177	-0.8276745
INTERFERON_GAMMA_RESPONSE(54)	-0.8676996	-0.992394	-1.7959685
INFLAMMATORY_RESPONSE(78)	-0.859344	0.98626304	-2.2286022
GLYCOLYSIS(35)	-0.8585612	-1.668841	0.57231283
SPERMATOGENESIS(41)	-0.81315	0.9893882	-0.9112202
MYOGENESIS(68)	-0.7283331	-2.076922	0.97508645
HYPOXIA(43)	-0.6789476	-1.621721	0.7484723
INTERFERON_ALPHA_RESPONSE(19)	-0.6589274	-0.9863508	-1.6548676
ALLOGRAFT_REJECTION(70)	2.289419	0.82894033	-1.8440007
PANCREAS_BETA_CELLS(18)	1.645536	0.7656557	1.3558906
KRAS_SIGNALING_UP(77)	1.2137183	1.1777133	-1.0576171
COAGULATION(40)	1.1363317	-0.8872311	0.7577182
APOPTOSIS(34)	1.0492808	0.5125637	-1.4000115
COMPLEMENT(51)	0.8890659	1.1915193	-0.8677361
KRAS_SIGNALING_DN(77)	0.8760653	-0.8056086	0.87724537
FATTY_ACID_METABOLISM(19)	0.8416021	0.80583864	0.89124566
TNFA_SIGNALING_VIA_NFKB(47)	0.8196529	-0.9630933	-2.8415568